THREE-DIMENSIONAL MODELING OF ELASTO-PLASTIC SINUSOIDAL CONTACT UNDER TIME DEPENDENT DEFORMATION INCLUDING BOTH STRESS RELAXATION AND CREEP ANALYSIS

by

Amir Rostami

A Thesis Submitted to the Graduate Faculty of
Auburn University
in Partial Fulfillment of the
requirements for the Degree of
Master of Science

Auburn, Alabama
August 3, 2013

Keywords: 3D Sinusoidal Contact, Elasto-plastic, Stress Relaxation, Creep, Finite Element Model

Approved by

Robert L. Jackson, Chair, Associate Professor of Mechanical Engineering
Hareesh V. Tippur, McWane Professor of Mechanical Engineering
Jeffery C. Suhling, Quina Distinguished Professor and Department Chair

ABSTRACT

Computational modeling of contact between rough surfaces has attracted a great deal of attention due to the developing technological needs of industry. Most of the early models of rough surface contacts assumed a cylindrical or spherical/ellipsoidal shape for the asperities on the surfaces. Due to high memory space and computational time requirements, researchers use simplified geometries to model the asperities or peaks on rough surfaces. Recent works tried to use a sinusoidal shape for asperities to improve the previous models. The sinusoidal geometry gives a better prediction of asperity interaction, especially for heavily loaded contacts. The effect of adjacent asperities is considered in sinusoidal contacts by using a symmetric boundary condition. Also, most of the multiscale contact models for rough surfaces use the Fourier series or Weierstrass profile to transform a rough surface to combination of sine and cosine functions. Therefore, it seems more reasonable to use a sinusoidal shape for asperities.

In the current work, the transient effect of creep and stress relaxation in contact between sinusoidal surfaces is studied using FE simulations. A three-dimensional sinusoidal asperity is created, and is modeled in contact with a rigid flat surface. The material of the sinusoidal surface is modeled as elasto-plastic, bi-linear isotropic hardening solid. The Garofalo formula is used in the current work to model the transient behavior of creep and stress relaxation. Two load steps are used in commercial software ANSYS (version 13.0) to model the effect of creep and stress relaxation. The first load step is static deformation or the stress build-up stage that is used to pressurize the asperity by the rigid flat surface. The second load step is the transient process during which creep and stress relaxation occur. To verify the model, the results for the purely elastic and elasto-plastic cases (without the creep and stress relaxation effects) are compared to the previous works in the literature.

Transient results under both constant displacement (stress relaxation) and constant force (creep) boundary conditions are presented and discussed. A parametric study is done to analyze the effect of the different material and geometrical properties and also the Garofalo constants on the

transient results. In the end, empirical equations are developed for both contact area and contact pressure based on the FEM results. The empirical equations are dependent on the surface separation, aspect ratio, and the Garofalo formula constants. In the contact area and contact pressure results for stress relaxation, a critical interference or surface separation was found that the contact area and contact pressure showed different behaviors above and below this value. The aspect ratio rate, $\delta\Delta/(\lambda\delta\tau)$, is introduced as a parameter that is independent from the height of the asperity during the stress relaxation process. This rate can be used in a multiscale contact model for rough surfaces to predict the real contact area as a function of time.

ACKNOWLEDGEMENTS

This thesis is based on the project that has been assigned and supported by the Siemens Corporate Technology under the title of "*The Development and Application of Multi-scale Friction Prediction Methods to Dynamic Actuator Systems*". I started working on this project from January 2012 along my M.Sc. studies in Auburn University under the supervision of **Prof. Robert L. Jackson**. I should thank Prof. Jackson who helped me a lot during this year and half, and I've benefited from his suggestions and ideas countlessly during the course of the project. He has been completely involved in every step of the project, and always supported me during the difficulties of the work. I should thank Mr. Andreas Goedecke and Mr. Randolf Mock in Siemens Corporate Technology. They have always supported and helped us with the data and info we needed during the project. I should also thank Prof. Hareesh V. Tippur and Prof. Jeffrey C. Suhling for serving on my thesis committee. In the same way, I should thank my lab mates in the Multi-scale Tribology Laboratory at Auburn University for their friendship and support and many shared laughs and hard work during this year and half.

I should also mention the support of the most important people in my life, my parents, during my Master studies which of course they are far away from me, but, they have always been close to me in my heart. I will try my best to be a person that will make them proud.

TABLE OF CONTENTS

LIST OF FIGURES

LIST OF TABLES

NOMENCLATURE

A	area of contact
B	aspect ratio
B'	creep constant of the power law
B''	creep constant of the exponential law
β	creep constant of the exponential law
C	critical yield stress coefficient
$C_i, \tilde{C}_i \ (i = 1-4)$	creep constants of the Garofalo, strain hardening, and modified time hardening model
d	material and geometry dependent exponent
E	elastic modulus
E'	reduced or effective elastic modulus
f	spatial frequency (reciprocal of wavelength)
F	contact force
g	average surface separation
G	normalized surface separation
h	height of the sinusoidal surface
n	creep constant of the Garofalo law
H	hardness
p^*	average pressure for complete contact (elastic)

p_{ep}^{*}	average pressure for complete contact (elasto-plastic)
$\overline{p}$ *or* p_{ave}	average pressure over entire asperity
P	normalized contact pressure
S_y	yield strength
t	contact time
τ	dimensionless contact time
Δ	amplitude of the sinusoidal surface
λ	asperity wavelength
ν	Poisson's Ratio
σ	stress
ε	strain
δ	interference between sinusoidal asperity and rigid surface
a, b	curve-fitting parameters for contact area
a', b', c', d'	curve-fitting parameters for contact pressure

Subscripts

0	initial or at $t = 0$
c	critical value at onset of plastic deformation
cr	creep dependent parameter
e	elastic
ep	elasto-plastic
JGH	from model by Johnson et al. [2]

CHAPTER 1

INTRODUCTION

The topic of contact between surfaces has been popular to researchers for many years. There exists many works on modeling the contact of surfaces starting around 1888 by Hertz [3] (originally developed to model optical contacts). All engineering surfaces are rough to some degree, therefore it is important to develop a model for the contact between rough surfaces. The main goal in modeling the contact between rough surfaces is to find a simple closed form solution for the real contact area. Most tribological effects such as friction, wear, adhesion, and electrical and thermal contact resistance are dependent on the real contact area between two contacting surfaces.

Creep and stress relaxation are time dependent phenomenon which cause changes in the stress and strain in a material over time. For contacting surfaces, creep and stress relaxation cause changes in the contact area and contact pressure between surfaces as time passes. Stress relaxation refers to the stress relief of a material under constant strain condition (Fig. 1.1a), and creep describes how strain in a material changes under constant stress condition (Fig. 1.1b). Any material can experience creep if certain conditions are met. It could be metals at high temperatures, polymers at room temperatures, and any material under the effect of nuclear radiation. Although there is no recovered creep strain or reversible behavior under normal operating conditions, elastic deformations are still recovered. The goal of this thesis is to model the effect of creep and stress relaxation in contact between sinusoidal surfaces.

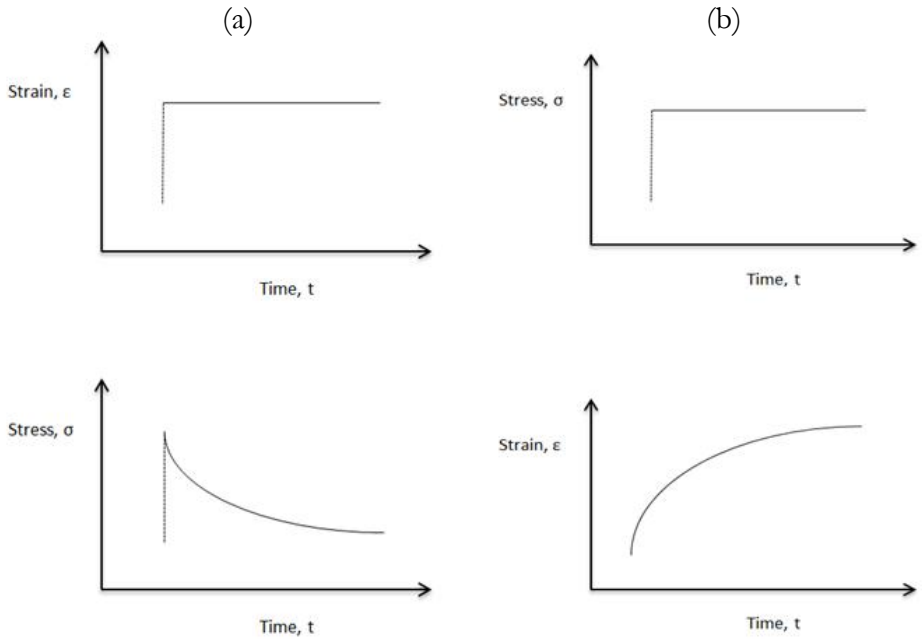

Fig. 1.1 Change in the stress and strain in a material due to (a) stress relaxation, and (b) creep

The change in contact area due to creep is considered as the reason why static friction changes over time, and why the dynamic friction is dependent on velocity [4-6]. The previous works on the creep effect in contact between surfaces used a cylindrical [4, 7-10] or spherical [1, 11, 12] geometry for the asperities. In this work, a sinusoidal geometry is developed and analyzed which is believed to be a more realistic geometry. The interaction between adjacent asperities, which is ignored in most previous works, is considered by assuming a sinusoidal asperity. Two kinds of boundary conditions are used in the current work to model the time dependent deformations: (i) constant displacement boundary condition (stress relaxation) and (ii) constant force boundary condition (creep). The hyperbolic sine function also known as the Garofalo formula is used to model the effect of the creep and stress relaxation [1]. The results for the contact area and contact pressure as they change over time are presented and discussed. Empirical equations are developed by fitting to the FEM results. These empirical equations can be put in a multiscale model to obtain the real contact area for a specific surface in contact as a function of time. This real contact area can

be used to obtain a prediction for the time dependent static friction or the velocity dependent dynamic friction between surfaces.

CHAPTER 2

LITERATURE REVIEW

2.1 Introduction

Most of the previous models on the contact between rough surfaces assume a spherical shape [13-20] or ellipsoidal shape [21-23] for the geometry of the asperities on the surfaces. Archard [14] used a stacked model of spherical asperities and showed that although the relation between the contact area and load for a single asperity is nonlinear, by using a multi-scale model this relation becomes linear.

More recent models consider a sinusoidal shape for the asperities because it seems to model the geometry of real surfaces better, especially for heavily loaded contacts [24-28]. It is shown for two-dimensional sinusoidal surfaces [26] and three-dimensional sinusoidal surfaces [27] that the average contact pressure increases past the conventional hardness, H, limit of $3 \cdot S_y$ obtained by assuming spherical geometries [29]. Several works have shown experimentally measured contact pressures much higher than three times the yield strength ($3 \cdot S_y$) [30, 31]. Furthermore, the interaction between adjacent asperities is addressed by using a sinusoidal geometry with accurate boundary conditions which is overlooked in works based on spherical asperities. Also, most of the models consider the multi-scale nature of surface roughness by using a Fourier series or Weierstrass profile [25, 32-34], and since these series use superimposed harmonic waves, it is logical to use a sinusoidal shape instead of a spherical shape in modeling the asperities.

The first models on the contact between rough surfaces using sinusoidal shaped asperities were mostly on the purely elastic contact. The elastic contact of two-dimensional sinusoidal surfaces was first solved by Westergaard [24]. Johnson et al. (JGH) [2] presented two asymptotic solutions

for the elastic contact of three-dimensional sinusoidal surfaces, but no analytical solution is available for the entire load range. Jackson and Streator [34] developed an empirical equation based on the JGH data [2] for the whole range of loading from early contact to complete contact.

When two surfaces come into contact, it is primarily the peaks or asperities that carry the load and make the contact. Therefore, the small contact area caused by the asperities carries very high pressures, and plastic deformations are practically inevitable in most cases of contact between metallic rough surfaces. Gao et al. [26] considered plastic deformations in their sinusoidal contact model. They modeled a two-dimensional elastic-perfectly plastic sinusoidal contact using the finite element method (FEM). Krithivasan and Jackson [27] and Jackson et al. [28] considered both elastic and elasto-plastic contacts in three- dimensions in their work, and presented empirical equations for the contact area as a function of contact pressure for the whole range of contact. Their equations are used to verify the current model in the next sections.

One of the important stages in contact between surfaces is when "complete contact" happens. The definition of complete contact between rough surfaces depends on the specific case and geometry of the surfaces in contact. In contact between sinusoidal surfaces, it is defined as the state in which sinusoidal surfaces have completely flattened out and there is no gap in between the surfaces. The average pressure (including both contacting and non-contacting regions) that causes complete contact is an important parameter used to interpret the results, and is denoted by p^*.

Recent works extended the asperity contact models by including both normal and tangential loading [35], and loading and unloading [36-38]. However, the transient behavior of asperities under loading such as creep and stress relaxation has been neglected in these works. There have been a few works on the computational modeling of the creep [11, 12] and stress relaxation [1] effect in the contact between surfaces but their concentration has been mostly restricted to a single spherical asperity contact. Most of the earlier models on the effect of the creep in contact between asperities have assumed a rigid spherical punch indenting an elasto-plastic flat surface [39-43].

Different effects in contact between rough surfaces such as the dwell-time dependent rise in static friction [5, 44], the velocity dependent dynamic friction [6-9] or friction lag and hysteresis [45] can be explained by the creep theory. Many experimental studies concerning the increase of friction with dwell time are published i.e. [46-50]. Malamut et al. [44] studied the effect of dwell time on the static friction coefficient due to creep for spherical contacts.

The creep behavior depends on the temperature and stress level to which the material is exposed, and depends noticeably on the time duration of application of these conditions. The change in the real contact area between two solids due to time of stationary contact is the main motivation for modeling the creep and stress relaxation effects.

The current analysis uses the same geometry used in Johnson et al. [2] and Krithivasan and Jackson [27] in order to compare the results in this paper to their works. The sinusoidal geometry is described by:

$$h = \Delta\left(1 - \cos\left(\frac{2\pi x}{\lambda}\right)\cos\left(\frac{2\pi y}{\lambda}\right)\right) \tag{2.1}$$

where h is the height of the sinusoidal surface, Δ is the amplitude of the sinusoidal surface, and λ is the wavelength of the sinusoidal surface. The contour plot of the sinusoidal surface is shown in Fig. 2.1.

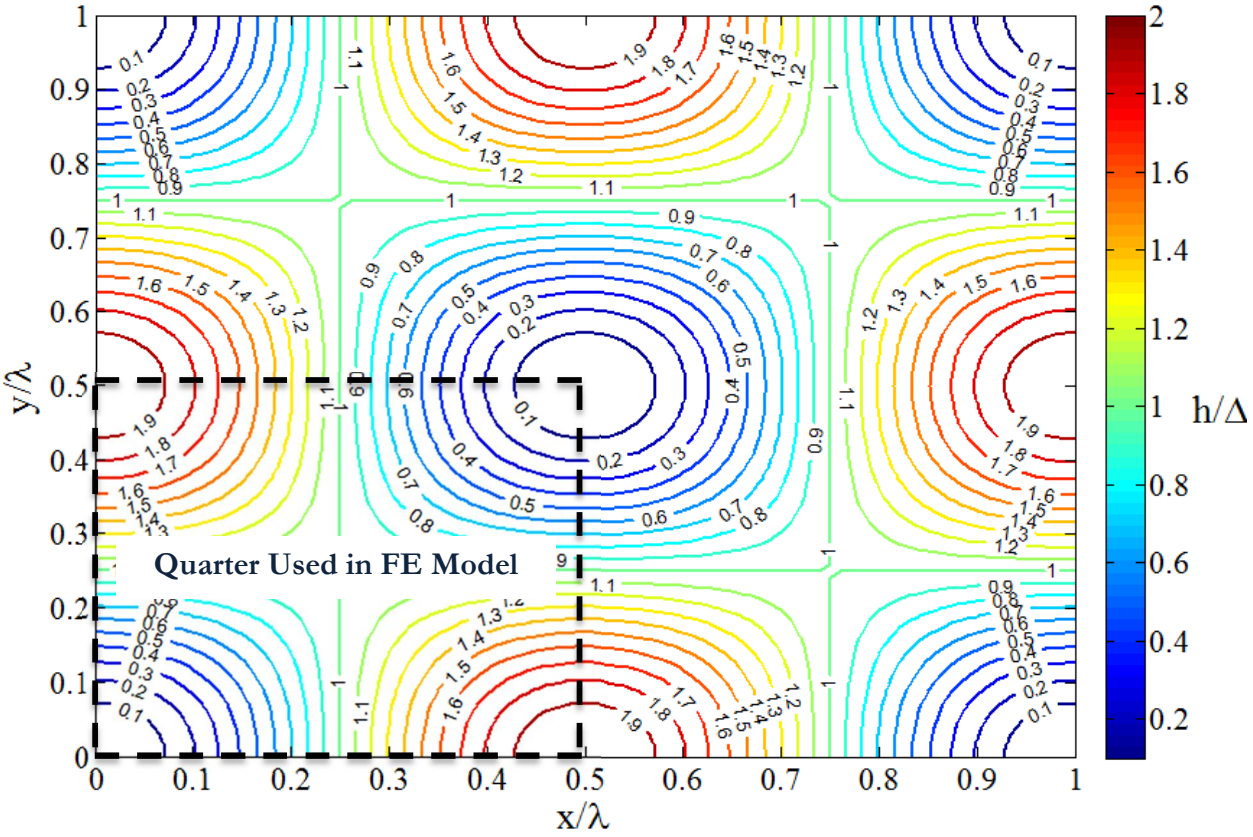

Fig. 2.1 Contour plot of the three-dimensional sinusoidal surface geometry

2.2 Elastic Sinusoidal Contact of Single Asperity

As mentioned before, Johnson et al. [2] developed asymptotic solutions for contact area of a perfectly elastic contact of three-dimensional sinusoidal shaped surfaces. In their work, $\bar{p}$ is defined as the average pressure on the surface (considering both contacting and non-contacting regions), and p^* is defined as the average pressure that when applied to the surface causes complete contact. p^* is given as:

$$p^* = \sqrt{2}\pi E' \Delta f \tag{2.2}$$

where Δ is the amplitude of the sinusoidal surface, f is the frequency or reciprocal of the asperity wavelength, λ, and E' is the equivalent elastic modulus which is given by:

$$\frac{1}{E'} = \frac{1-\nu_1^2}{E_1} + \frac{1-\nu_2^2}{E_2} \tag{2.3}$$

E_1, ν_1 and E_2, ν_2 are the elastic modulus and Poisson's ratio of the contacting surfaces.

The flat surface is considered to be rigid in this work: $(E_2 \to \infty)$, and Eq. (2.3) reduces to:

$$E' = \frac{E_1}{1-\nu^2} \tag{2.4}$$

The Johnson et al. [2] solutions are applicable when $\bar{p} << p*$ i.e. at the early stages of contact, and when $\bar{p}$ approaches p^* $\bar{p} \to p*$ i.e. near the complete contact. The equations are given as shown:

$$\bar{p} << p* : \qquad (A_{JGH})_1 = \frac{\pi}{f^2}\left[\frac{3}{8\pi}\frac{\bar{p}}{p^*}\right]^{2/3} \tag{2.5}$$

$$\bar{p} \to p^* \quad : \qquad (A_{JGH})_2 = \frac{1}{f^2}\left(1 - \frac{3}{2\pi}\left[1 - \frac{\bar{p}}{p^*}\right]\right) \tag{2.6}$$

Jackson and Streator [34] developed an empirical equation based on the experimental and numerical data provided by Johnson et al. [2], linking Eqs. (2.5) and (2.6):

$$\text{for } \frac{\bar{p}}{p^*} < 0.8 \ : \qquad A = (A_{JGH})_1\left(1 - \left[\frac{\bar{p}}{p^*}\right]^{1.51}\right) + (A_{JGH})_2\left(\frac{\bar{p}}{p^*}\right)^{1.04} \tag{2.7}$$

$$\text{for } \frac{\bar{p}}{p^*} \geq 0.8 \ : \qquad A = (A_{JGH})_2 \tag{2.8}$$

2.3 Elasto-Plastic Sinusoidal Contact of Single Asperity

Three-dimensional elasto-plastic contact between sinusoidal surfaces has been investigated by Krithivasan and Jackson [27] and Jackson et al. [28]. They showed that for the elasto-plastic contact, complete contact occurs much earlier (at the lower pressures) than elastic contact. Jackson et al. [28] presented an empirical equation for calculating the average pressure, p_{ep}^* , that causes complete contact for the elasto-plastic case. The equation is given below:

$$\frac{p_{ep}^*}{p^*} = \left(\frac{11}{4(\Delta/\Delta_c) + 7}\right)^{3/5} \tag{2.9}$$

where Δ_c is the analytically derived critical interference, and is given by:

$$\Delta_c = \frac{\sqrt{2}}{3\pi}\frac{S_y}{E'}\frac{e^{2/3\nu}}{f} \tag{2.10}$$

Jackson and Krithivasan's [27] empirical equation for the contact area versus contact pressure for the elasto-plastic case is given by:

$$A = \left(A_p\right)\left(1 - \left[\frac{\overline{p}}{p^*_{ep}}\right]^{1.51}\right) + \left(A_{JGH}\right)_2\left(\frac{\overline{p}}{p^*_{ep}}\right)^{1.04} \tag{2.11}$$

where A_p is given by

$$A_p = 2\left(\frac{A_c}{2}\right)^{\frac{1}{1+d}}\left(\frac{3.\overline{p}}{4CS_y}\lambda^2\right)^{\frac{d}{1+d}} \tag{2.12}$$

In the above equation, A_c is the critical contact area for the sinusoidal contact based on spherical contacts [19], and is given by:

$$A_c = \frac{2}{\pi}\left(\frac{CS_y}{8\Delta f^2 E'}\right)^2 \tag{2.13}$$

where the constant C is related to the Poisson's ratio by:

$$C = 1.295\exp(0.736v) \tag{2.14}$$

The value of the constant d in Eq. (2.12) is given by:

$$d = d_1\left(\frac{E'}{S_y}\frac{\Delta}{\lambda}\right)^{d_2} \tag{2.15}$$

where, $d_1 = 3.8$ and $d_2 = 0.11$ are constants which are obtained empirically by curve-fitting to FEM results.

In the current work, Eq. (2.11) is used to confirm the first load step or stress build-up stage of the finite element model (before creep and stress relaxation initiate at $t = 0$).

2.4 Average Surface Separation in Sinusoidal Contacts

In many applications that require tight tolerances such as sealing and lubricated bearings, it is important to be able to predict the surface separation between contacting surfaces. The average separation also determines the volume of the space trapped between two surfaces which is a very important parameter in lubricated surfaces. Little work has been done to characterize the surface separation or gap between sinusoidal surfaces as a function of load. In Fig. 2.2, surface separation between a sinusoidal asperity and a rigid flat surface in two-dimensions is shown. The average surface separation before the contact is equal to the amplitude of the sinusoidal asperity, $\bar{g} = \Delta$, (Fig. 2.2a), and during the contact the average surface separation is less than the amplitude, $\bar{g} < \Delta$, (Fig. 2.2.b). Johnson et al. [2] developed two asymptotic solutions for the average surface separation, $\bar{g}$, as a function of contact pressure, $\bar{p}$, for the elastic case. These solutions are for early contact $\bar{p} << p^*$ and nearly complete contact $\bar{p} \to p^*$ situations. These two asymptotic solutions are given in Eqs. (2.16) and (2.17) (note that the normalized variables $P_e = \dfrac{\bar{p}}{p^*}$ and $G = \dfrac{\bar{g}}{\Delta}$ are used in the equations).

$$P_e << 1: \qquad G_1 = 1 - \frac{1}{2}\left(3\pi^2 P_e\right)^{2/3} + \left[4ln\left(\sqrt{2}+1\right)\right]\cdot\left(P_e\right) \tag{2.16}$$

$$P_e \to 1: \qquad G_2 = \frac{16}{15\pi^2}\left(\frac{3}{2}\right)^{3/2}\left[1 - P_e\right]^{5/2} \tag{2.17}$$

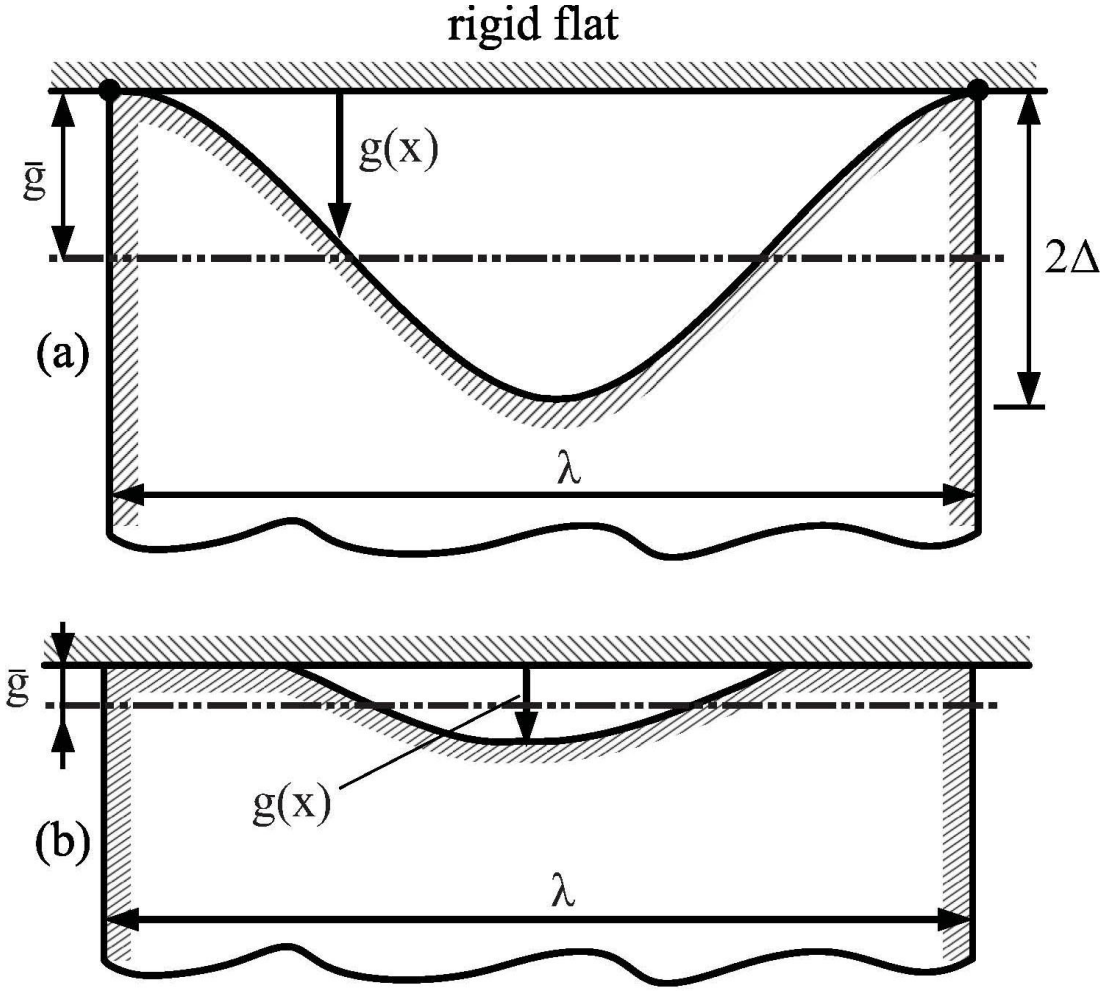

Fig. 2.2 Rigid flat and the sinusoidal asperity (a) before contact and (b) during contact where surface separation, amplitude and the wavelength of the sinusoidal asperity are shown schematically

Their asymptotic solutions are based on the elastic Hertz contact theory for early contact and the crack theory for near complete contact conditions. In this work, empirical equations are provided based on the FE simulations that can approximately predict the average surface separation for both elastic and elastic-plastic sinusoidal contacts over a wide range of material properties and over the whole range of contact.

2.5 Creep and Stress Relaxation Effects in Single Asperity Contacts

For analyzing the creep and stress relaxation behavior of materials, usually two different approaches have been used in the literature. The first one is a mathematical approach based on a combination of springs and dashpots [51] to model the transient effect and the second approach is based on the experimental results to relate different creep parameters using empirical formulas [1, 11, 12]. In this work, the second approach is considered. Some of the empirical equations that are used in creep and stress relaxation modeling are listed as follows:

Power law [52, 53] $$\dot{\varepsilon}_{cr} = B'\sigma^{n} \tag{2.18}$$

Exponential Law [52, 53] $$\dot{\varepsilon}_{cr} = B''exp(\beta\sigma) \tag{2.19}$$

Garofalo Law [53, 54] $$\dot{\varepsilon}_{cr} = C_1 sinh^{n}(C_2\sigma) \tag{2.20}$$

Strain Hardening [52, 53] $$\dot{\varepsilon}_{cr} = C_1\sigma^{C_2}\varepsilon_{cr}^{C_3}e^{-C_4/T} \tag{2.21}$$

Modified Time Hardening [52, 53] $$\varepsilon_{cr} = \frac{C_1\sigma^{C_2}t^{C_3}e^{-C_4/T}}{(C_3+1)} \tag{2.22}$$

In the above equations, ε_{cr} is the creep component of the strain, σ is the nominal stress in the material, T is the temperature, and the constants C_i $(i=1-4)$, B', B'', and β are creep parameters which are obtained by curve-fitting to the results of an accurate creep experiment. It is suggested in [54] that the power creep law is only applicable to low stresses, and for high stresses the exponential creep law gives better predictions. In addition, it is sometimes hard to distinguish experimentally between power and exponential creep laws. Therefore, the Garofalo creep law [54] was introduced which reduces to the power law for low stresses and to the exponential law for high stresses.

In modeling the transient deformation in contact between single asperities, two boundary conditions are usually used: Constant interference (i.e. relaxation) and constant force (i.e. creep).

Some works [11, 12] employed a constant normal force, and others employed constant interference [1] boundary conditions. In the rest of this section as an example of each boundary condition, a summary of the two works by Goedecke and Mock [1] and Brot et al. [11] is given.

The stress relaxation behavior of an elastic-perfectly plastic hemispherical asperity in fully plastic contact with a rigid flat surface by Goedecke and Mock [1], is discussed here. It should be mentioned that the "creep" and "stress relaxation" terms are used in this work interchangeably. Fully plastic contact means that the material has reached the yield criteria everywhere in the contact area.

We can write the following equation for the total strain tensor, ε_{tot} , which can be separated into the creep, plastic and elastic strain tensors:

$$\dot{\varepsilon}_{tot} = \dot{\varepsilon}_{cr} + \dot{\varepsilon}_{pl} + \dot{\varepsilon}_{el} \tag{2.23}$$

In the creep (stress relaxation) process, the elastic strain, $\dot{\varepsilon}_{el}$, decreases in favor of the creep strain, thus reducing the total stress to $\sigma = C : \varepsilon_{el}$ with C being the elasticity tensor[1]. It is sufficient to formulate the uniaxial creep law, $\dot{\varepsilon}_{cr}(\sigma)$, where ε_{cr} and σ denote the equivalent strain and stress (von Mises stress), respectively. Using the Garofalo creep law with this model, as presented by Goedecke and Mock [1], two distinct phases of creep (stress relaxation) can be distinguished. The asperity creeps with an accelerated creep rate in the first phase, but in the second phase the asperity creeps with a much slower rate and no significant contact area change can be seen. It should be noted that the inclusion of a time- or temperature-dependent material creep law is straightforward as long as the hyperbolic sine dependence on stress is retained. In this case, the constant C_1 becomes a time- and temperature-dependent function, $C_1(t,T)$, and can be included trivially in the equations describing the asperity behavior.

[1] In this notation, the colon (:) marks a reduction of the full tensor grade by 2; i.e., a multiplication of a tensor of the fourth grade with a tensor of the second grade yields a tensor of second grade.

As mentioned before, in this model (Goedecke and Mock [1]) the contact between a hemispherical asperity and a rigid flat is under a fixed interference boundary condition, δ, (see Fig. 2.3). It is assumed that $n=1$ in the Garofalo formula (Eq. 2.20) which corresponds to Persson's creep theory [10]:

$$\dot{\varepsilon}_{cr} = C_1 \sinh(C_2 \sigma) \tag{2.24}$$

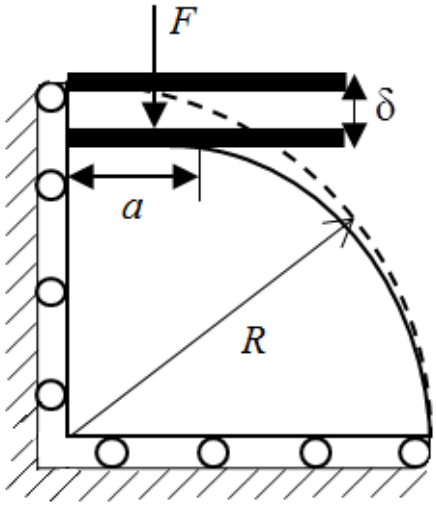

Fig. 2.3 A hemispherical asperity with radius, R, before and after loading, showing the contact radius, a, the displacement, δ, and the load, F.

The creep constant C_1 in the Garofalo formula shows the characteristic time scale in the creep process, and the results are presented with respect to this scaled time:

$$\tau = t / t_1 = t \frac{EC_1}{H} \tag{2.25}$$

Table 2.1 Overview of the parameter ranges used for FE simulation [1]

Run No.	Varied parameter	Range
1	Reference	$R = 1\ mm$, $E = 200\ GPa$, $\upsilon = 0.33$, $\sigma_Y = 400\ MPa$, $(C_1 = 10^{-4} s^{-1})$, $C_2 = 10/\sigma_Y$, $\delta = 100\delta_c$
2	Radius R	$0.1 - 10\ mm$
3	Interference δ	$25\delta_c - 600\delta_c$
4	Poisson's Ratio υ	$0.28 - 0.38$
5	Yield stress σ_Y	$200 - 2000\ MPa$
6	Young's Modulus E	$70 - 300\ GPa$
7	MCL parameters C_1, C_2	$C_1 = 10^{-3} - 10^{-5} s^{-1}$, $C_2 = 5 - 15/\sigma_Y$

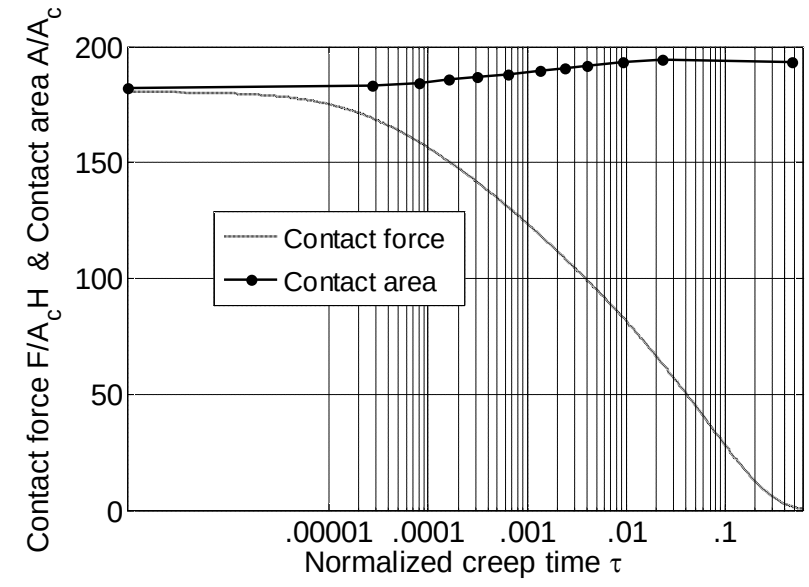

(a)

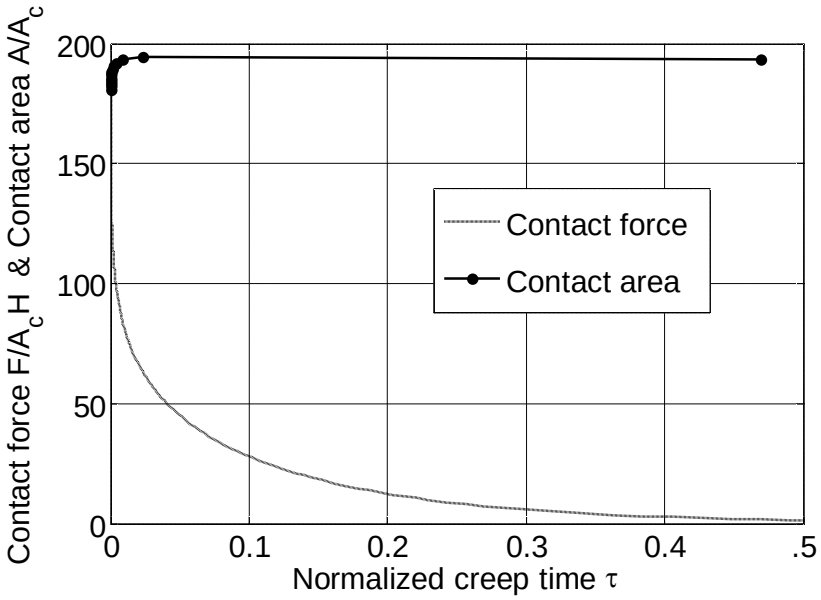

(b)

Fig. 2.4 Relaxation of force (solid line) and evolution of contact area (dashed line) with respect to normalized creep time in a (a) logarithmic and (b) conventional scale.

In Fig. 2.4 the contact force, F, and the contact area, A, dependence on τ for reference parameters (set number 1 in Table 2.1) are shown. It can be seen that the contact area after an initial rise of about 7%, remains nearly constant. The contact force, on the other hand, shows a steep initial reduction and a slowing creep rate as time increases.

The finite element simulations include two steps: (i) Displacing the rigid flat to reach a predefined interference, δ, as shown in Fig. 2.3, and then, (ii) Stress relaxation occurs at this fixed interference. The Jackson and Green [19] formulas for elasto-plastic hemispherical contact can be used to obtain the state of the sphere before creep initiates (Step (i)). Using the Garofalo creep Eq. (2.24) and considering the fact that the total strain is constant at ε_0 because of the fixed interference boundary condition, the following equation can be obtained for the contact area as it changes in time due to creep.

$$A(t) \approx A_0\left[1-(1-2\xi)\left(\varepsilon_0-\frac{2}{EC_2}\operatorname{arctanh}\left(-C_1C_2t+\xi\right)\right)\right] \tag{2.26}$$

where A_0 is the initial contact area before creep starts, and ξ is an integration constant. So a time evolution law for the change in contact area ΔA is

$$\frac{\Delta A(t,C_2,\nu)}{A_0}=\frac{\Delta A(C_2,\nu)}{A_0}\left[1-2c(p_1,p_2)\operatorname{arctanh}\left\{\exp(-p_1\varepsilon(t)+p_2)\right\}\right] \tag{2.27}$$

where

$$c(p_1,p_2)=\left[2\operatorname{arctanh}\left(\exp(p_2)\right)\right]^{-1} \tag{2.28}$$

to set $\Delta A(t=0)=0$. p_1 and p_2 are the fit parameters and their values for the example material properties listed in Table 2.1 are given as:

$$p_1=27\pm5 \quad \text{and} \quad p_2=-(1\pm0.4)\times10^{-3} \tag{2.29}$$

The pressure rate or relaxation rate for the second step (ii) is obtained from the following equation

$$\dot{p}(p) = -\sum_{i=1}^{2} A_i \sinh(\alpha_i p) \tag{2.30}$$

The A_i and α_i are dependent on input parameters such as the fixed interference, δ, the asperity radius, R, etc., and are obtained by curve fitting to accurate numerical or experimental results. Extending Eq. (2.30):

$$-\dot{p} = A_1 \sinh(\alpha_1 p) + A_2 \sinh(\alpha_2 p) \tag{2.31}$$

where the constants A_i and α_i are obtained using the following empirical equations:

$$\begin{pmatrix} A_1 \\ A_2 \end{pmatrix} = EC_1 \left\{ \begin{pmatrix} 2.933 \pm 0.076 \\ -0.035 \pm 0.019 \end{pmatrix} + C_2 \sigma_Y \begin{pmatrix} 0.001 \pm 0.010 \\ 0.089 \pm 0.002 \end{pmatrix} \right\} \tag{2.32}$$

$$\begin{pmatrix} \alpha_1 \\ \alpha_2 \end{pmatrix} = \frac{1}{H} \left\{ \begin{pmatrix} 0.43 \pm 0.14 \\ 3.43 \pm 0.23 \end{pmatrix} + C_2 \sigma_Y \begin{pmatrix} 0.57 \pm 0.02 \\ 0.85 \pm 0.03 \end{pmatrix} \right\} \tag{2.33}$$

The second case that is considered here is creep under the constant force boundary condition as described by Brot et al. [11]. In reference [11], a polymeric bio-material is used to model the single hemispherical asperity, and they also used a simplified form of the modified time hardening law (Eq. 2.22) for their model because it predicts the experimental results for polymers very well. Since bio-materials are used over a narrow range of temperatures, the temperature dependency can be ignored. Therefore, by substituting the simplified from of Eq. (2.22) into a sum of the different components of the strains (Eq. 2.23) gives:

$$\varepsilon = \varepsilon_{elastic} + \varepsilon_{cr} = \frac{\sigma}{E} + \overline{C}_1 \sigma^{C_2} t^{C_3} \tag{2.34}$$

The above equation is called the simplified modified time hardening law (MTH) where E is the linear elastic modulus of the polymer and the parameter $\overline{C}_1$ is defined as:

$$\overline{C}_1 = \frac{C_1}{(C_3 + 1)} \tag{2.35}$$

Brot et al. [11] found the following equations for the creep displacement and creep contact area using Eq. (2.34), and by performing a parametric analysis to study the effect of the various variables obtained:

$$\omega_{cr}(t) = \omega_{cr}(t_r)\left(\frac{t}{t_r}\right)^{(0.71C_3+0.03)} \tag{2.36}$$

$$A_{cr}(t) = C_2 \pi R \omega_{cr}(t_r)\left(\frac{t}{t_r}\right)^{(0.71C_3+0.03)} \tag{2.37}$$

In the above equations $\omega_{cr}(t)$ and $A_{cr}(t)$ are the time dependent creep displacement and creep contact area, respectively. It should be noted that $\omega_{cr}(t_r)$ is the creep displacement at a convenient reference time t_r, R is the radius of the hemispherical asperity, C_2 and C_3 are constants that are calculated by curve fitting to the experimental results. As shown by the equations, Brot et al. [11] found a linear relation between the area evolution $A_{cr}(t)$ and interference $\omega_{cr}(t)$.

In this work, the time dependent deformation of a sinusoidal asperity under the constant interference (stress relaxation) and the constant force (creep) boundary conditions are modeled using FE simulations. In the next section, it is shown how this model is implemented in ANSYS.

CHAPTER 3

METHODOLOGY

3.1 Introduction

The finite element method that is used to model the effect of stress relaxation and creep in single asperity contact is discussed in this chapter. Firstly, the model for the static deformation or the stress build-up stage is developed and explained in detail. The results in this stage are compared to previous works in the literature to verify the model. Next, the model is extended to include the effect of the stress relaxation and creep. The rigid flat surface is displaced or loaded to a predefined value, and transient results for both constant force and constant displacement boundary conditions are presented and discussed.

3.2 Modeling and Simulation of the Static Deformation Step (Load Step 1)

The three dimensional sinusoidal geometry with a wavelength of λ, and amplitude of Δ is shown in Fig. 3.1. Due to the symmetry that exists in the sinusoidal geometry of the asperity, only one quarter of this geometry is used in the finite element method.

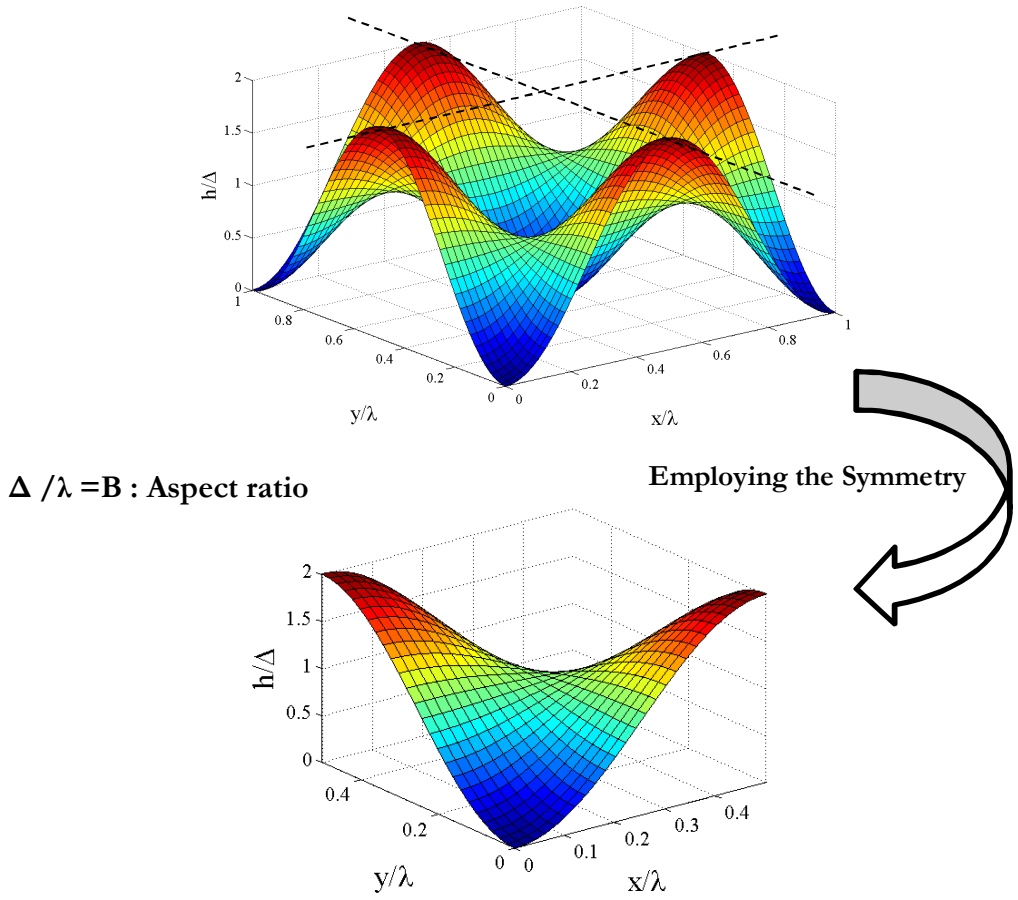

Fig. 3.1 Three-dimensional plot of the sinusoidal surface

The three-dimensional sinusoidal surface is generated in the commercial software ANSYS™ 13.0 package using APDL coding. APDL is the acronym of "ANSYS Parametric Design Language" which is an alternative to the GUI (Graphical User Interface) to perform modeling in ANSYS. Since generating a sinusoidal asperity via GUI in ANSYS is very tedious, we used APDL instead.

The steps that are used to create the sinusoidal asperity in ANSYS are shown in Fig. 3.2. First, the keypoints are developed using Eq. (2.1) (Figure 3.2a). Then using these keypoints, the

lines are formed between them (Figure 3.2b). After that, using every four lines, small areas are created. Combining all of these small areas together, the sinusoidal surface is created (Figure 3.2c). Finally, this sinusoidal surface cuts a rectangular prism block to create the sinusoidal asperity (Figure 3.2d).

Solid186, which is a 20-node brick element, is used for the meshing of entire volume of the sinusoidal asperity. Hexahedral elements are used and the "sweep" option is implemented to mesh the sinusoidal asperity. By performing a mesh convergence for different numbers of elements, it was observed that a total number of 52,802 elements gives reasonable results. The rigidity of the flat surface is acquired by using a single element to mesh this surface (this method is used in current work), or we can use an elastic modulus value for the rigid flat surface which is several orders of magnitude higher than the one used for the sinusoidal asperity. Next, the sinusoidal asperity is put into contact with a rigid flat surface. Conta174 and Targe170 elements are used to form the contact pair to model interaction between the surfaces. The "augmented Lagrange method" is used as the algorithm of contact model. The normal penalty stiffness is set to 100, and the penetration tolerance is set to 0.01 in the contact model.

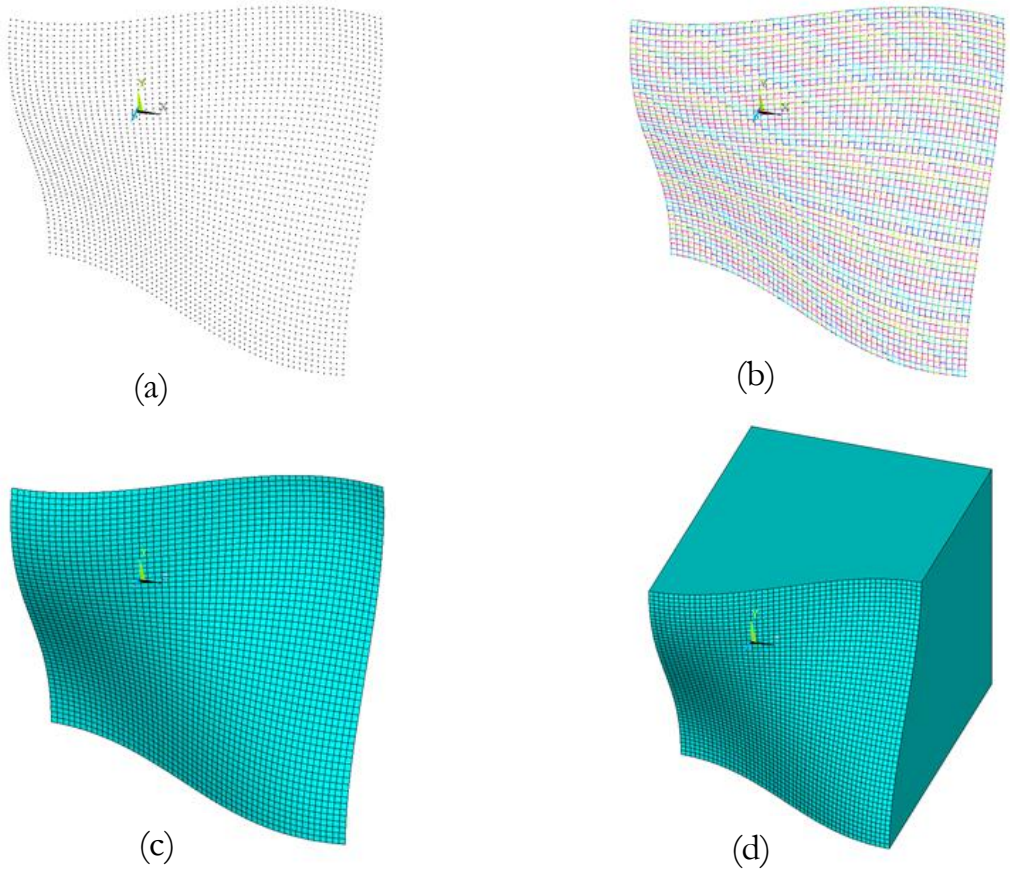

Fig. 3.2 The steps to create the sinusoidal asperity: (a) creating the keypoints, (b) creating the lines, (c) creating the sinusoidal surface, and (d) adding volume to the sinusoidal surface

The boundary conditions which are used for the sinusoidal geometry and the rigid flat surface are listed below:

1) Zero displacement is applied in the normal direction of all of the side surfaces of the sinusoidal geometry due to the symmetric boundary condition. The bottom surface is constrained in all directions.

2) The rigid flat can only displace in the z direction i.e. the displacement in the x and y directions and the rotation about all of the axes are held to zero. Contact between the sinusoidal asperity and the rigid flat is accomplished by applying a displacement on the rigid flat surface or by inserting a constant force in the z direction on the flat surface depending on if transient behavior under a constant displacement boundary condition (stress relaxation) or under a constant force boundary condition (creep) is considered.

The meshed sinusoidal geometry and the rigid flat along with the boundary conditions used for the side and bottom surfaces are shown in Fig. 3.3.

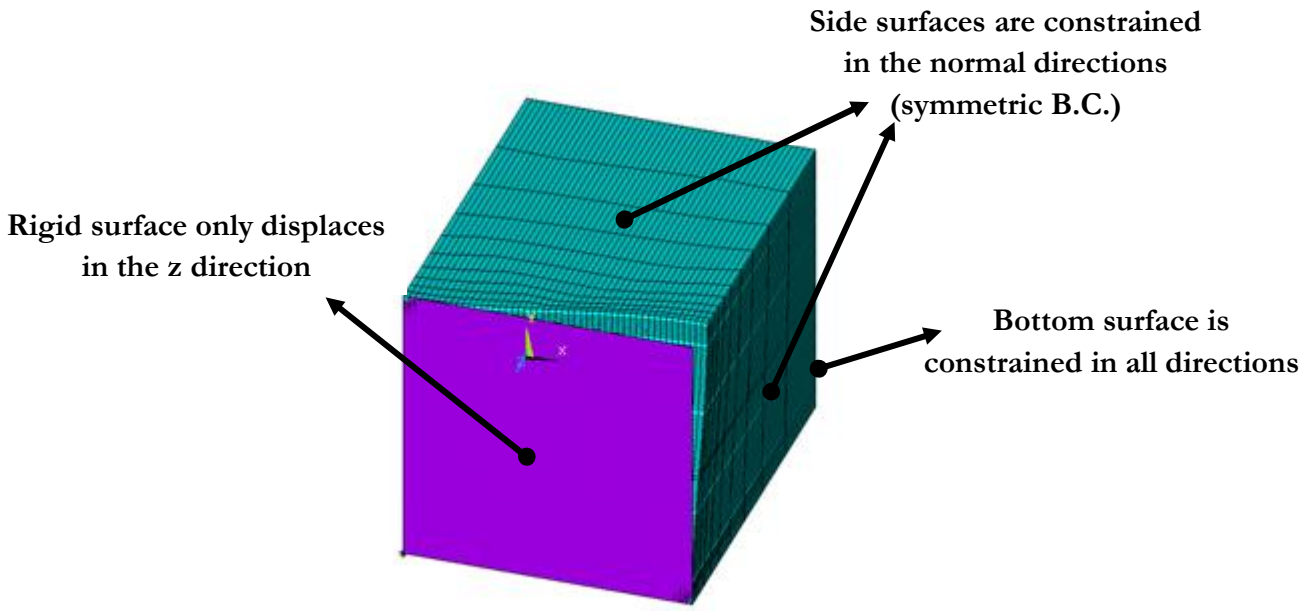

Fig. 3.3 The element plot of the sinusoidal asperity and the rigid flat including the boundary conditions that are used for the geometry

In the first load step, the sinusoidal geometry should be pressurized. There are two ways to do this which depends on the boundary condition under which the time dependent deformations are considered. If the transient case under a constant force boundary condition (creep) is considered then a predefined force should be applied to the rigid surface, and if constant displacement boundary condition (stress relaxation) is considered then the rigid surface should be displaced toward the sinusoidal surface to a predefined value. This occurs before any time steps are taken.

By determining the contact status and contact pressure of each node during post-processing, the total number of nodes in contact is obtained from the nodal solution for incremented values of displacement. The ratio of the number of nodes in contact to the total number of nodes over the surface gives the real area of contact normalized by the apparent or nominal area of contact. The average surface separation is also obtained by averaging over the contact gap of non-contacting nodes. It should be noted that the effect of the boundary nodes is considered in averaging.

The results in the first load step are equivalent to the static deformation investigated by Johnson et al. [2] for the elastic case and Krithivasan and Jackson [27] for the elasto-plastic case. The FEM results of the current model for the static deformation stage are compared with these works for validation.

3.3 Verification of the Model Accuracy (Elastic Case)

Verification of the model accuracy is achieved by comparing the FEM results for the elastic case with the Johnson et al. data [2] and the Jackson and Streator fit [34] (Fig. 3.4). In order to compare our results for the elastic case with the work by Jackson and Streator [34], the same material and geometrical properties are chosen for the sinusoidal asperity. For the elastic case, $E = 200GPa$ and $\upsilon = 0.3$ (these values are for a steel type material) are used in the FE model.

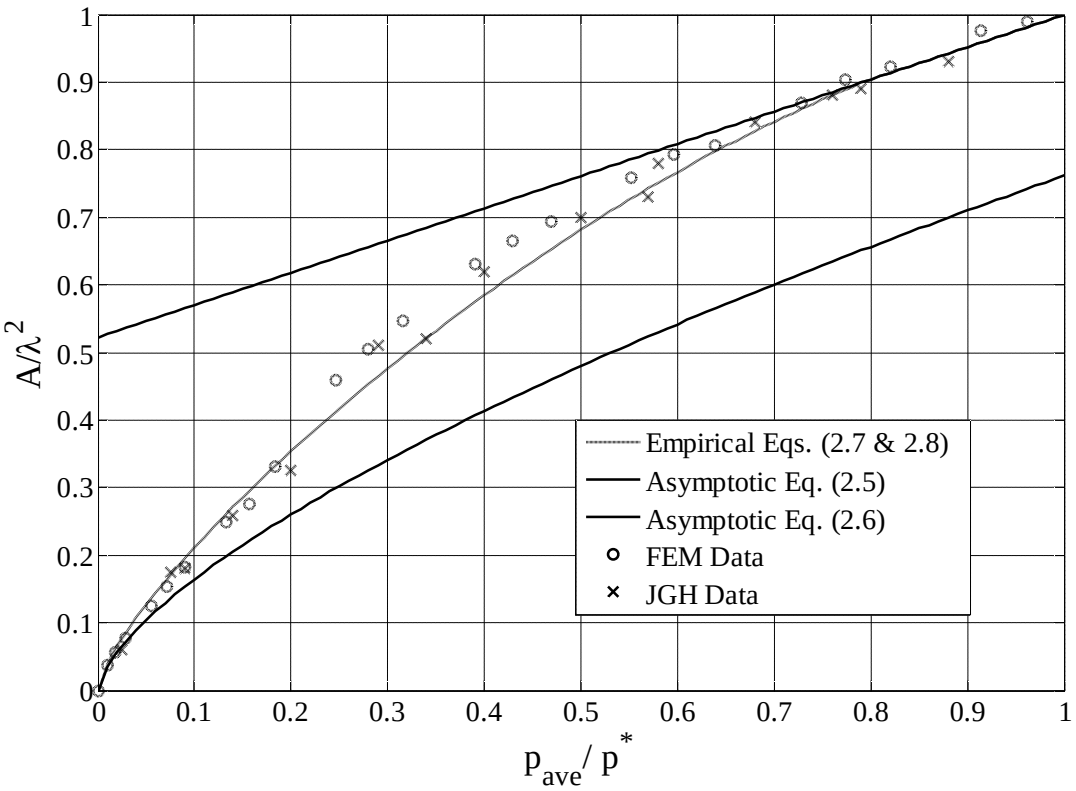

Fig. 3.4 Comparison of the elastic FEM contact area results with JGH data and Jackson-Streator empirical equation

As it is shown in Fig. 3.4, the FEM data differs from the empirical Eqs. (2.7 & 2.8) by an average error of 5%, but appears to compare better with the data provided by Johnson et al [2].

3.4 Verification of the Model Accuracy (Elasto-plastic Case)

The elasto-plastic results are also compared to the empirical equation developed by Krithivasan and Jackson (KJ) [27]. The material of the sinusoidal surface for the elasto-plastic case is assumed to be bi-linear isotropic hardening solid with an elastic modulus, E, of $200\ GPa$, Poisson's ratio, υ, of 0.3, yield strength, S_y, of $1\ GPa$ and a tangent modulus, E_T, of 2% of the elastic modulus, E. This low value of E_T has been shown to have a negligible effect on the results (the results are applicable to the cases of elastic-perfectly plastic materials). The hardening was used to help enhance convergence. The contact area results versus contact pressure in comparison with the Eq. (2.11) are shown in Fig. 3.5. In Fig. 3.5, the FEM data differs from the empirical Eq. (2.11) by an average error of 4%.

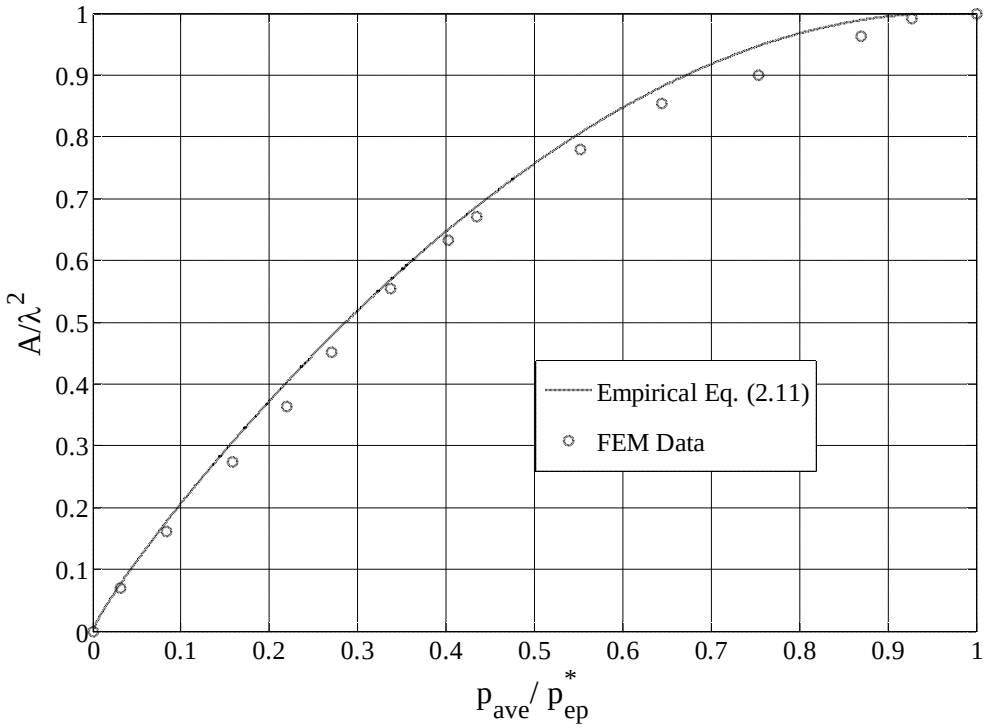

Fig. 3.5 Comparison of the elasto-plastic FEM contact area results with empirical equation provided by Krithivasan and Jackson

Also, the FEM surface separation results for both the elastic and elasto-plastic cases are obtained, and the elastic results are compared to the JGH data [2]. Empirical equations for both the elastic case and elasto-plastic case are also developed.

3.5 Surface Separation Results for the Elastic Case

Finite element results for the normalized average surface separation, G, for the elastic case are shown in Fig. 3.6. The numerical results developed by JGH [2] along with their asymptotic solutions are also shown. The following empirical equation is developed for the elastic case which is also shown in Fig. 3.6.

$$G = \left(1 - \sqrt{P_e}\right)^{5/2} \tag{3.1}$$

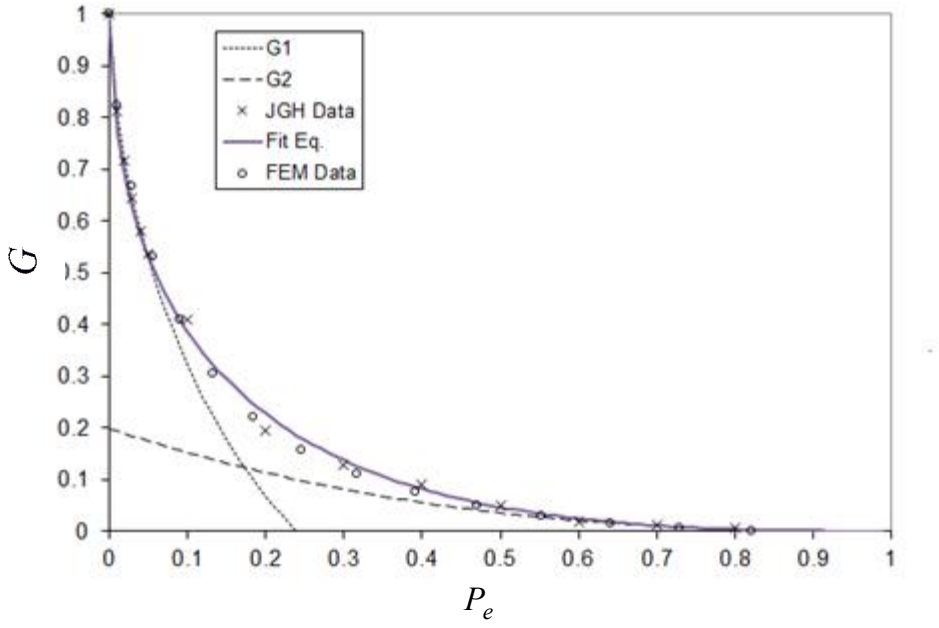

Fig. 3.6 Comparison of the FEM elastic results for average surface separation (shown by circles) with the JGH data (shown by crosses) and the new fit given by Eq. (3.1) (shown by solid line)

In Fig. 3.6, the FEM data differs from the empirical Eq. (3.1) by an average error of 3.4%. This shows that the elastic FEM results agree well with the JGH data [2]. In the next section, the model is extended to consider the plastic deformation, as well.

3.6 Surface Separation Results for the Elasto-plastic Case

Using the same material properties as in section 3.4, the average surface separation results for different values of aspect ratio, Δ/λ, and yield strength, S_y, values are shown in Figs. 3.7 and 3.8.

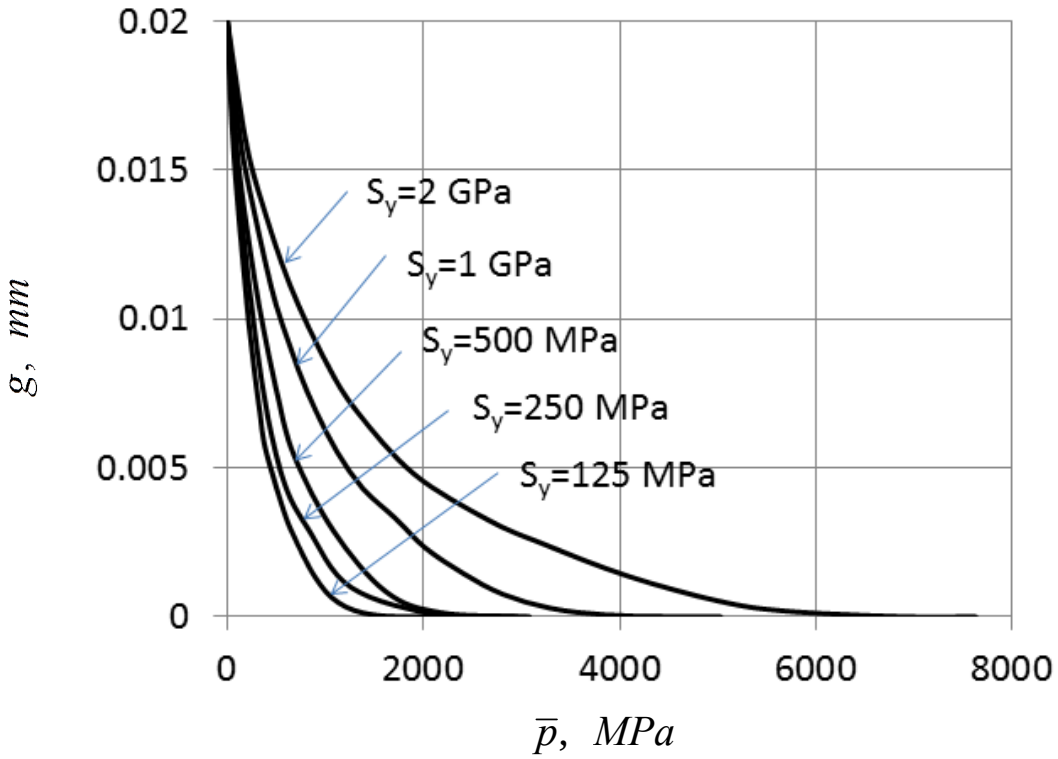

Fig. 3.7 The FEM elasto-plastic results for average surface separation for various yield strengths

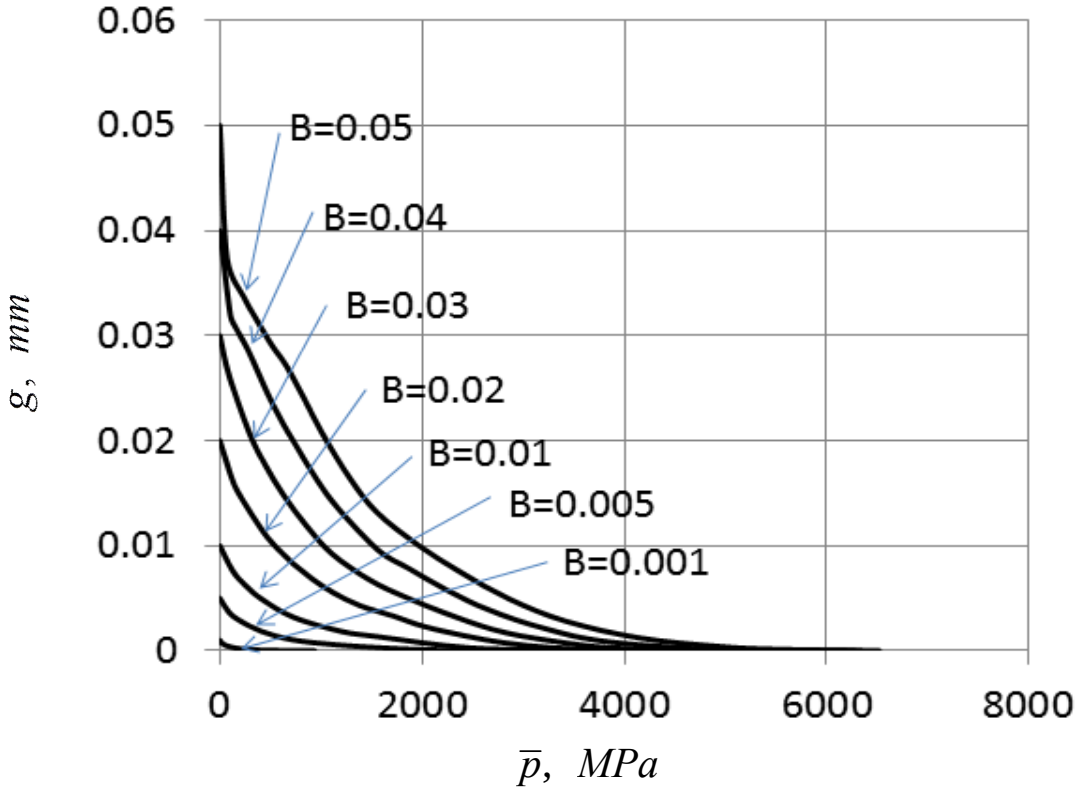

Fig. 3.8 The FEM elasto-plastic results for average surface separation for various aspect ratios

It should be noted that the results in Figs. 3.7 and 3.8 are not normalized so that the differences between the different cases can be more easily discerned. Similar to Eq. (3.1) for the elastic case, an empirical fit is now introduced for the elasto-plastic case and follows the same general form, except that the $\frac{\bar{p}}{p_{ep}^*}$ is to the power of a varying quantity which also depends on $\frac{\bar{p}}{p_{ep}^*}$, $\frac{S_y}{E'}$, and B. Here additional normalized variables are also introduced as $P_{ep} = \frac{\bar{p}}{p_{ep}^*}$, $\varepsilon_y = \frac{S_y}{E'}$, and $B^* = \frac{B}{B_c}$. The empirical Eq. is:

$$G = \left(1 - \left(P_{ep}\right)^{A_1 P_{ep} + A_2}\right)^{5/2} \tag{3.2}$$

where A_1 and A_2 are given by

$$A_1 = -0.08 \ln\left(B^*\right) \tag{3.3}$$

$$A_2 = \frac{1}{15}\left(B^* - 1\right)^{0.44} + 0.99 \; {}^{0.41\left(B^* - 1\right)} - \frac{1}{2} \tag{3.4}$$

Eqs. (3.2-3.4) differ from the FEM data by an average 3.8% (Fig. 3.9) in the range of $5.69 \cdot 10^{-4} \le \varepsilon_y \le 9.1 \cdot 10^{-3}$ and $10^{-3} \le B \le 5 \cdot 10^{-2}$. This range is comparable to the values typically encountered on the asperities of metallic rough surfaces, but was limited by the finite element methodology. It is difficult to obtain results outside of this range due to problems with obtaining solution convergence and having an adequate mesh density. It should be mentioned that as B^* approaches 1, Eq. (3.2) becomes identical to Eq. (3.1) for the perfectly elastic case.

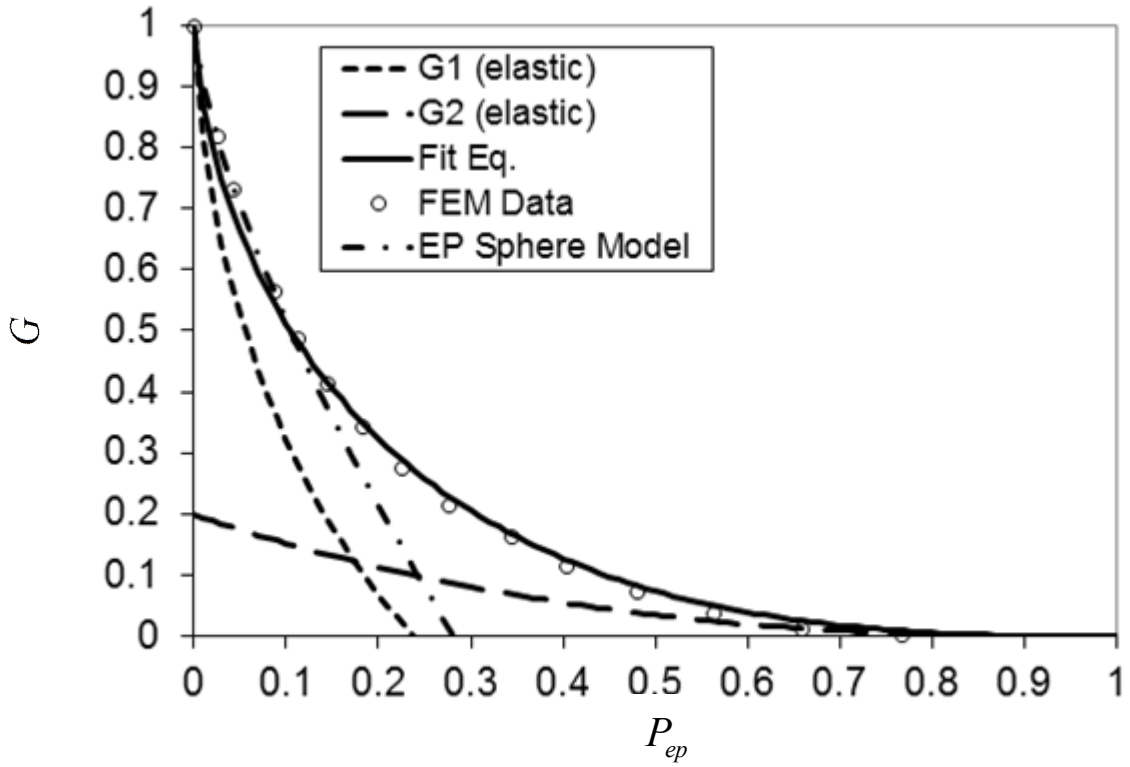

Fig. 3.9 The comparison of FEM elasto-plastic results for average surface separation (shown by small circles) with the new fit given by Eq. (3.2) (shown by solid line).

As shown, the FE model results agree with both the previous elastic and elasto-plastic empirical models [27, 28, 34] for the static case. The next step is to install the transient effects (stress relaxation and creep) into the FE model.

3.7 Modeling and Simulation of the Stress Relaxation and Creep Effects (Load Step 2)

When the first load step or "static deformation" stage is completed, the second load step begins and the effect of stress relaxation and creep are studied. In ANSYS, the time is set to zero at the beginning of the second load step which is now transient, and the creep effect is activated.

There are several built-in empirical equations in ANSYS that can be employed to investigate the stress relaxation and the creep behavior of materials. In this work, the Garofalo equation (hyperbolic sine power creep law) is used. The built-in Garofalo equation in ANSYS is given below which has a few extra terms not given in Eq. (2.20):

$$\dot{\varepsilon}_{cr} = \tilde{C}_1 \left[sinh(\tilde{C}_2 \sigma) \right]^{\tilde{C}_3} e^{-\tilde{C}_4/T} \tag{3.5}$$

In this equation, $\tilde{C}_1$, $\tilde{C}_2$, $\tilde{C}_3$, and $\tilde{C}_4$ are all constants. Here, a constant temperature is assumed, and $C_1 = \tilde{C}_1 e^{-\tilde{C}_4/T}$ which results in Eq. (3.5) reducing to Eq. (2.20). In the creep theory by Persson [10], the exponential relation for creep is presented as the high-stress limit case of his theory and a linear formula is presented as the low stress limit. Following Persson's idea, it is assumed $n = \tilde{C}_3 = 1$ in Eqs. (2.20) and (3.5) which can be seen as a good quasi-static approximation to Persson's creep law. This assumption is a minor limitation for high stress creep because a change in the creep parameter $\tilde{C}_2{}' = n\tilde{C}_2$ has the same effect as a change in the exponent n or $\tilde{C}_3$. So, the final form of $\dot{\varepsilon}_{cr} = C_1 sinh(C_2 \sigma)$ is used in the stress relaxation and creep analysis where the strain rate depends on the stress level and the two constants C_1 and C_2. The Garofalo constant C_2 determines how sensitive the creep or relaxation rate is to the absolute stress value, i.e., how much faster the material creeps or relaxes due to higher local stress. The constant C_1 defines the characteristic time scale $\tau \propto 1/C_1$ and is used to normalize the time when analyzing the results. Although neglected in this work, in reality, C_1 usually varies exponentially with the temperature, T, i.e. $C_1 = C_1' \exp(-Q_{cr}/kT)$,

where Q_{cr} is the activation energy for creep. All results are presented using this non-dimensional scaled time.

$$\tau = t\frac{EC_1}{p_{ep}^*} \tag{3.6}$$

In Goedecke and Mock's work [1], hardness, H, has been used in the normalized time expression (Eq. 2.25) instead of p_{ep}^*. In this work, p_{ep}^* is a more logical choice than hardness, H, since hardness is essentially meaningless in sinusoidal contacts [27, 28, 55].

As mentioned before, two boundary conditions are considered for modeling the time dependent deformations. A typical simulation for stress relaxation or creep takes approximately 1 day on a 3.4 GHz Intel® Core™ i7-200 assuming $t = 500s$ for the second load step.

CHAPTER 4

RESULTS

4.1 Introduction

In this section the contact area and contact pressure results of the stress relaxation and creep model built in ANSYS are presented and discussed. As stress relaxation or creep happens, the stress distribution in the loaded asperity starts to reduce over time which causes an increase in the contact area. For the constant force boundary condition (creep), the sinusoidal asperity will continue to flatten with time until the stress relaxes. In contrast, for the constant displacement boundary condition (stress relaxation), the contact force will decrease over time until the stress has relaxed. A parametric study is performed to study the effects of different parameters on the contact area and contact pressure results. Finally, empirical equations are developed based on the transient contact area and contact pressure results while including stress relaxation and creep.

4.2 Stress Relaxation Results

In this section, the stress relaxation of the sinusoidal asperity which is pressurized by the displacement of the rigid flat surface in the first load step is studied. During the second load step the rigid flat surface displacement is kept constant (Fig. 4.1), and the contact area and contact pressure are monitored as a function of time. The material and geometrical properties that were used in the previous sections along with the creep parameters given in Table 4.1 are used to obtain a benchmark set of results.

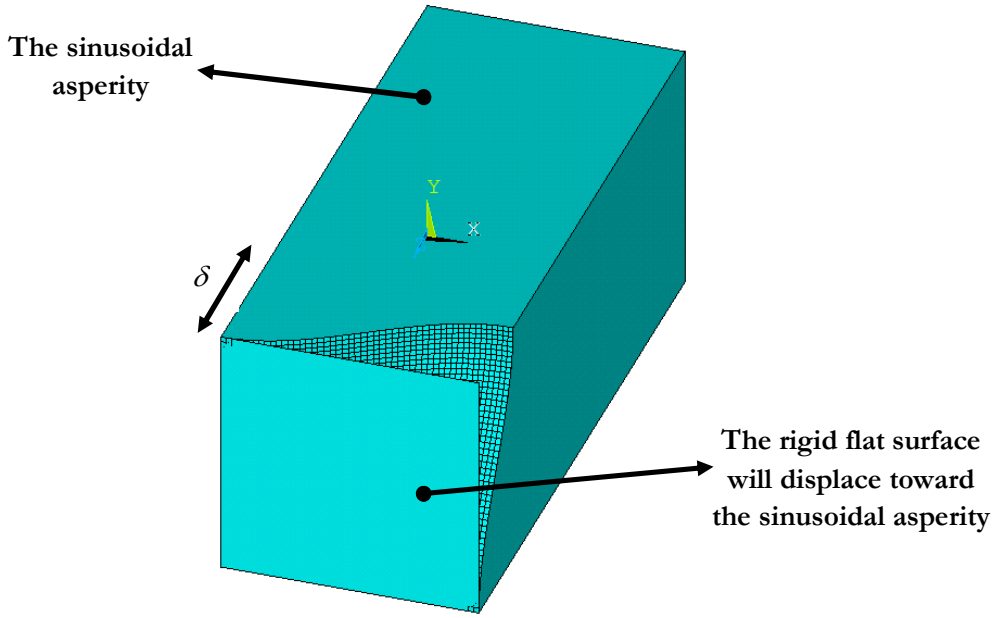

Fig. 4.1 Plot of the three-dimensional sinusoidal asperity and the rigid flat surface under constant displacement boundary condition

The normalized contact area, A/λ^2, and contact pressure, $\bar{p}/p_{ep}^*$, results versus time for the reference properties are shown in Fig. 4.2. It can be seen that the contact area and contact pressure have a steep initial increase and decrease, respectively. As time passes, the normalized contact area, A/λ^2, reaches to 1 (complete contact) with a gradually decreasing rate, and the contact pressure goes asymptotically to zero (it's not shown in Fig. 4.2).

Table 4.1 Reference properties

$E = 200\ GPa,\ \nu = 0.3,\ S_y = 1\ GPa$	$\delta/\Delta = 1$
$C_1 = 10^{-3} s^{-1},\ C_2 = 10/S_y$	$\Delta/\lambda = 0.02$

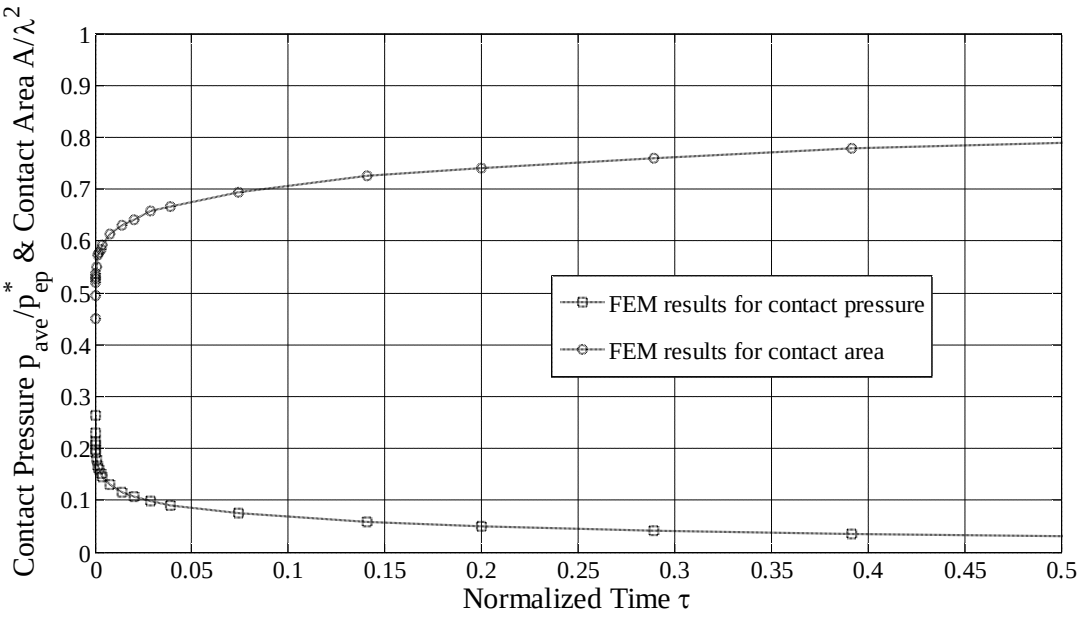

Fig. 4.2 The FEM results for the contact area and contact pressure versus time for reference properties

In the rest of this section, a parametric study is performed to analyze the effect of different parameters on the stress relaxation results. The ranges of variation of different material and geometrical parameters including the constants of the Garofalo equation are given in Table 4.2.

Table 4.2 Overview of the parameter ranges used for the FE simulations (constant displacement B.C.)

Parameter	Range
Average surface separation	$0.0147 \le g_o/\Delta \le 0.5664$
Aspect ratio	$0.01 < \Delta/\lambda < 0.04$
Poisson's ratio	$0.3 < v < 0.4$
Yield strength	$1\ GPa < S_y < 4\ GPa$
Elastic modulus	$100\ GPa < E < 200\ GPa$
Garofalo constants C_1, C_2	$10^{-5}\,s^{-1} < C_1 < 10^{-3}\,s^{-1},\ 5/S_y < C_2 < 15/S_y$

The results for the change of contact area and contact pressure over time for different values of average surface separations which correspond to the rigid surface displacements equal to $\delta/\Delta = 0.5,\ 0.75,\ 0.875,\ 1,\ 1.125,\ 1.25,\ 1.5$ are shown in Figs. 4.3-4.5. In these results, only the initial average surface separation (initial penetration) is varied and the properties in Table 4.1 are used for other parameters.

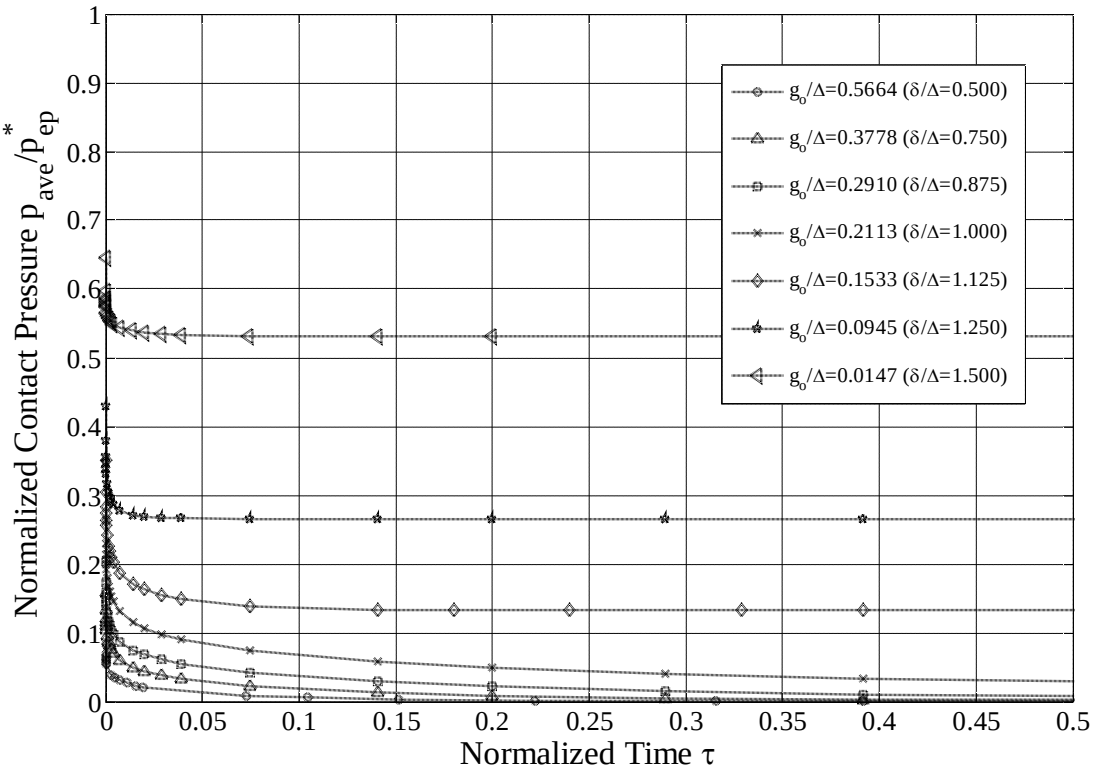

Fig. 4.3 The FEM results for contact pressure versus time for different surface separations (penetrations)

As it is shown in Fig. 4.3, stress relaxation causes the contact pressure to reduce with time for different surface separations which is in agreement with the definition of creep relaxation. It can be seen that for the surface separation values equal to or more than approximately $g_0/\Delta \approx 0.21$ which corresponds to $\delta/\Delta = 1$, the contact pressure goes asymptotically to zero. However, for surface separations less than this value, the contact pressure reduces to a nonzero value. Also, for low surface separations or high loads, the time rate change of contact pressure is more than that at high surface separations or low loads.

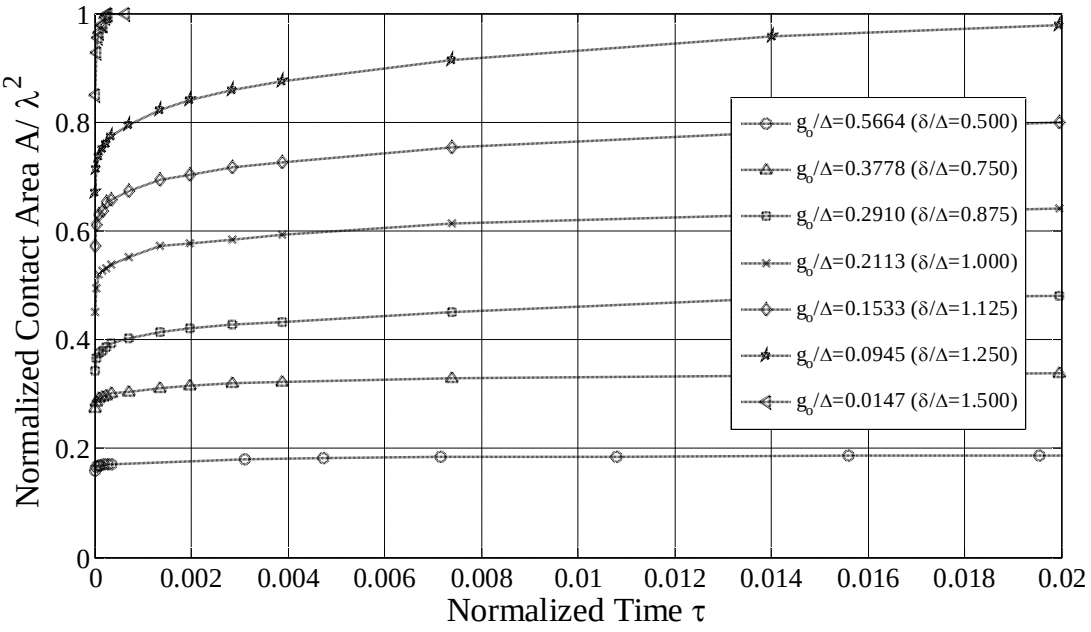

Fig. 4.4 The FEM results for the contact area versus time for different surface separations (penetrations) over a short duration of time

The change of contact area over a relatively short period of time $0 \le \tau \le 0.02$ for different surface separations (penetrations) is shown in Fig. 4.4. The contact area increases with time which again agrees with the definition of the stress relaxation. The contact area for the surface separations equal to or below approximately $g_0/\Delta \approx 0.21$ $(\delta/\Delta = 1)$ increases with time until complete contact occurs $(A/\lambda^2 = 1)$. Although for surface separations higher than this value the contact area increases with time towards an asymptote lower than the complete contact area, and the complete contact condition isn't achieved. In Fig. 4.5, the contact area results over a longer duration of time are shown $(0 \le \tau \le 3)$. Surprisingly, the contact area results for surface separations higher than approximately $g_0/\Delta \approx 0.21$ $(\delta/\Delta = 1)$ or low loads reduce to very small values after an initial increase. It seems that the sinusoidal asperity starts to lose its contact from the rigid flat surface. This

behavior doesn't occur for the surface separations lower than $g_0/\Delta \approx 0.21$. Also, for lower surface separations the time rate change of contact area is higher than that for higher surface separations.

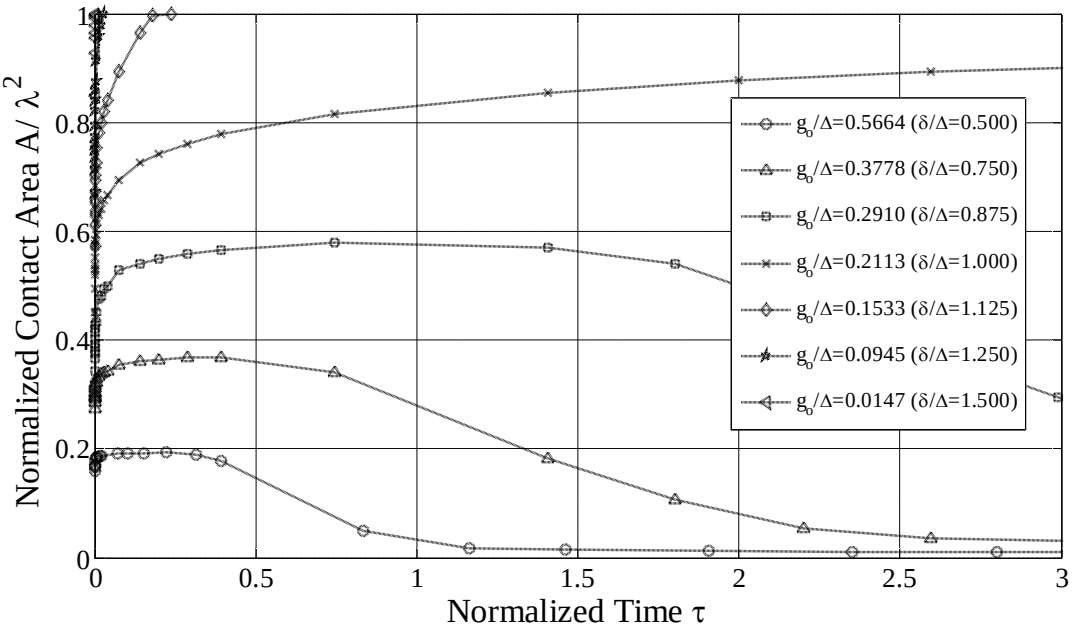

Fig. 4.5 The FEM results for the contact area versus time for different surface separations (penetrations) over a longer duration of time

So, it seems that the approximate surface separation $g_0/\Delta \approx 0.21$ (penetration equals to $\delta/\Delta = 1$) acts like a critical value for this case. Both the contact area and contact pressure behave differently above and below this critical value. For surface separations below this critical value, there is a sudden increase in the contact area within a very small normalized time after which complete contact is acquired ($A/\lambda^2 = 1$). For surface separations higher than this value, complete contact cannot be achieved. Instead, after an initial increase, the contact area decreases with time to a very small value (Fig. 4.5).

Likewise, contact pressure decreases with time and asymptotically approaches zero for surface separations higher than $g_0/\Delta \approx 0.21$ (penetrations lower than $\delta/\Delta = 1$), but for surface separations below than $g_0/\Delta \approx 0.21$ (penetrations higher than $\delta/\Delta = 1$), the contact pressure doesn't go to zero, and instead decreases asymptotically to a finite value (Fig. 4.3). This behavior is expected since the creep strain is similar to the plastic strain i.e. it conserves the volume [56] i.e. Poisson's ratio equal to 0.5 ($\nu_{cr} = 0.5$). Consider that, at low surface separations or high loads the compressed volume is equal to or greater than the vacant volume that exists between the sinusoidal surface and the rigid flat after the penetration (Fig. 4.6). In other words, for surface separations higher than the critical surface separation, the material has enough space to fill into and to relax its stress completely. However, for lower surface separations, the compressed volume exceeds the void volume and there isn't complete stress relief, and the contact pressure approaches a nonzero value.

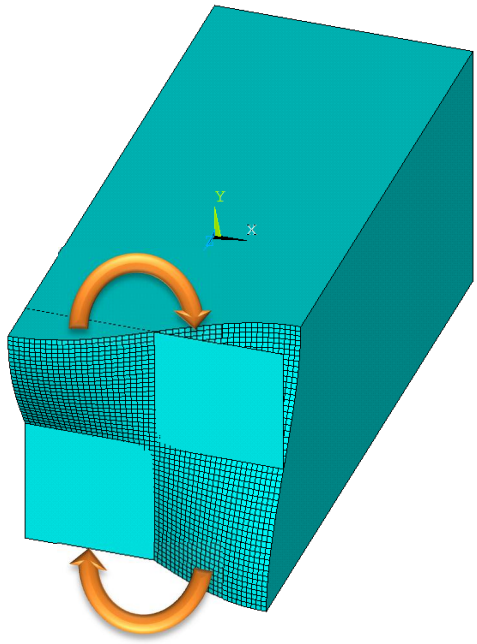

Fig. 4.6 The arrows show how the deformed material displaces to the void volume between the sinusoidal asperity and the rigid flat

In Fig. 4.7, the change of normalized contact area and contact pressure with time is shown for different values of yield strength. The penetration for all cases is the same ($\delta/\Delta=1$). All of the other properties are the same as Table 4.1 except the yield strength which is changing. The value of the initial contact area and contact pressure for each curve is different because yield strength also affects the first load step or stress build-up stage. Although, they each initiate from different points, the contact area and especially contact pressure curves show the same trend for different yield strength values. For the contact pressure results, the curves for the different yield strengths overlap after the initial times. Also, it can be seen that for lower values of yield strength, we have higher contact area which is expected since lower value of yield strength let the material to deform plastically more easily, and it causes higher contact area.

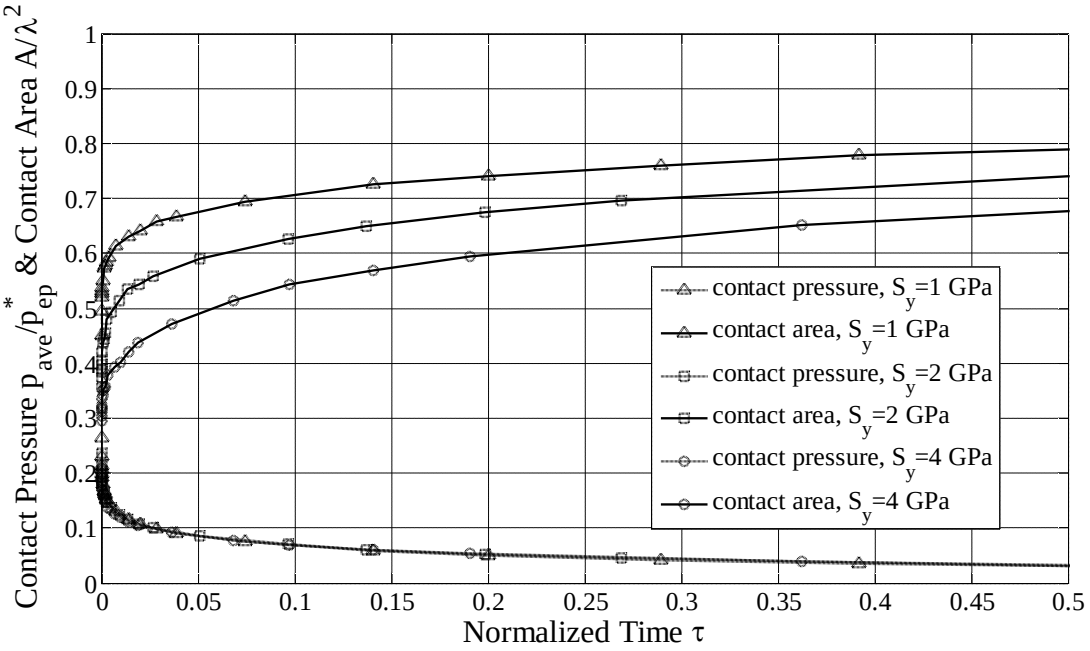

Fig. 4.7 The FEM results for the contact area and pressure versus time for different yield strength, S_y, values

The constant, C_2, in the Garofalo equation is varied in Figs. (4.8-4.10) for a specific penetration ($\delta/\Delta = 1$), and all the other properties are held constant and are the same as the reference properties (Table 4.1). It should be noted that for each value of yield strength in Figs. (13-15) all of the curves start from one point because the Garofalo constant, C_2, doesn't affect the first load step or stress build-up stage. It can be seen for higher values of C_2, that the rate of contact area and contact pressure change is higher (see Fig. 4.8). This was already expected because C_2 shows how much faster the material relaxes or creeps under the high stresses.

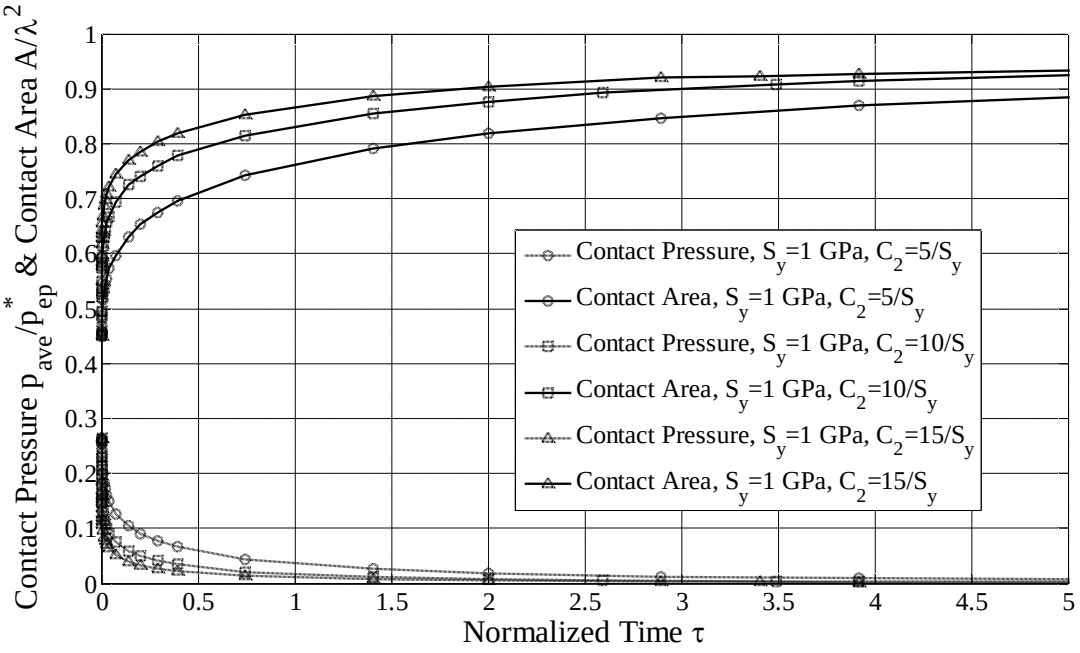

Fig. 4.8 The FEM results for the contact area and pressure versus time for different Garofalo constant, C_2, values ($S_y = 1\ GPa$)

In Fig. 4.9, the yield strength is set to $2\ GPa$. In this case all of the contact area curves for different C_2 values start from a smaller value than the $S_y = 1\ GPa$ case. As mentioned earlier, for a

predefined penetration, $\delta/\Delta = 1$, lower values of yield strength, S_y, let the material to flow more easily under the stress due to yielding and increase the contact area. The initial contact pressure is also lower for a material with $S_y = 2\ GPa$ than a material with $S_y = 1\ GPa$, if all of the other properties are held constant.

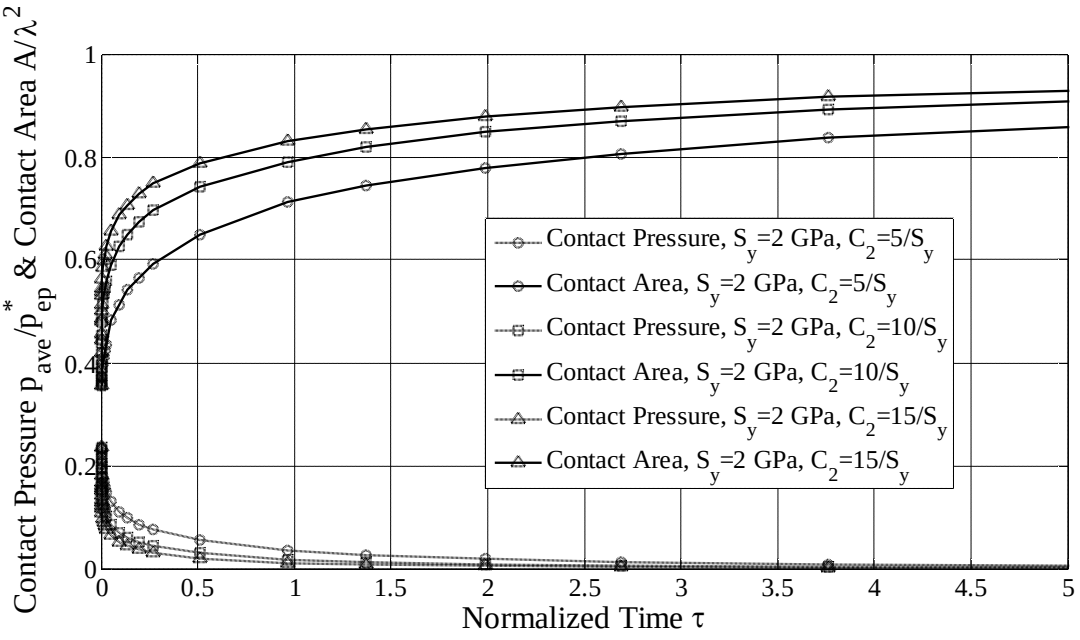

Fig. 4.9 The FEM results for the contact area and pressure versus time for different Garofalo constant, C_2, values ($S_y = 2\ GPa$)

In Fig. 4.10, the yield strength is set to $4\ GPa$. It can be seen that in this case the contact pressure and contact area starts from a smaller value than the case with yield strengths $S_y = 1\ GPa$ and $S_y = 2\ GPa$. Nonetheless, the effect of the Garofalo constant C_2 appears to be similar for all three yield strengths, S_y.

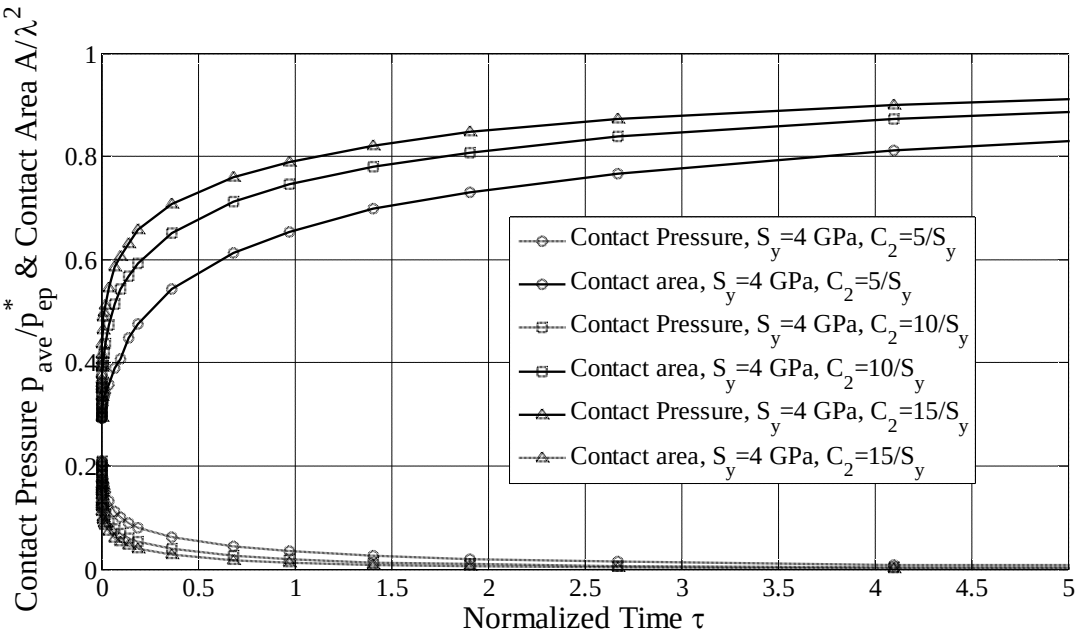

Fig. 4.10 The FEM results for the contact area and pressure versus time for different Garofalo constant, C_2, values ($S_y = 4\ GPa$)

The results for different values of the Garofalo constant C_1 are given in Fig. 4.11. These results show that changing C_1 within the given range in Table 4.2 doesn't affect the contact area and contact pressure results noticeably. This is because the creep time, τ, is proportional to C_1 according to Eq. (3.6). It means that for lower values of C_1, it takes more time to have the same change in contact area and contact pressure. In Fig. 4.11, the creep time for all the cases is $t_{\max} = 500s$, and as the C_1 values decrease, there is no change in the trend of results, but the results become denser within lower values of normalized time, τ. Lines 1, 2, and 3 show when the results end for different cases of $C_1 = 10^{-5}$, $C_1 = 10^{-4}$, and $C_1 = 10^{-3}$, respectively.

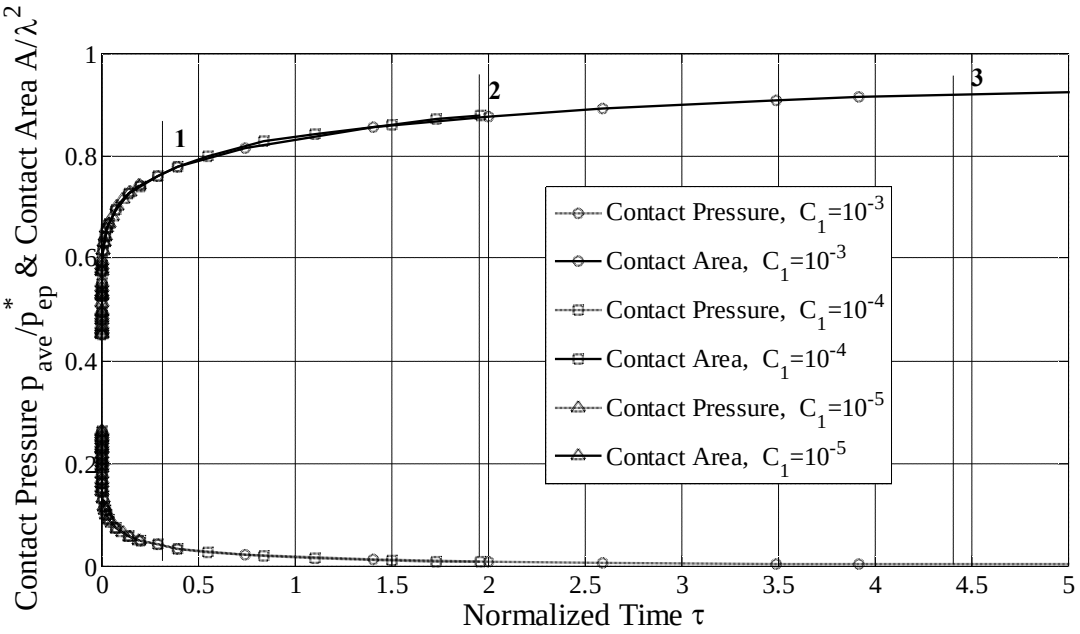

Fig. 4.11 The FEM results for the contact area and pressure versus time for different Garofalo constant, C_1, values

The elastic modulus is also changed within the given range in Table 4.2 in the Fig. 4.12. The initial point, like the yield strength case, is different for each value. For the same penetration of $\delta/\Delta = 1$, the material with the higher elastic modulus creates higher contact pressure and contact area values. This behavior is exactly opposite of the case with yield strength. The contact pressure results collapse while the contact area results stays separated.

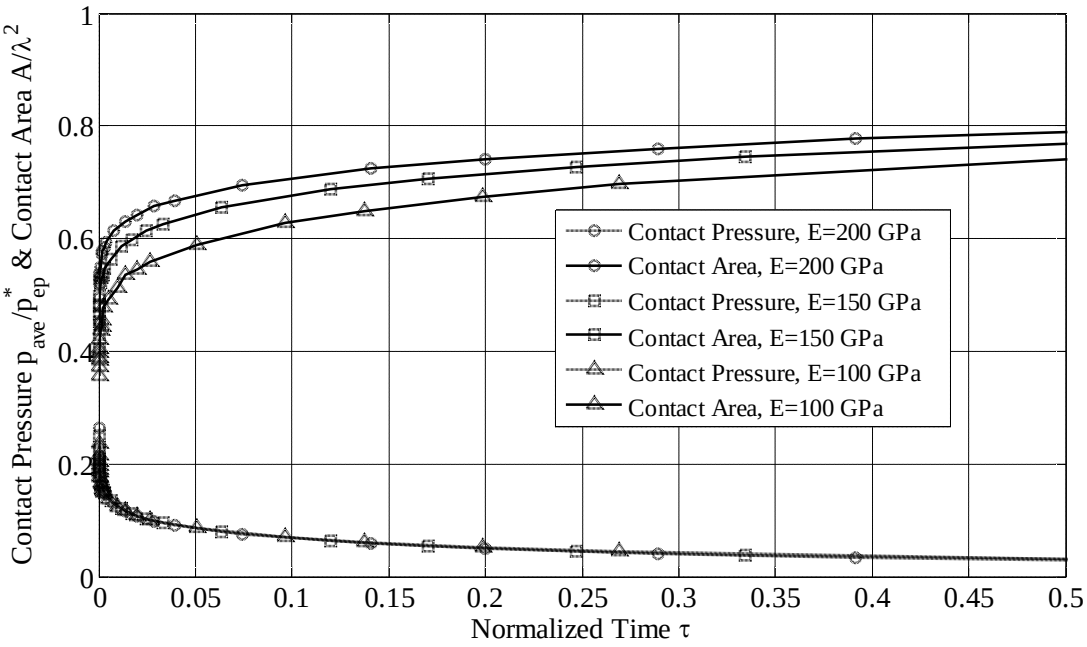

Fig. 4.12 The FEM results for the contact area and pressure versus time for different elastic modulus, E

Results are also generated for two values of Poisson's ratio and are given in Fig. 4.13. Here, again like the elastic modulus and yield strength cases, the starting point is different for each case. The change of the Poisson's ratio has a considerable effect on the starting point of each curve, and the results show that the contact area has a higher dependence on the Poisson's ratio than the contact pressure. It can be seen that higher values of the Poisson's ratio create higher contact area and contact pressures for a specific penetration of $\delta/\Delta = 1$.

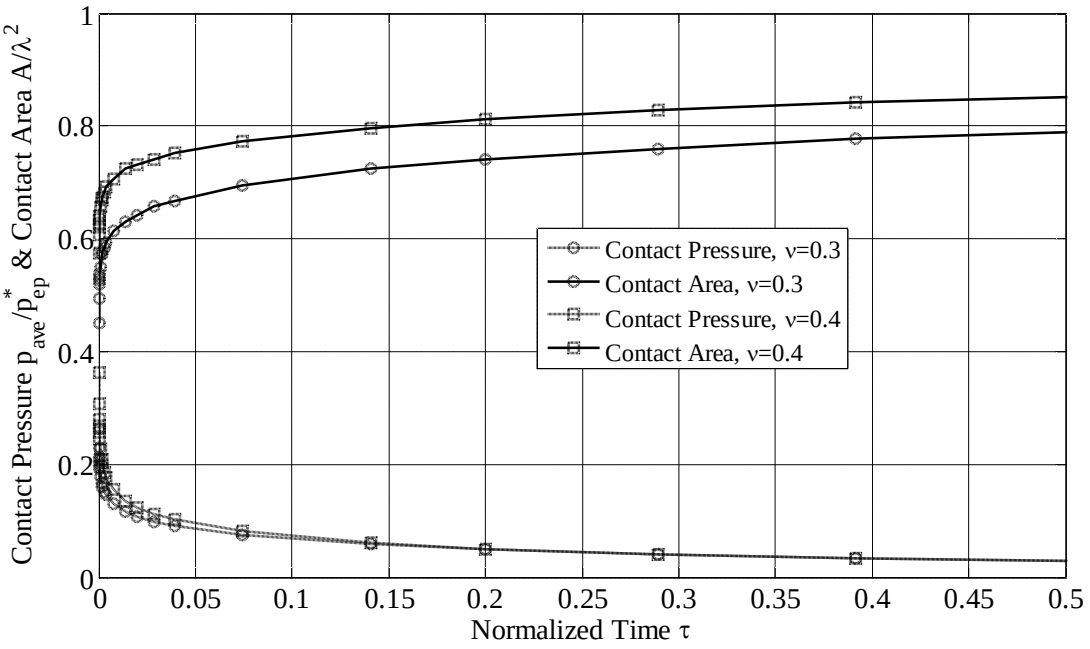

Fig. 4.13 The FEM results for the contact area and contact pressure versus time for different Poisson's ratio, ν

Finally, the aspect ratio, Δ/λ, which is the only geometrical property, is changed in Fig. 4.14 within a very small range as given in Table 4.2. The constant displacement $\delta/\Delta = 1$ is the same for all cases. Again, in this case, the starting point is different for different aspect ratios. As it is shown in Fig. 4.14, the aspect ratio has a significant influence on the contact area. It can be seen that the lower change in contact area $A_{cr} = (A_\tau - A_0)$ is obtained for a higher value of aspect ratio, Δ/λ. This is because a larger aspect ratio, Δ/λ, increase A_0 and hence, reduces the stress levels during the stress relaxation phase. It is apparent from Fig. 4.14 that the normalized contact pressure results overlap for this case.

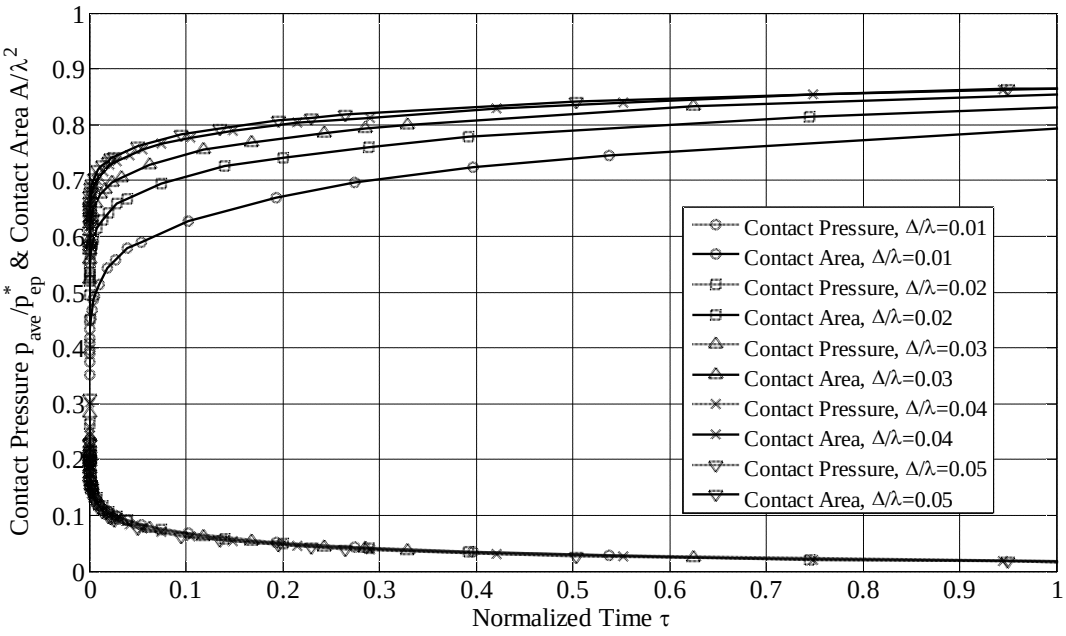

Fig. 4.14 The FEM results for the contact area and pressure versus time for different aspect ratios, Δ/λ

4.3 Empirical Equations for the Stress Relaxation Case

Due to the high number of parameters which affect the stress relaxation results, developing a general relation that considers the effects of all of these parameters is very difficult. For simplicity, the variation of material properties isn't considered in developing empirical equations in this work. The material properties are the same as the reference properties $(E = 200\ GPa,\ \nu = 0.3,\ S_y = 1\ GPa)$. However, the empirical equations consider the effect of the Garofalo constants, C_1 and C_2, the aspect ratio of the sinusoidal asperity, Δ/λ, and the average surface separation, g_0/Δ, between the rigid flat and the sinusoidal asperity.

Since the aimed application of this study is to investigate the effects of stress relaxation and creep in static friction, the maximum time for consideration of the contact area and contact pressure change can be estimated for practical purposes. It is assumed an asperity with a wavelength λ equal to $1\ mm$, with an interaction time of $5\ s$ would be achieved for a speed of roughly $v = 2 \times 10^{-4}\ m/s$, which compares favorably with the literature [9]. Therefore, the empirical equations for the variation of contact area and contact pressure are considered within a time period of 5 seconds ($t_{max} = 5\ s$). Therefore, the stress relaxation (creep) can be considered responsible for the time-dependent dry friction of certain metallic materials.

4.3.1 Empirical Fit for Contact Area

According to the trend of contact area results, a power equation is used to fit the results. This relation is given in Eq. (4.1).

$$\frac{\Delta A_{cr}}{A_0} = \frac{(A_\tau - A_0)}{A_0} = a\tau^b \tag{4.1}$$

where $A_\tau = f(g_o/\Delta,\ \Delta/\lambda,\ C_2,\ \tau)$, a and b are constants which are functions of surface separation, g_o/Δ, aspect ratio, Δ/λ, and Garofalo constant, C_2, and A_0 is given in Eq. (2.11). Note that $A = A_0$ in Eq. (2.11).

For aspect ratio $\Delta/\lambda = 0.02$ and Garofalo constant $C_2 = 10/S_y$, the change of contact area over the initial contact area for different surface separations, g_o/Δ, is shown in Fig. 4.15. Empirical Eq. (4.1) is fit to the FEM data, and these curve-fits are also shown in Fig. 4.15.

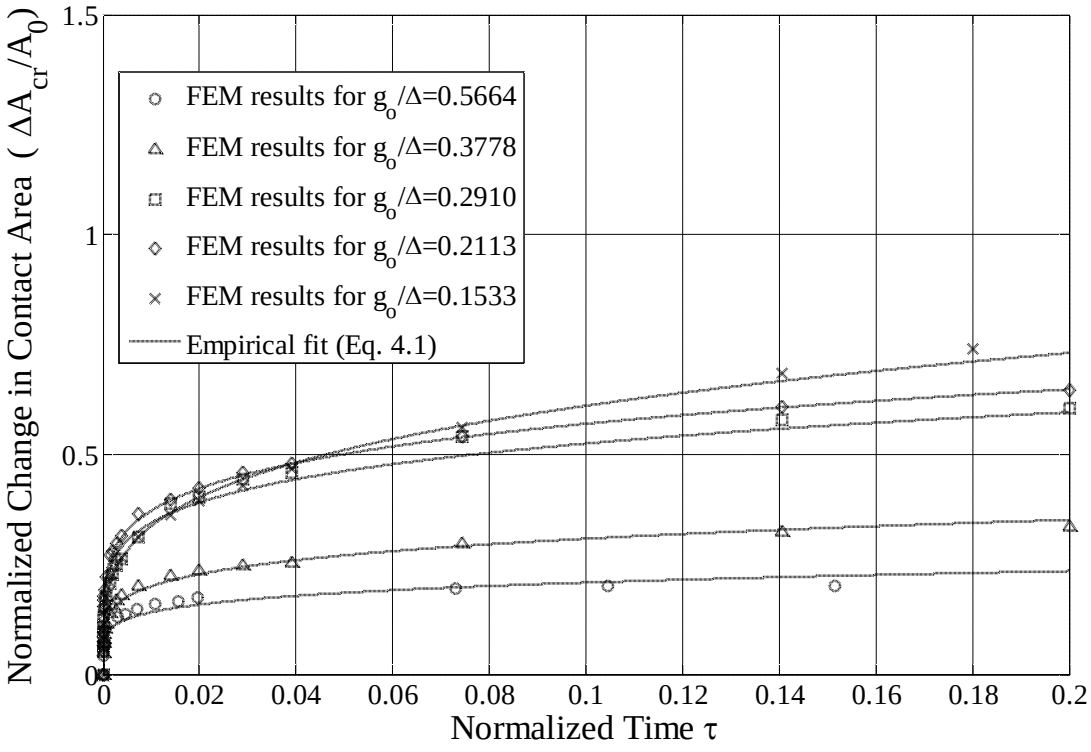

Fig. 4.15 The FEM results and corresponding curve-fits for the normalized contact area change for different surface separations, g_o/Δ

The average error between the FEM data and the curve-fits is 5.88 %. The empirical formulas for constants a and b are given as

$$a|_{\Delta/\lambda=0.02,C_2S_y=10} = 4.001\left(g_0/\Delta\right)^{-0.1332} - 4.026 \tag{4.2}$$

$$b|_{\Delta/\lambda=0.02,C_2S_y=10} = 2\times 10^{-6}\left(g_0/\Delta\right)^{-5.692} + 0.1727 \tag{4.3}$$

For a Garofalo constant of $C_2 = 10/S_y$ and a surface separation of $g_0/\Delta \approx 0.21$, the change of contact area over the initial contact area for different aspect ratio, Δ/λ, values is shown in Fig. 4.16 along with the fit Eq. (4.1).

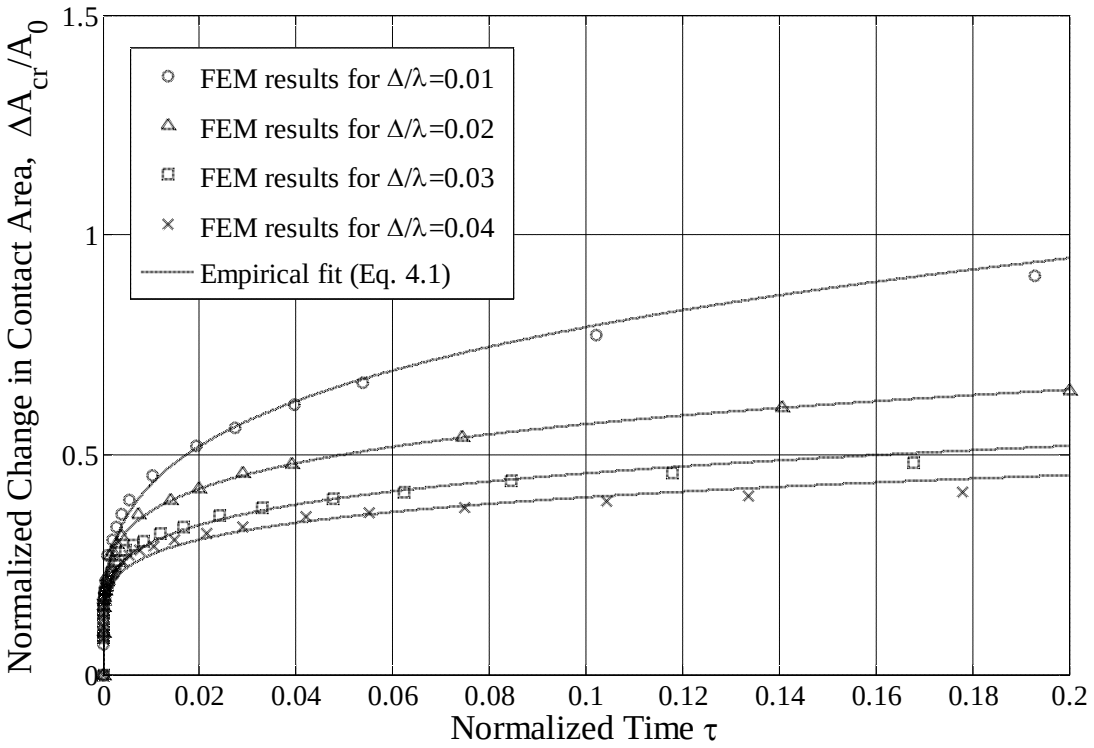

Fig. 4.16 The FEM results and corresponding curve-fits for the normalized contact area change for different aspect ratios, Δ/λ

The average error between the FEM data and the curve-fits is 3.7 %. The empirical formulas for constants a and b are given as

$$a|_{C_2S_y=10} = 0.01(\Delta/\lambda)^{-1.023} - 0.5471 + a|_{\Delta/\lambda=0.02,C_2S_y=10} \tag{4.4}$$

$$b|_{C_2S_y=10} = 3.2\times10^{-6}(\Delta/\lambda)^{-2.237} - 0.0202 + b|_{\Delta/\lambda=0.02,C_2S_y=10} \tag{4.5}$$

In the above equations the parameters $a|_{\Delta/\lambda=0.02,C_2S_y=10}$ and $b|_{\Delta/\lambda=0.02,C_2S_y=10}$ can be calculated from Eqs. (4.2 and 4.3).

Finally, for an aspect ratio of $\Delta/\lambda = 0.02$ and a surface separation of $g_0/\Delta = 0.2113$, the change of contact area over the initial contact area for different C_2 values is shown in Fig. 4.17. Empirical Eq. (4.1) is fit to the FEM data, and these curve-fits are also shown in Fig. 4.17.

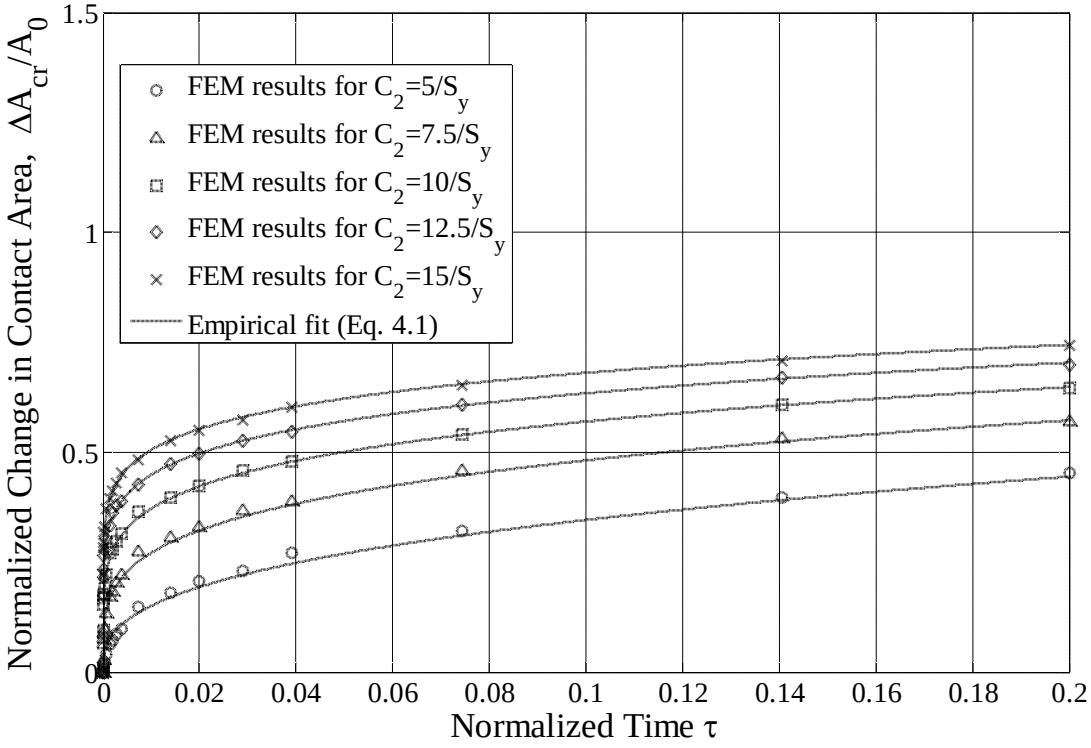

Fig. 4.17 The FEM results and corresponding curve-fits for the normalized contact area change for different, C_2, values

The average error between the FEM data and the curve-fits is 3.2 %. The empirical formulas for constants a and b are given as

$$a = -0.822\left(C_2 S_y\right)^{-0.207} + 0.5103 + a\,|_{C_2 S_y = 10} \tag{4.6}$$

$$b = 1.754\left(C_2 S_y\right)^{-1} - 0.1754 + b\,|_{C_2 S_y = 10} \tag{4.7}$$

In the above equations the parameters $a|_{C_2S_y=10}$ and $b|_{C_2S_y=10}$ can be calculated from Eqs. (4.4 and 4.5).

As mentioned before, the constants in the contact area equation are dependent on the Garofalo constant, C_2, surface separation, g_0/Δ, and aspect ratio, Δ/λ. If contact area at a specific normalized time, τ, for a specific value of Garofalo constant C_2, specific geometry (aspect ratio, Δ/λ), and for a surface separation, g_0/Δ, is desired, Eqs. (4.2-4.7) can be used. First, using the given surface separation, g_0/Δ, Eqs. (4.2 and 4.3) are used to calculate $a|_{\Delta/\lambda=0.02,C_2S_y=10}$ and $b|_{\Delta/\lambda=0.02,C_2S_y=10}$. Then these constants and the given aspect ratio, Δ/λ, will be substituted into Eqs. (4.4 and 4.5) to calculate $a|_{C_2S_y=10}$ and $b|_{C_2S_y=10}$. Finally, these new constants with the given Garofalo constant, C_2, are substituted into Eqs. (4.6 and 4.7) to calculate the final a and b constants. Putting these final constants in Eq. (4.1), the contact area at any time, τ, can be calculated. Note that great care should be taken in using these equations outside of the ranges considered in this work.

4.3.2 Empirical Fit for Contact Pressure

According to the trend of contact pressure results, a two term power law is used to fit the contact pressure results. This function is given in Eq. (4.8) and has four empirical constants a', b', c', and d'.

$$\frac{\Delta\bar{p}_{cr}}{\bar{p}_0}=\frac{\bar{p}_0-\bar{p}_\tau}{\bar{p}_0}=a'\tau^{b'}+c'\tau^{d'} \tag{4.8}$$

For a Garofalo constant of $C_2 = 10/S_y$ and a surface separation of $g_o/\Delta \approx 0.21$, the change of contact pressure over its initial value $\frac{\Delta\bar{p}}{\bar{p}_0} = \frac{\bar{p}_0 - \bar{p}_\tau}{\bar{p}_0}$ for different aspect ratios, Δ/λ, is shown in Fig. 4.18. Empirical Eq. (4.8) is used to fit to the FEM data, and these curve-fits are also shown in Fig. 4.18.

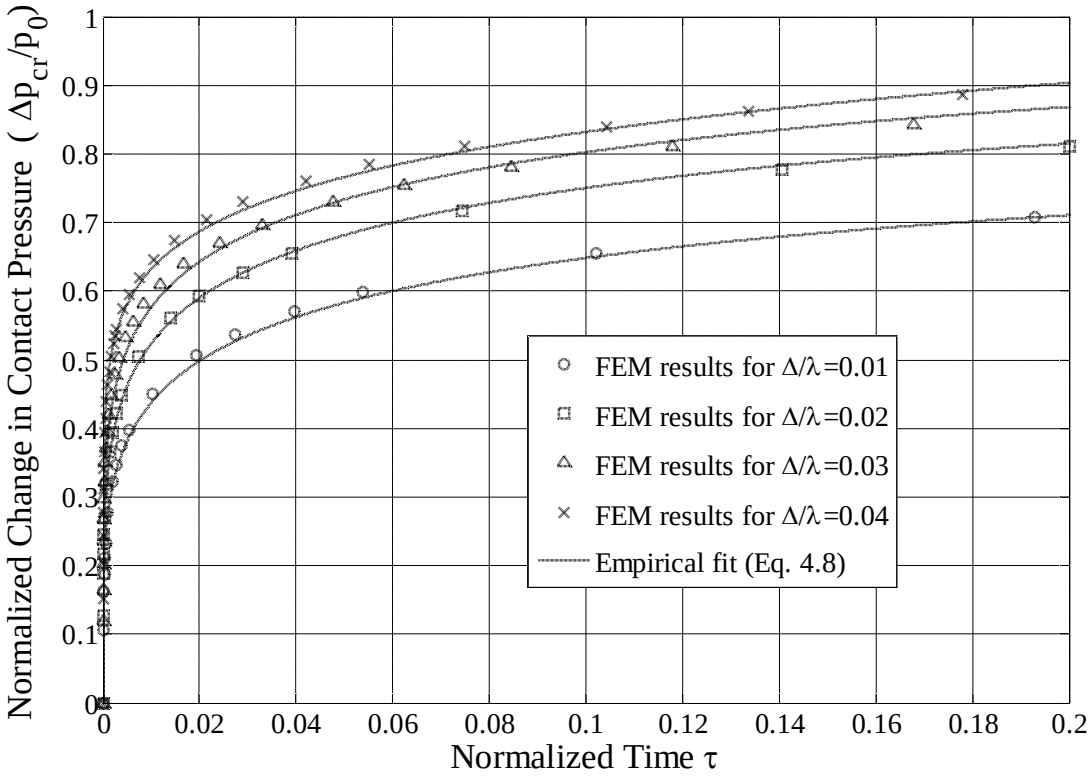

Fig. 4.18 The FEM results and corresponding curve-fits for the normalized contact pressure change for different aspect ratios, Δ/λ

The average error between the FEM data and the curve-fits is 0.48%. The empirical formulas for constants a', b', c', and d' are given as

$$a'|_{g_0/\Delta=0.21,C_2S_y=10} = 980(\Delta/\lambda)^{1.18} - 23.14 \tag{4.9}$$

$$b'|_{g_0/\Delta=0.21,C_2S_y=10} = -5.6\times10^{11}(\Delta/\lambda)^{8.712} + 0.3166 \tag{4.10}$$

$$c'|_{g_0/\Delta=0.21,C_2S_y=10} = -1031(\Delta/\lambda)^{1.201} + 23.75 \tag{4.11}$$

$$d'|_{g_0/\Delta=0.21,C_2S_y=10} = -5.7\times10^{8}(\Delta/\lambda)^{6.64} + 0.3027 \tag{4.12}$$

For an aspect ratio of $\Delta/\lambda = 0.02$ and a Garofalo constant of $C_2 = 10/S_y$, the normalized change of contact pressure for different surface separations, g_o/Δ, values is shown in Fig. 4.19. Empirical Eq. (4.8) is fit to the FEM data, and these curve-fits are also shown in Fig. 4.19.

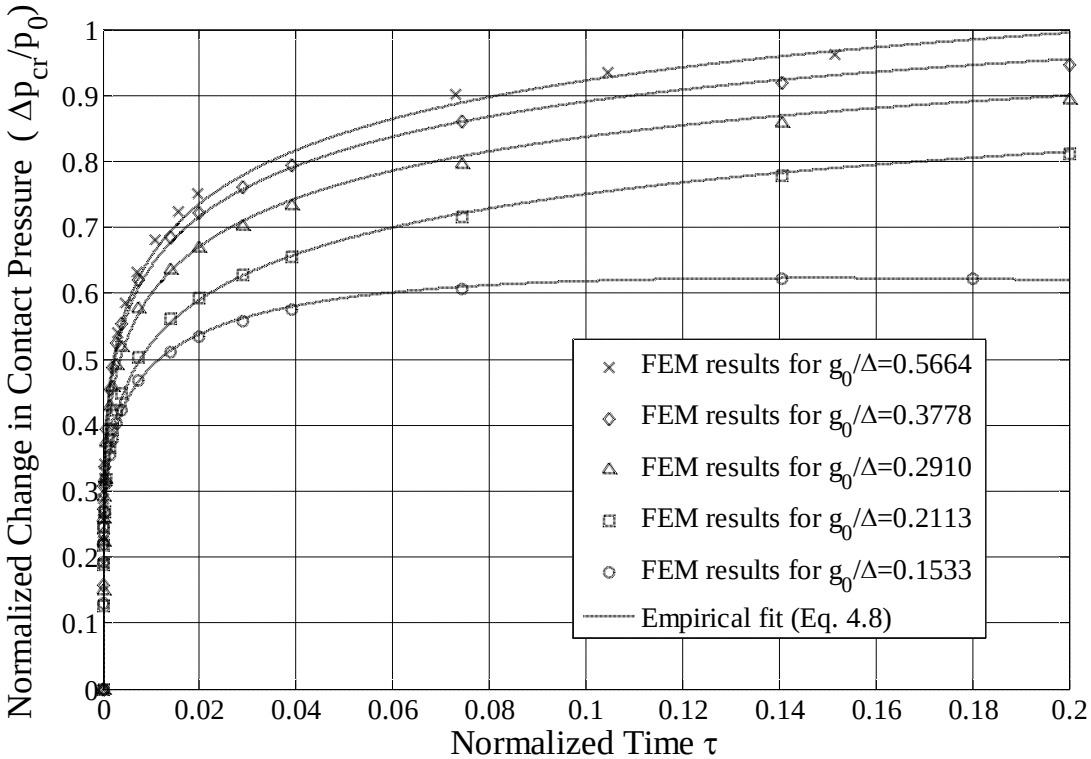

Fig. 4.19 The FEM results and corresponding curve-fits for the normalized contact pressure change for different surface separations, g_0/Δ

The average error between the FEM data and the curve-fits is 0.51%.

The empirical formulas for constants a', b', c', and d' are given as

$$a'|_{C_2S_y=10} = -54.45\left(g_0/\Delta\right)^{0.4} + 29.239 + a'|_{g_0/\Delta=0.21,C_2S_y=10} \tag{4.13}$$

$$b'|_{C_2S_y=10} = 5\times10^{-6}\left(g_0/\Delta\right)^{-4.7} - 0.008 + b'|_{g_0/\Delta=0.21,C_2S_y=10} \tag{4.14}$$

$$c'|_{C_2S_y=10} = 64.61\left(g_0/\Delta\right)^{0.315} - 39.595 + c'|_{g_0/\Delta=0.21,C_2S_y=10} \tag{4.15}$$

$$d'|_{C_2S_y=10} = 3\times10^{-6}\left(g_0/\Delta\right)^{-4.5} - 0.003 + d'|_{g_0/\Delta=0.21,C_2S_y=10} \tag{4.16}$$

In the above equations the parameters $a'|_{g_0/\Delta=0.21,\,C_2S_y=10}$, $b'|_{g_0/\Delta=0.21,C_2S_y=10}$, $c'|_{g_0/\Delta=0.21,\,C_2S_y=10}$, and $d'|_{g_0/\Delta=0.21,C_2S_y=10}$ can be calculated from Eqs. (4.9-4.12).

Finally, For an aspect ratio of $\Delta/\lambda=0.02$, and surface separation of $g_0/\Delta=0.2113$, the normalized change of contact pressure for different C_2 values is shown in Fig. 4.20. Empirical Eq. (4.8) is fit to the FEM data, and these curve-fits are also shown in Fig. 4.20.

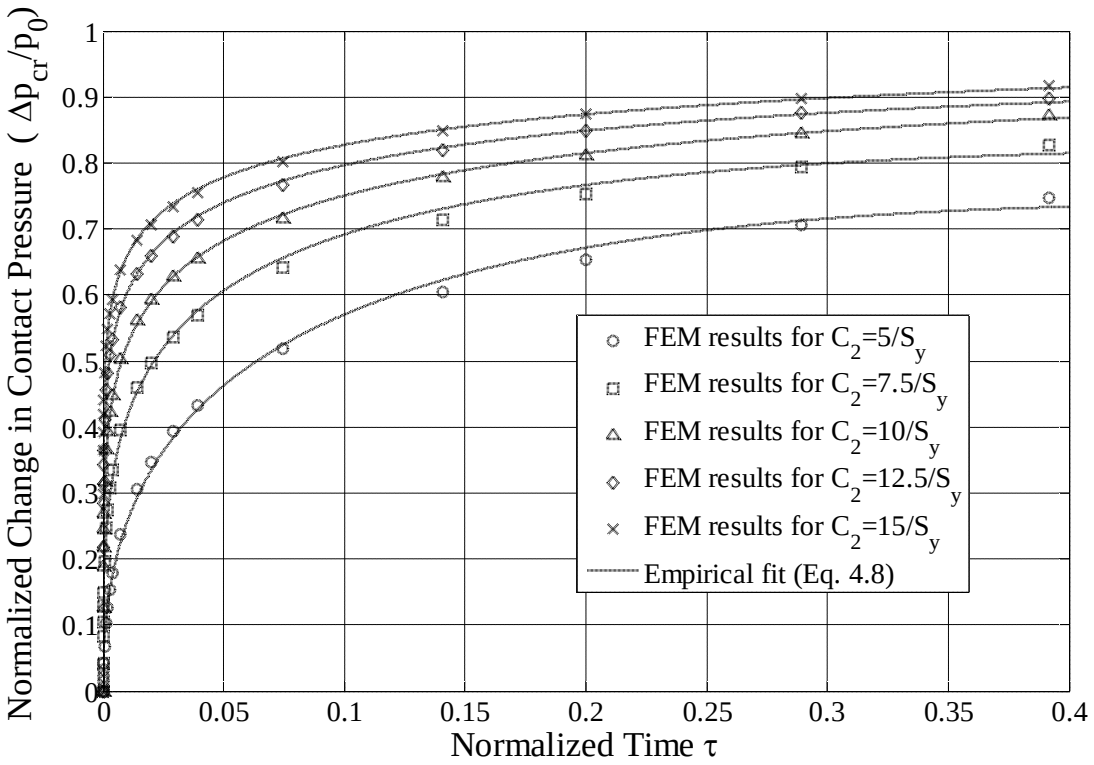

Fig. 4.20 The FEM results and corresponding curve-fits for the normalized contact pressure change for different, C_2, values

The average error between the FEM data and the curve-fits is 0.51%.

The empirical formulas for constants a', b', c', and d' are given as below

$$a' = -132.9\left(C_2 S_y\right)^{-0.25} + 74.735 + a'|_{C_2 S_y=10} \tag{4.17}$$

$$b' = 2.289\left(C_2 S_y\right)^{-0.776} - 0.383 + b'|_{C_2 S_y=10} \tag{4.18}$$

$$c' = 134.9\left(C_2 S_y\right)^{-0.236} - 78.345 + c'|_{C_2 S_y=10} \tag{4.19}$$

$$d' = 2.16\left(C_2 S_y\right)^{-0.688} - 0.443 + d'|_{C_2 S_y = 10} \tag{4.20}$$

In the above equations the parameters $a'|_{C_2 S_y=10}$, $b'|_{C_2 S_y=10}$, $c'|_{C_2 S_y=10}$, and $d'|_{C_2 S_y=10}$ can be calculated from Eqs. (4.13-4.16).

As mentioned before, the constants in contact pressure equation are dependent on the Garofalo constant, C_2, surface separation, g_0/Δ, and aspect ratio, Δ/λ. If contact pressure at a specific normalized time, τ, for a specific value of Garofalo constant C_2, specific geometry (aspect ratio, Δ/λ), and for a surface separation, g_0/Δ, is desired, Eqs. (4.9-4.20) can be used. First, using the given aspect ratio, Δ/λ, Eqs. (4.9-4.12) are used to calculate $a'|_{g_0/\Delta=0.21, C_2 S_y=10}$, $b'|_{g_0/\Delta=0.21, C_2 S_y=10}$, $c'|_{g_0/\Delta=0.21, C_2 S_y=10}$, and $d'|_{g_0/\Delta=0.21, C_2 S_y=10}$. Then these constants and the given surface separation, g_0/Δ, will be substituted into Eqs. (4.13-4.16) to calculate $a'|_{C_2 S_y=10}$, $b'|_{C_2 S_y=10}$, $c'|_{C_2 S_y=10}$, and $d'|_{C_2 S_y=10}$. Finally, these new constants and the given Garofalo constant, C_2, are substituted into Eqs. (4.9-4.12) to calculate the final a', b', c', and d' constants. By putting these final constants into Eq. (4.8), the contact pressure at any time, τ, can be calculated. Note that great care should be taken in using these equations outside of the ranges considered in this work.

In the next section a brief discussion is given about the dependency of the contact area and contact pressure results on the base height of the asperity.

4.4 Base Height-dependency of the Stress Relaxation Results

Two cases are modeled in ANSYS in order to investigate the effect of the base height on the contact area and contact pressure results. The same properties given in Table 4.1 are used here except for the initial surface separation which is set to $g_0/\Delta \approx 0.15$. For the first case (a), a height equal to 20 times the amplitude is selected, and for the second case (b), this height is doubled. The finite element mesh of these two cases are shown in Fig. 4.21.

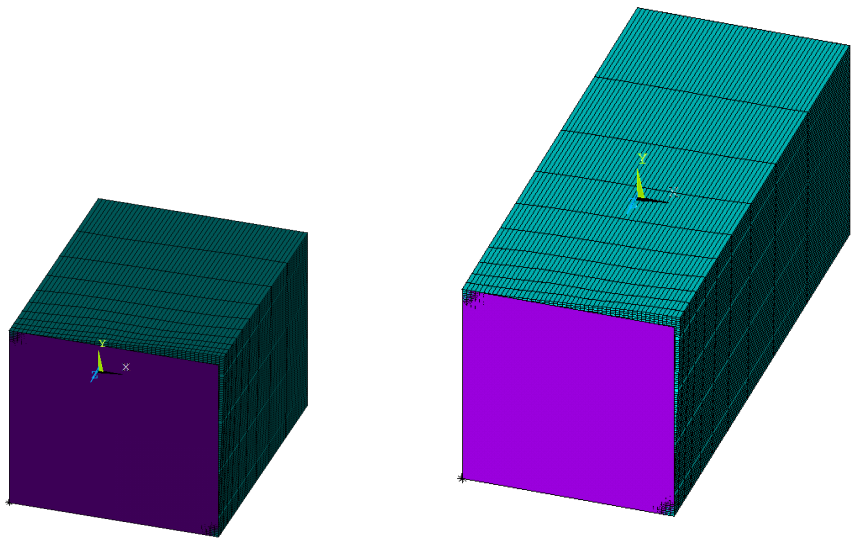

Fig. 4.21 The element plot of the sinusoidal asperity for a case with the (a) smaller height, and the case with the (b) doubled height

The von Mises stress distribution at time $\tau = 0$ before the stress relaxation process happens are shown in Fig. 4.22 for both cases. It can be seen that the von Mises stress for the two cases are similar with a small difference due to the deformation of the substrate. It can be seen from Fig. 4.22 that the maximum von Mises stress in case (a) is $1.326\ GPa$, and for case (b) is $1.332\ GPa$. In case

(b), in order to have the same initial surface separation, $g_0/\Delta \approx 0.15$, higher value for the displacement of the rigid flat surface is inserted, and that's why the initial von Mises stress is higher for this case.

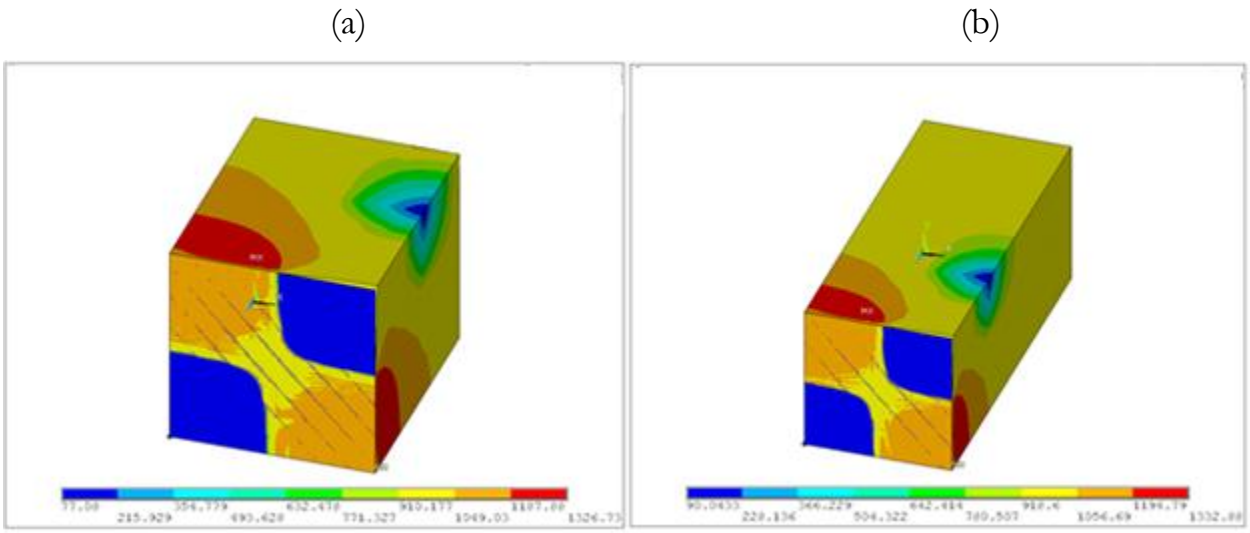

Fig. 4.22 The von Mises stress plot (in MPa) for case with the (a) smaller height, and the case with the (b) doubled height

The stress relaxation results for contact area and contact pressure for cases (a and b) are shown in Figs. 4.23 and 4.24. It can be seen that the contact area and contact pressure results start to show different trends after some threshold of normalized time. Therefore, it shows that the contact area and contact pressure results are dependent on the height of the asperity.

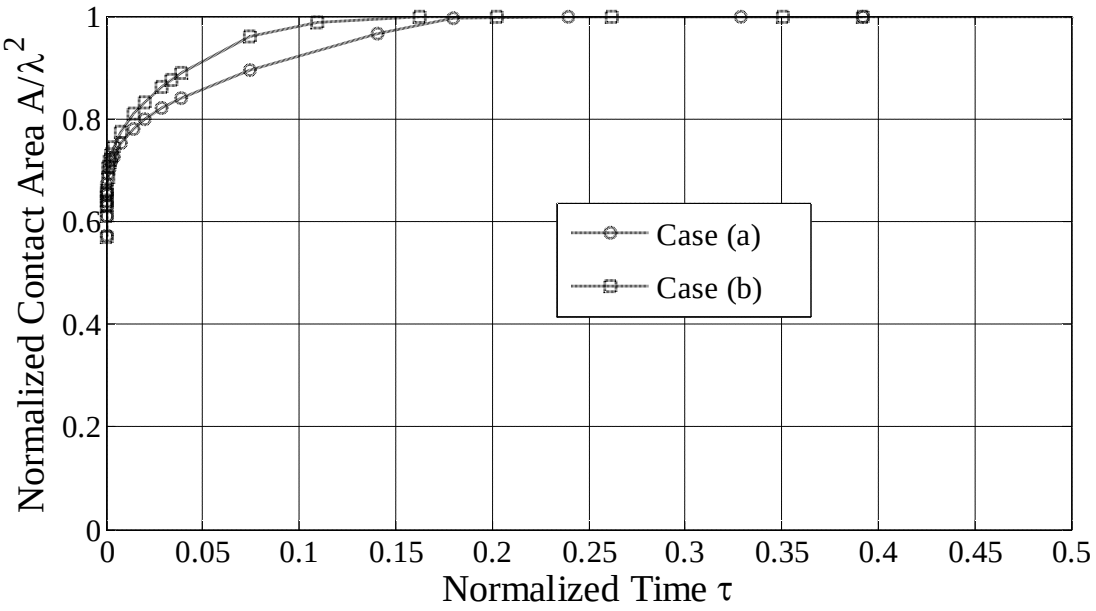

Fig. 4.23 Contact area results for the case with the (a) smaller height, and the case with the (b) doubled height

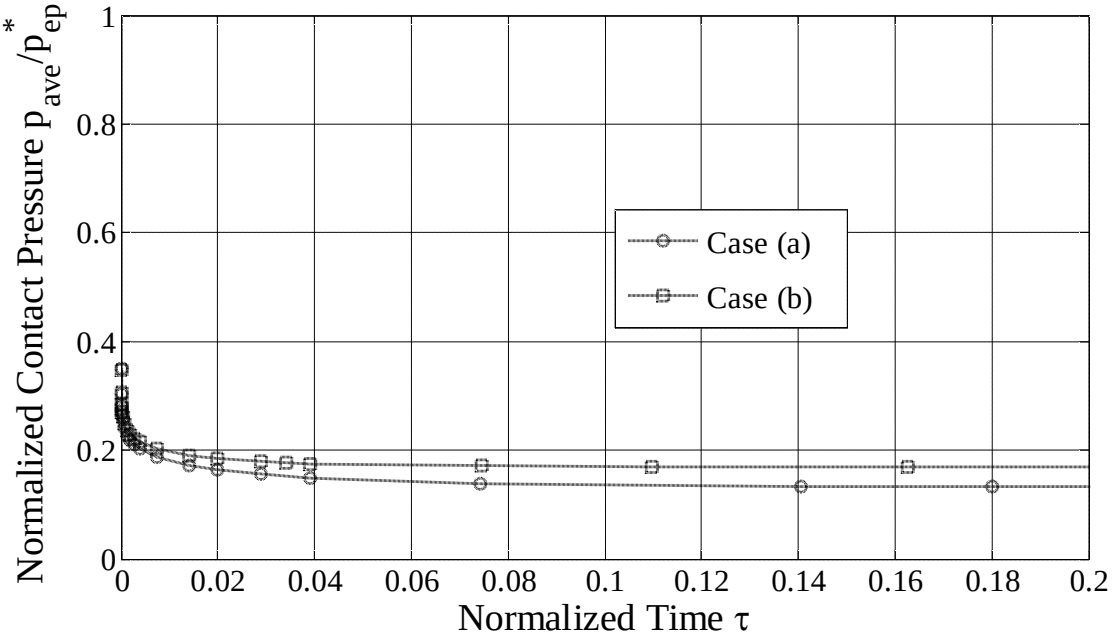

Fig. 4.24 Contact pressure results for case with the (a) smaller height, and the case with the (b) doubled height

To better correlate these results, the rate of aspect ratio, $\delta\Delta/(\lambda\cdot\delta t)$, versus normalized contact pressure, $\bar{p}(\tau)/\,p^{*}_{ep}(\tau)$, is calculated using the contact area and contact pressure results and is shown in Fig. 4.25. This is based on the idea that the rate of creep strain is proportional to the pressure which corresponds to the Garofalo creep law. As an approximation, the change in the asperity amplitude should be proportional to the creep strain rate. This rate represents the permanent change in the shape of the sinusoidal asperity due to creep strain. From Fig. 4.25, It can be seen that these two cases show similar trends which is very interesting, and it declares that the aspect ratio rate, $\delta\Delta/(\lambda\cdot\delta t)$, which is an important parameter in a multiscale model for creep (stress relaxation), is independent from the asperity height.

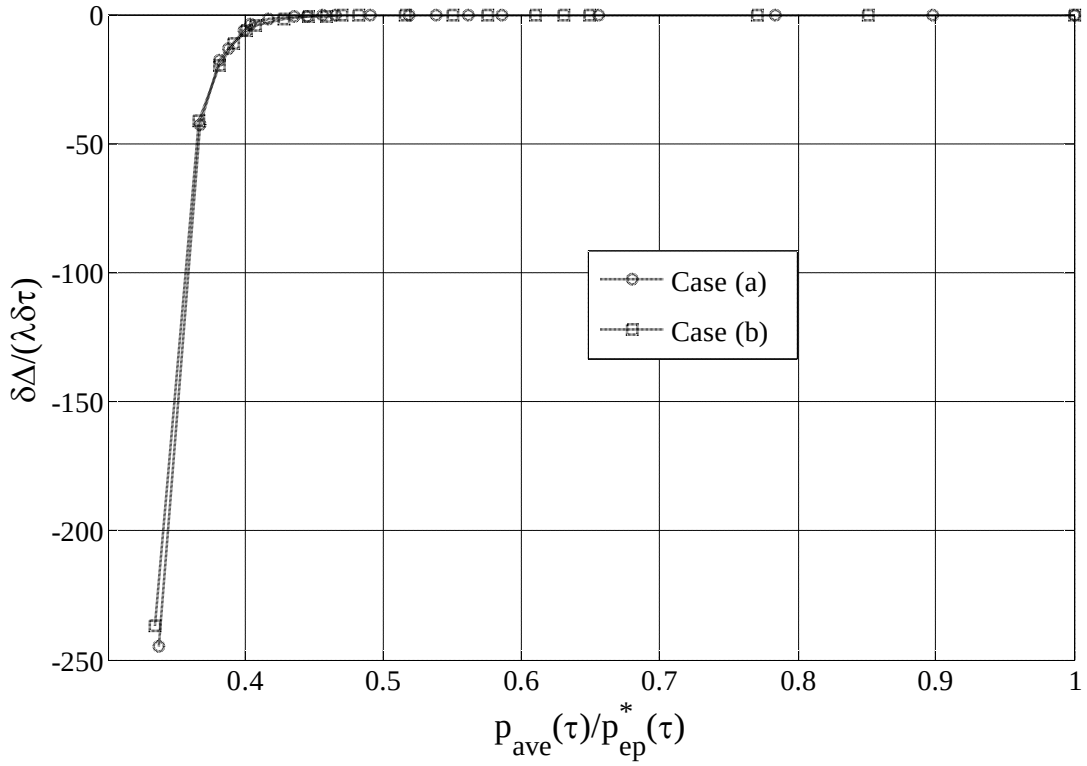

Fig. 4.25 The aspect ratio rate results for the case with the (a) smaller height, and the case with the (b) doubled height

The previously presented contact area and contact pressure results for various Garofalo constant values, C_2, surface separations, g_0/Δ, and aspect ratios, Δ/λ, are used to obtain results for the normalized amplitude rate, $\delta\Delta/(\Delta_0 \cdot \delta t)$, which are shown in Figs. (4.26-4.28), respectively.

The results for the rate of aspect ratio are obtained by three steps:

1. The contact area and contact pressure in each time step is substituted into Eq. 2.11 to calculate the complete contact pressure, p^*_{ep}, as a function of time.
2. The aspect ratio in each time step can be calculated, using the p^*_{ep} results, from Eq. 2.9.
3. The rate of the aspect ratio can be easily calculated using the aspect ratio results along with the finite difference method.

In Figs. (4.26-4.28) the aspect ratio rate is normalized by $1000 \cdot \Delta_0$, where Δ_0 is the initial aspect ratio.

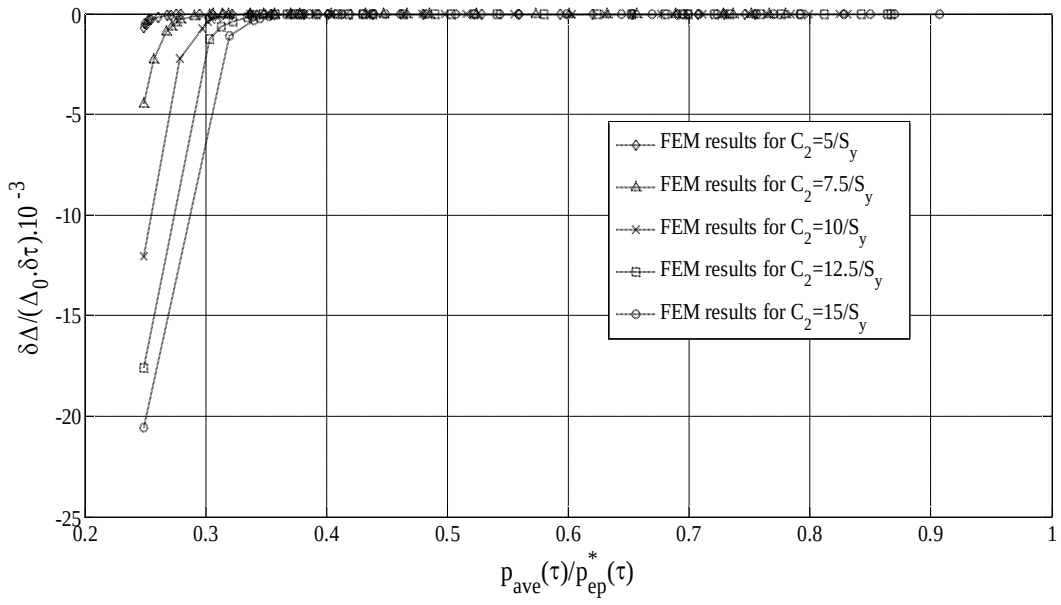

Fig. 4.26 The normalized amplitude rate results for the different values of Garofalo constant, C_2

In Fig. 4.26, it can be seen that as the Garofalo constant C_2 increases, the absolute value of the amplitude rate, $\delta\Delta/(\lambda\cdot\delta t)$, is higher. It means that higher values of the Garofalo constant, C_2, cause larger changes in the amplitude of the asperity which agrees with the definition of C_2. Also, for all the cases, the absolute value of the amplitude rate decreases with time.

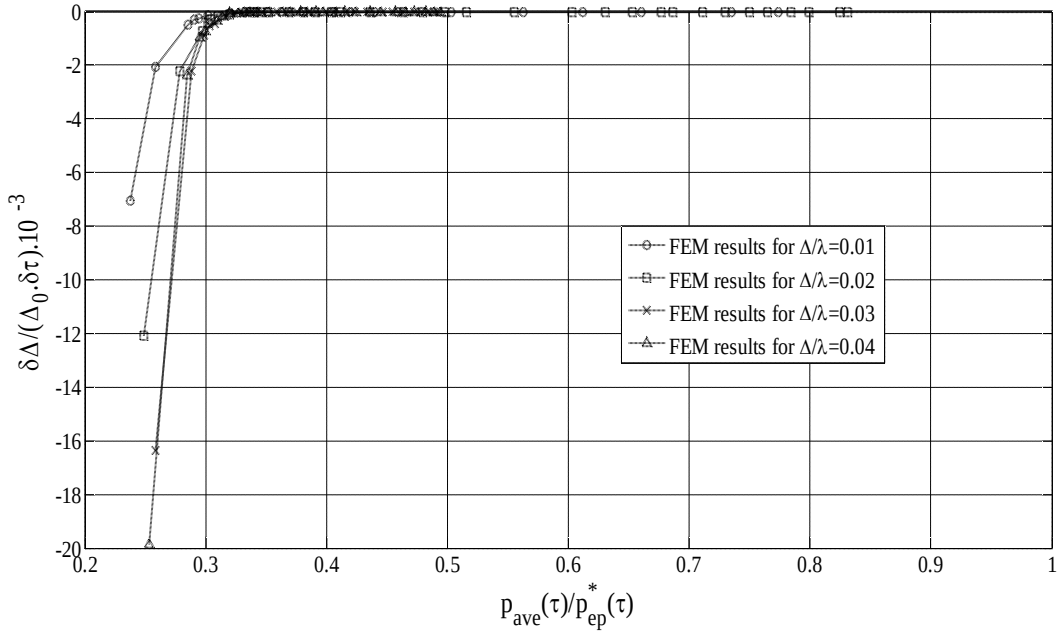

Fig. 4.27 The normalized amplitude rate results for the different values of aspect ratio, Δ/λ

The results for the normalized amplitude rate for different aspect ratios are shown in Fig. 4.27. The results in Fig. 4.27 show that for higher values of aspect ratio, Δ/λ, the absolute values of the amplitude rate are higher.

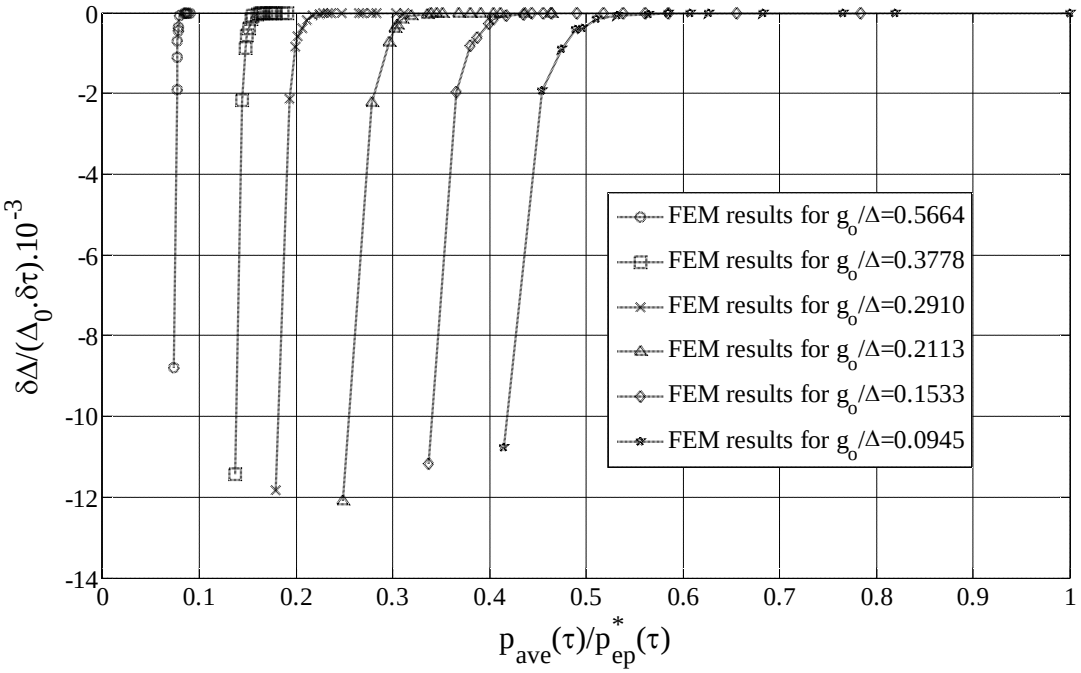

Fig. 4.28 The normalized amplitude rate results for the different values of surface separation, g_o/Δ

The amplitude rate results for different values of the surface separation, g_o/Δ, are given in Fig. 4.28. It can be seen that for different surface separations, the range of normalized contact pressure isn't the same. As the surface separation, g_o/Δ, decreases, the initial contact pressure is higher, and the absolute value of the initial amplitude rate, $\delta\Delta/(\lambda\cdot\delta t)$, should be higher. However, it can be seen that for surface separations lower than $g_o/\Delta \approx 0.21$ ($\delta/\Delta = 1$), the initial amplitude rate decreases instead of increasing.

4.5 Creep Results

In the sections 4.3 and 4.4, the time dependent deformation under constant displacement boundary condition (stress relaxation) was considered, and empirical equations for the contact area and contact pressure as a function of time were developed.

Transient behavior of the sinusoidal asperity under the constant force boundary condition (creep) is investigated in this section as it is shown schematically in Fig. 4.29. In this case the sinusoidal asperity is pressurized in the first load step by applying a force on the rigid flat surface. It should be noted that the (average) contact pressure is constant in this case during the transient process, and only the contact area is changing over time. The same geometry and mesh as the case with constant displacement boundary condition are used here, but instead of displacement, the constant force is applied on the rigid flat surface.

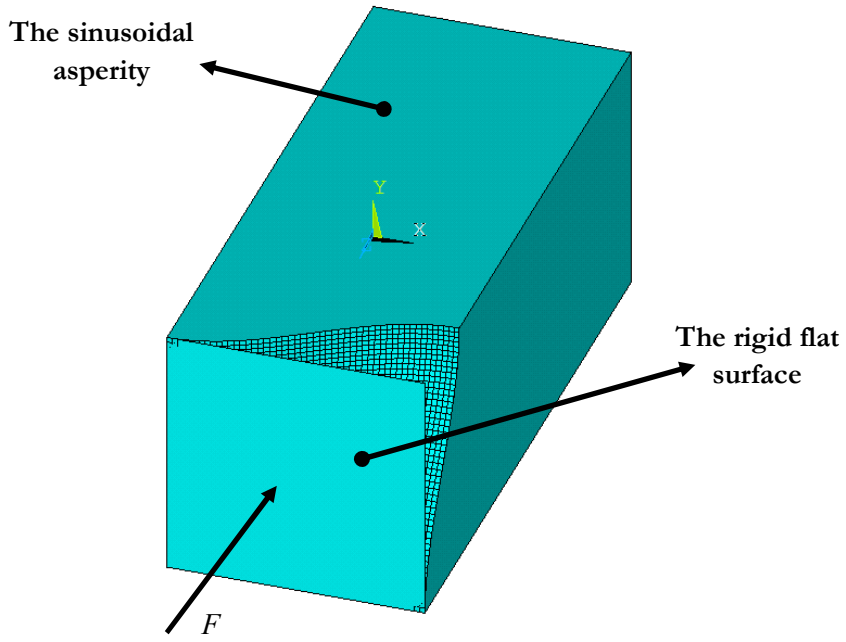

Fig. 4.29 Plot of the three-dimensional sinusoidal asperity under constant force boundary condition

The results for the normalized contact area versus normalized creep time for a reference normal load, $\bar{p} = 0.8\ GPa$, are shown in Fig. 4.30. Here, the applied force is normalized by the apparent contact area, λ^2, resulting in the average pressure $\bar{p}$. The same material and geometrical properties and Garofalo constants used in Table 4.1 are employed. As expected, the contact area increases with time until the complete contact is reached, after which the contact area plateaus at $A = \lambda^2$. It is clear that for this case the average contact pressure will be constant and equal to $\bar{p} = 0.8\ GPa$, and it doesn't change with time.

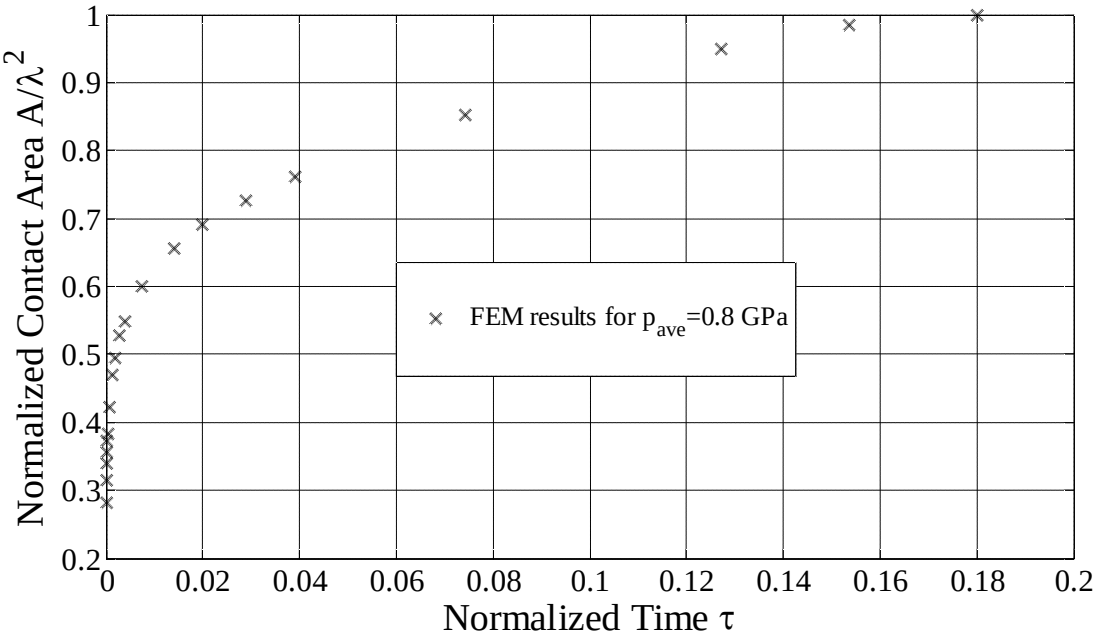

Fig. 4.30 The FEM results for the contact area versus time for reference parameters, and contact pressure, $\bar{p} = 0.8\ GPa$

A parametric study is performed to analyze the effect of different parameters on the creep results. The ranges of parameters considered are given in Table 4.3.

Table 4.3 Overview of parameter ranges used for FE simulations (constant force B.C.)

Parameter	Range
Normal load (average pressure)	$0 \le \bar{p} \le 2 \ \ GPa$
Aspect ratio	$0.01 < \Delta/\lambda < 0.02$
Garofalo constant C_2	$5/S_y < C_2 < 15/S_y$

In Fig. 4.31, the normalized contact area results for different constant normal loads, which are changed within the range given in Table 4.3 are shown.

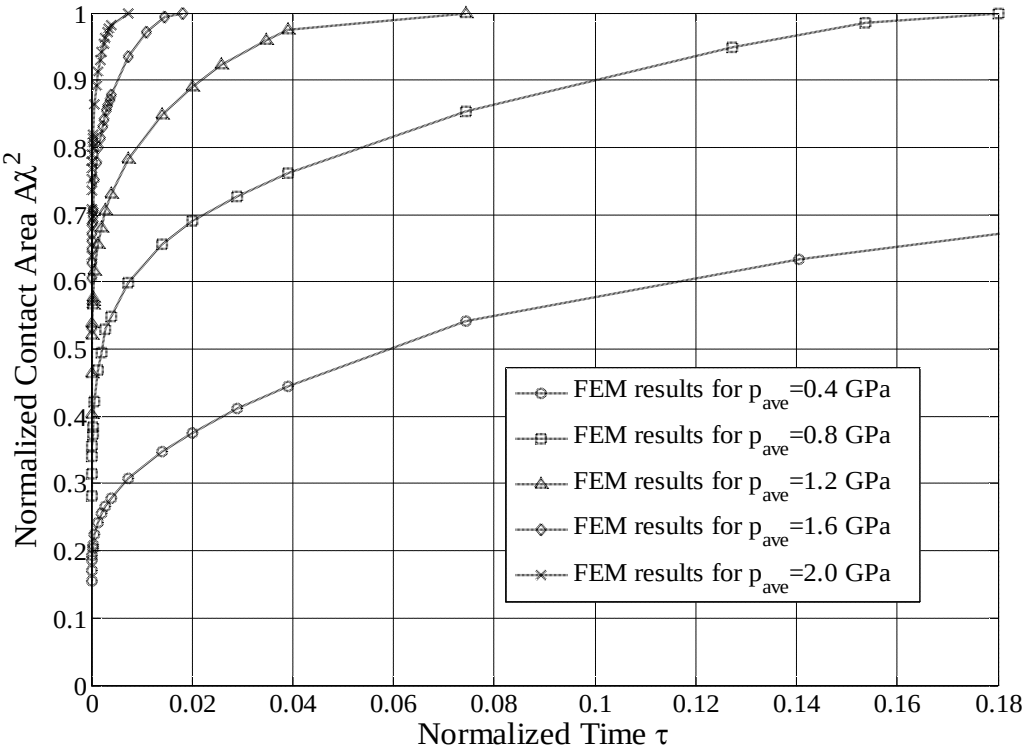

Fig. 4.31 The FEM results for the contact area versus time for different constant contact loads

It can be seen from Fig. 4.31 that as the load increases, the initial contact area is higher. Also, the change in contact area due to creep is faster for higher values of the normal load, and the complete contact condition is achieved at earlier times.

For the case with $\bar{p} = 0.8\ GPa$, the contact area results for the different values of the Garofalo constant, C_2, are shown in Fig. 4.32.

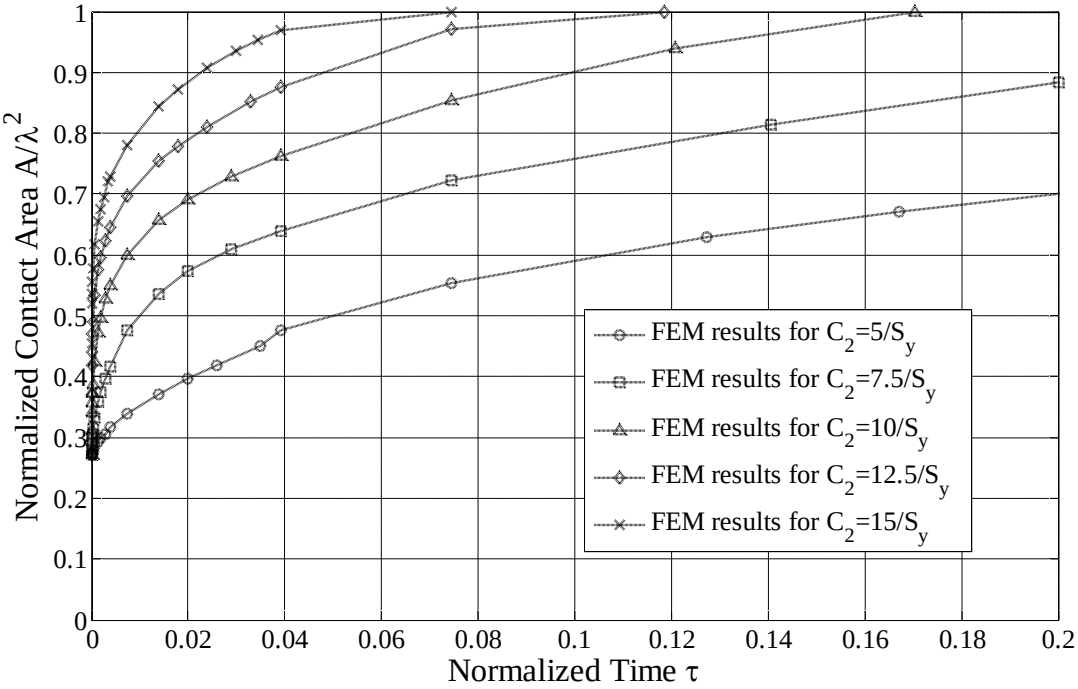

Fig. 4.32 The FEM results for the contact area versus time for different Garofalo constants, C_2

The contact area results show that the rate of change of contact area is much faster for higher values of the Garofalo constant, C_2, and the complete contact condition is reached sooner. It should be noted that all curves for this case start from the same point because the Garofalo constant, C_2, doesn't affect the first load step.

Also, the aspect ratio of the sinusoidal asperity is varied within the range of Table 4.3, and the contact area results are shown in Fig. 4.33. Convergence and element distortion problems made it difficult to solve cases for higher aspect ratios.

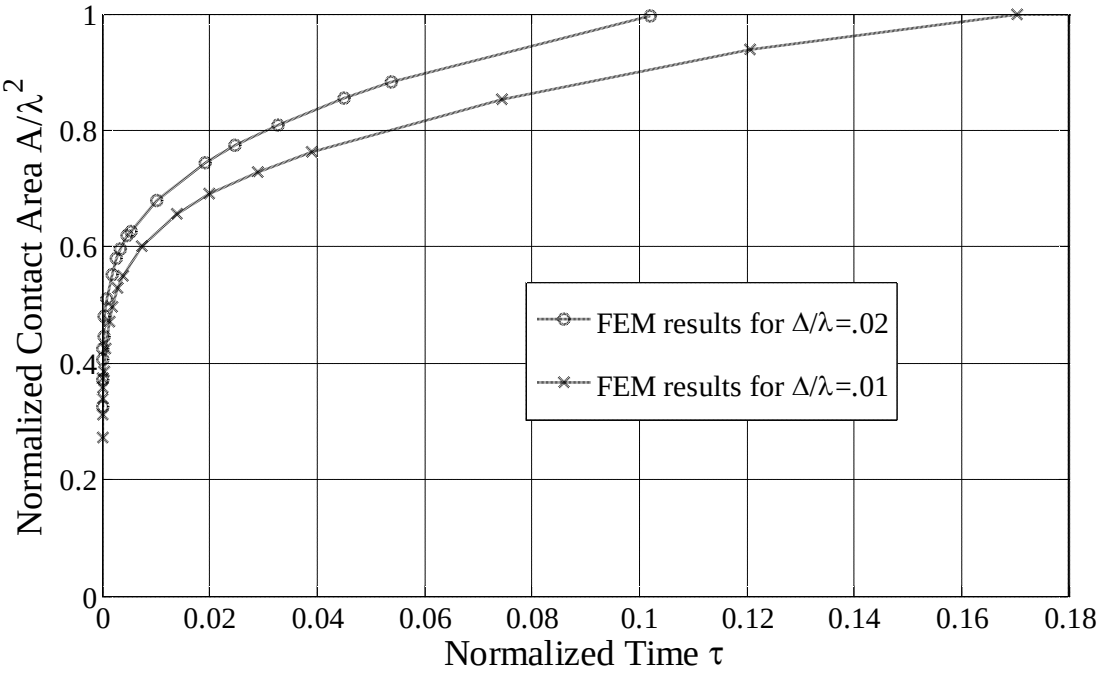

Fig. 4.33 The FEM results for the contact area versus time for different aspect ratios, Δ/λ

4.6 Comparison between the Stress Relaxation and Creep Results

Contact area and contact pressure results for the creep under the constant force, F, and stress relaxation under the displacement, δ, that causes the same value of the contact force before the transient process, are compared to each other. The von Mises stress distribution for both cases (a) and (b) before the transient process is shown in Fig. 4.34. The maximum von Mises stress for both cases is the same and equal to $1.227\ GPa$. The same material and geometrical properties and

creep parameters given in Table 4.1 are used for both cases. It can be seen that the contact area results for these two cases follow different trends (Fig. 4.35). The trend can be explained by the fact that the asperity in case (a) is always under a constant average pressure that causes the complete contact eventually to happen. However, in case (b), the average contact pressure decreases with time and goes asymptotically to zero when the asperity stress completely relaxes. Therefore, the contact area change in case (b) is much smaller than that experienced in case (a). The average contact pressure results are also shown for both cases (Fig. 4.36). It can be seen that the contact pressure in case (a) is constant, but, in case (b) the contact pressure decreases with time.

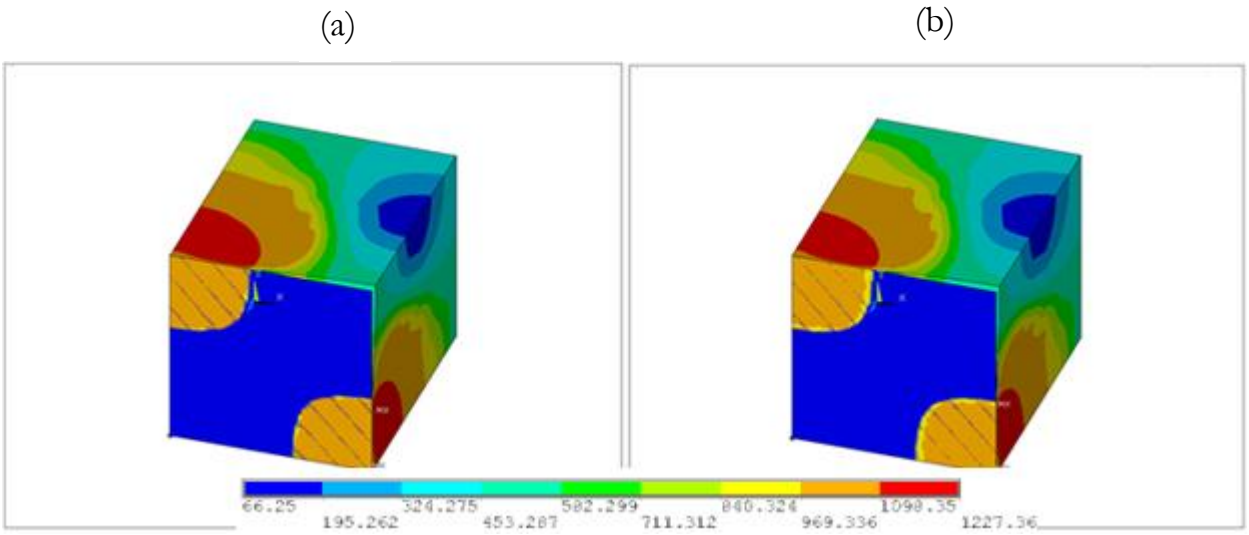

Fig. 4.34 The von Mises stress (MPa) plot for the asperity under (a) constant force, and (b) constant displacement boundary conditions

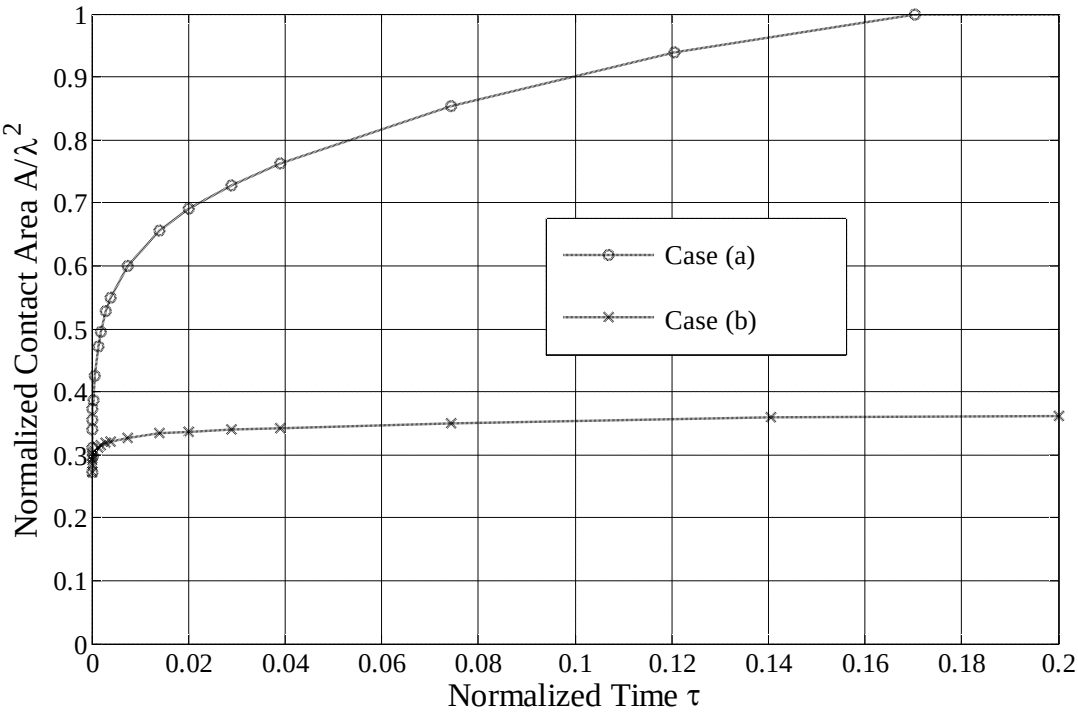

Fig. 4.35 Contact area results for the case under (a) constant force (creep), and the case under (b) constant displacement (stress relaxation) boundary conditions

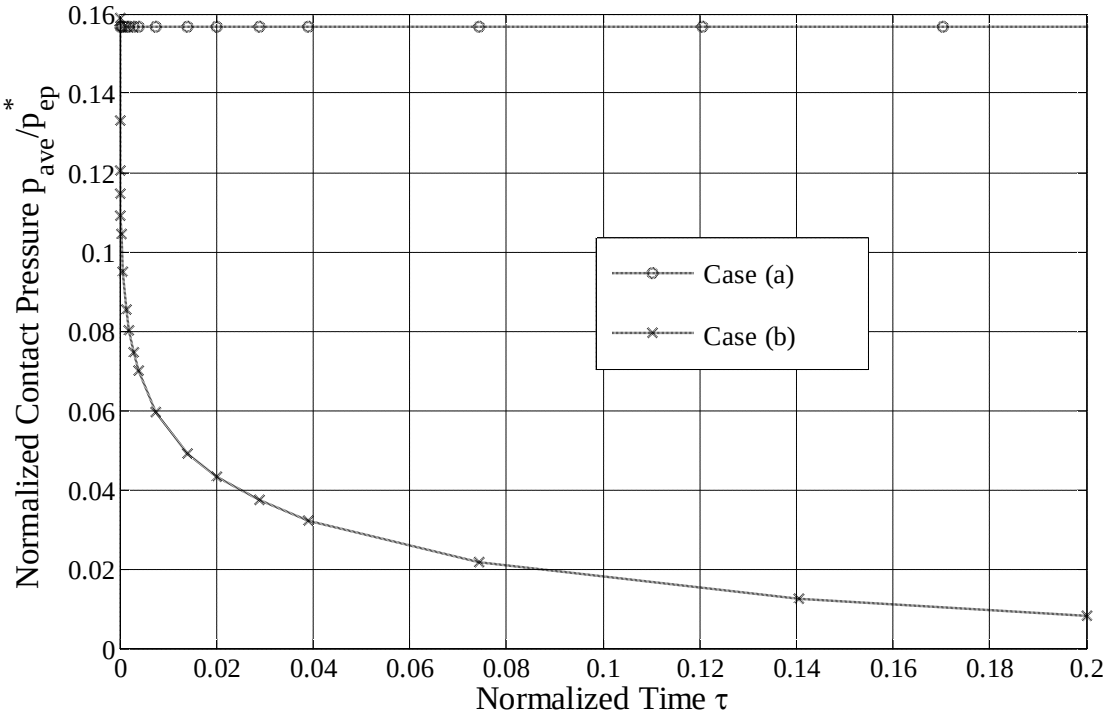

Fig. 4.36 Contact pressure results for the case under (a) constant force (creep), and the case under (b) constant displacement (stress relaxation) boundary conditions

CHAPTER 5

CONCLUSIONS

In this work, the time dependent deformation of a three-dimensional elasto-plastic sinusoidal asperity in contact with a rigid flat surface under both constant displacement (stress relaxation) and constant force (creep) boundary conditions were investigated assuming a hyperbolic sine creep law. A numerical model was generated using the commercial finite element software ANSYS 13.0. The numerical model was verified by comparing the elastic and elasto-plastic results to previous works in the literature. The input constants of Garofalo creep formula were selected for an iron-like material. The contact area and contact pressure results for a reference set of properties were obtained. The trend of the stress relaxation results were reasonable as contact area increased with time, and contact pressure decreased over time. In the case of creep, contact pressure was constant over time. A parametric study was performed to study the effect of different material and geometrical properties, and creep constants on the contact area and contact pressure results. It should be noted that the material and geometrical properties affect both the initial static deformation stage and the transient step, but the creep parameters (Garofalo constants) only affect the second load step or the transient step. It was seen that the creep parameter, C_1, doesn't affect the normalized results, but since it is used in normalizing the time, it causes the range of results to compress or expand over different periods of the normalized time. The results showed that the stress relaxation consists of two phases. The first phase consisted of a fast increase and decrease in contact area and contact pressure, respectively. In the second phase, the stress relaxation process slowed considerably.

Dimensionless expressions were empirically derived for the change of contact area and contact pressure. A power law equation was used for the change of contact area over its initial value, and for the contact pressure a two term power law was used. In developing these empirical equations, the reference material properties were used. Therefore, the empirical equations are only dependent on the aspect ratio, Δ/λ, Garofalo constant, C_2, and surface separation, g_0/Δ. The

errors in the numerical fits are fairly low (less than 4% for the contact area fits and less than 1% for the contact pressure fits) which suggest that the fits are reasonable. Transient results for the case solved with the constant force boundary condition (creep) are also obtained. A brief parametric study was also performed for this boundary condition. Unfortunately, for the case with the constant force boundary condition (creep), it is difficult to obtain results for high loads, and also for high values of aspect ratio due to convergence issues. Also, a case has been considered to compare the transient results for the constant force (creep) and constant displacement (stress relaxation) boundary conditions. The results showed that the contact area and contact pressure change with time for these two cases follow different trends. The aspect ratio rate, $\delta\Delta/(\lambda\delta\tau)$, was obtained from the contact area and contact pressure results for the stress relaxation. It was shown that this quantity is independent from the base height of the sinusoidal asperity. This rate can be used in a multiscale contact model to predict the real contact area between rough surfaces as a function of time.

BIBLIOGRAPHY

[1] Goedecke, A., and Mock, R., 2009, "Creep Relaxation of an Elastic--Perfectly Plastic Hemisphere in Fully Plastic Contact," Journal of Tribology, 131(2), pp. 021407-10.

[2] Johnson, K. L., Greenwood, J. A., and Higginson, J. G., 1985, "The Contact of Elastic Regular Wavy Surfaces," International Journal of Mechanical Sciences, 27(6), pp. 383-396.

[3] Timoshenko, S., and Goodier, J., "Theory of Elasticity. 1951," New York, pp. 412.

[4] Brechet, Y., and Estrin, Y., 1994, "The Effect of Strain Rate Sensitivity on Dynamic Friction of Metals," Scripta Metallurgica et Materialia;(United States), 30(11), pp.

[5] Berthoud, P., Baumberger, T., G'sell, C., and Hiver, J.-M., 1999, "Physical Analysis of the State-and Rate-Dependent Friction Law: Static Friction," Physical Review B, 59(22), pp. 14313.

[6] Baumberger, T., Berthoud, P., and Caroli, C., 1999, "Physical Analysis of the State-and Rate-Dependent Friction Law. Ii. Dynamic Friction," Physical Review B, 60(6), pp. 3928.

[7] Ruina, A., 1983, "Slip Instability and State Variable Friction Laws," Journal of Geophysical Research, 88(B12), pp. 10359-10,370.

[8] Ruina, A., 1983, "Stability of Steady Frictional Slipping," Journal of Applied Mechanics, 50(pp. 343-349.

[9] Rabinowicz, E., 1965, *Friction and Wear of Materials*, Wiley New York,

[10] Persson, B., 2000, "Theory of Time-Dependent Plastic Deformation in Disordered Solids," Physical Review B, 61(9), pp. 5949.

[11] Brot, C., Etsion, I., and Kligerman, Y., 2008, "A Contact Model for a Creeping Sphere and a Rigid Flat," Wear, 265(5), pp. 598-605.

[12] Goedecke, A., Jackson, R. L., and Mock, R., 2010, "Asperity Creep under Constant Force Boundary Conditions," Wear, 268(11), pp. 1285-1294.

[13] Greenwood, J. A., and Williamson, J. B. P., 1966, "Contact of Nominally Flat Surfaces," Proceedings of the Royal Society of London. Series A. Mathematical and Physical Sciences, 295(1442), pp. 300-319.

[14] Archard, J., 1957, "Elastic Deformation and the Laws of Friction," Proceedings of the Royal Society of London. Series A. Mathematical and Physical Sciences, 243(1233), pp. 190-205.

[15] Chang, W. R., Etsion, I., and Bogy, D. B., 1987, "An Elastic-Plastic Model for the Contact of Rough Surfaces," Journal of Tribology, 109(2), pp. 257-263.
[16] Jackson, R. L., and Kogut, L., 2006, "A Comparison of Flattening and Indentation Approaches for Contact Mechanics Modeling of Single Asperity Contacts," Journal of Tribology, 128(1), pp. 209-212.
[17] Polycarpou, A. A., and Etsion, I., 1999, "Analytical Approximations in Modeling Contacting Rough Surfaces," Journal of Tribology, 121(2), pp. 234-239.
[18] Kogut, L., and Etsion, I., 2002, "Elastic-Plastic Contact Analysis of a Sphere and a Rigid Flat," Journal of Applied Mechanics, 69(5), pp. 657-662.
[19] Jackson, R. L., and Green, I., 2005, "A Finite Element Study of Elasto-Plastic Hemispherical Contact against a Rigid Flat," Transactions of the ASME-F-Journal of Tribology, 127(2), pp. 343-354.
[20] Lin, L. P., and Lin, J. F., 2005, "An Elastoplastic Microasperity Contact Model for Metallic Materials," Journal of Tribology, 127(3), pp. 666-672.
[21] Lévesque, F., Goudreau, S., and Cloutier, L., 2011, "Elastic-Plastic Microcontact Model for Elliptical Contact Areas and Its Application to a Treillis Point in Overhead Electrical Conductors," Journal of Tribology, 133(1), pp.
[22] **林黎柏**, and **林仁輝**, 2009, "Effects of Ellipticity of Contact Area and Poisson's Ratio on the Yielding Behavior of Two Contact Solids," pp.
[23] Jamari, J., and Schipper, D., 2006, "An Elastic–Plastic Contact Model of Ellipsoid Bodies," Tribology Letters, 21(3), pp. 262-271.
[24] Westergaard, H. M., 1939, "Bearing Pressures and Cracks," ASME J. Appl. Mech., 6), pp. 49-53.
[25] Ciavarella, M., Demelio, G., Barber, J. R., and Jang, Y. H., 2000, "Linear Elastic Contact of the Weierstrass Profile," Proceedings of the Royal Society of London. Series A: Mathematical, Physical and Engineering Sciences, 456(1994), pp. 387-405.
[26] Gao, Y. F., Bower, A. F., Kim, K. S., Lev, L., and Cheng, Y. T., 2006, "The Behavior of an Elastic–Perfectly Plastic Sinusoidal Surface under Contact Loading," Wear, 261(2), pp. 145-154.

[27] Krithivasan, V., and Jackson, R. L., 2007, "An Analysis of Three-Dimensional Elasto-Plastic Sinusoidal Contact," Tribology Letters, 27(1), pp. 31-43.

[28] Jackson, R. L., Krithivasan, V., and Wilson, W. E., 2008, "The Pressure to Cause Complete Contact between Elastic—Plastic Sinusoidal Surfaces," Proceedings of the Institution of Mechanical Engineers, Part J: Journal of Engineering Tribology, 222(7), pp. 857-863.

[29] Tabor, D., 1951, "The Hardness of Materials," Claredon Press, Oxford, UK, 131(pp. 357-364.

[30] Williamson, J., and Hunt, R., 1972, "Asperity Persistence and the Real Area of Contact between Rough Surfaces," Proceedings of the Royal Society of London. A. Mathematical and Physical Sciences, 327(1569), pp. 147-157.

[31] Childs, T., 1977, "The Persistence of Roughness between Surfaces in Static Contact," Proceedings of the Royal Society of London. A. Mathematical and Physical Sciences, 353(1672), pp. 35-53.

[32] Ciavarella, M., Murolo, G., Demelio, G., and Barber, J. R., 2004, "Elastic Contact Stiffness and Contact Resistance for the Weierstrass Profile," Journal of the Mechanics and Physics of Solids, 52(6), pp. 1247-1265.

[33] Gao, Y. F., and Bower, A., 2006, "Elastic–Plastic Contact of a Rough Surface with Weierstrass Profile," Proceedings of the Royal Society A: Mathematical, Physical and Engineering Science, 462(2065), pp. 319-348.

[34] Jackson, R. L., and Streator, J. L., 2006, "A Multi-Scale Model for Contact between Rough Surfaces," Wear, 261(11), pp. 1337-1347.

[35] Brizmer, V., Kligerman, Y., and Etsion, I., 2007, "A Model for Junction Growth of a Spherical Contact under Full Stick Condition," Journal of Tribology, 129(4), pp. 783-790.

[36] Etsion, I., Kligerman, Y., and Kadin, Y., 2005, "Unloading of an Elastic–Plastic Loaded Spherical Contact," International Journal of Solids and Structures, 42(13), pp. 3716-3729.

[37] Kadin, Y., Kligerman, Y., and Etsion, I., 2008, "Loading–Unloading of an Elastic–Plastic Adhesive Spherical Microcontact," Journal of Colloid and Interface Science, 321(1), pp. 242-250.

[38] Jackson, R., Chusoipin, I., and Green, I., 2005, "A Finite Element Study of the Residual Stress and Deformation in Hemispherical Contacts," Transactions of the ASME-F-Journal of Tribology, 127(3), pp. 484-493.

[39] Mulhearn, T., and Tabor, D., 1960, "Creep and Hardness of Metals: A Physical Study," J. Inst. Met, 89(1), pp. 7-12.

[40] Bower, A., Fleck, N., Needleman, A., and Ogbonna, N., 1993, "Indentation of a Power Law Creeping Solid," Proceedings of the Royal Society of London. Series A: Mathematical and Physical Sciences, 441(1911), pp. 97-124.

[41] Ogbonna, N., Fleck, N., and Cocks, A., 1995, "Transient Creep Analysis of Ball Indentation," International journal of mechanical sciences, 37(11), pp. 1179-1202.

[42] Ossa, E., Deshpande, V., and Cebon, D., 2005, "Spherical Indentation Behaviour of Bitumen," Acta materialia, 53(11), pp. 3103-3113.

[43] Kumar, R., and Narasimhan, R., 2004, "Analysis of Spherical Indentation of Linear Viscoelastic Materials," Current Science, 87(8), pp. 1088-1095.

[44] Malamut, S., Kligerman, Y., and Etsion, I., 2009, "The Effect of Dwell Time on the Static Friction in Creeping Elastic–Plastic Polymer Spherical Contact," Tribology Letters, 35(3), pp. 159-170.

[45] Dieterich, J., 1978, "Time-Dependent Friction and the Mechanics of Stick-Slip," pure and applied geophysics, 116(4-5), pp. 790-806.

[46] Feyzullahoglu, E., and Saffak, Z., 2008, "The Tribological Behaviour of Different Engineering Plastics under Dry Friction Conditions," Materials & Design, 29(1), pp. 205-211.

[47] Li, Y., Trauner, D., and Talke, F., 1990, "Effect of Humidity on Stiction and Friction of the Head/Disk Interface," Magnetics, IEEE Transactions on, 26(5), pp. 2487-2489.

[48] Merkher, Y., Sivan, S., Etsion, I., Maroudas, A., Halperin, G., and Yosef, A., 2006, "A Rational Human Joint Friction Test Using a Human Cartilage-on-Cartilage Arrangement," Tribology Letters, 22(1), pp. 29-36.

[49] Gitis, N. V., and Volpe, L., 1992, "Nature of Static Friction Time Dependence," Journal of Physics D: Applied Physics, 25(4), pp. 605.

[50] Rabinowicz, E., 1958, "The Intrinsic Variables Affecting the Stick-Slip Process," Proceedings of the Physical Society, 71(4), pp. 668.

[51] Gittus, J., 1975, "Creep, Viscoelasticity, and Creep Fracture in Solids," pp.

[52] Tomlins, P. E., 1996, "Comparison of Different Functions for Modelling the Creep and Physical Ageing Effects in Plastics," Polymer, 37(17), pp. 3907-3913.

[53] 2010, "Ansys 13.0 Documentation " ANSYS Inc., pp.

[54] Garofalo, F., 1965, *Fundamentals of Creep and Creep-Rupture in Metals*, Macmillan,

[55] Manners, W., 2008, "Plastic Deformation of a Sinusoidal Surface," Wear, 264(1), pp. 60-68.

[56] Ashby, M. F., and Jones, D. R. H., 2005, "Engineering Materials 1: An Introduction to Properties," Applications and Design, pp.

APPENDICES

APPENDIX A

"APDL" CODE USED FOR MODLING THE EFFECT OF STRESS RELAXATION

```
!---------- FE Model of Elasto-Plastic Sinusoidal Asperity ----------!
!---------- in Contact with the Rigid Flat Surface under Time Dependent ----------!
!---------- Deformation Including Stress Relaxation and Creep ----------!

! LENGTH UNIT: mm
/prep7                  ! PREPROCESSOR
ET, 1, SOLID186         ! SOLID186 (20-NODE BRICK ELEMENT)
ET, 2, TARGE170         ! TYPE 2 = 4-NODE TARGET ELEMENT
ET, 3, CONTA174         ! TYPE 3 = 4-NODE CONTACT ELEMENT
KEYOPT, 2, 2, 1         ! CONSTRAINTS OF NODES ON TARGET SURFACE DEFINED
                         BY USERS
KEYOPT, 3, 5, 1         ! CLOSE INITIAL GAP BETWEEN CONTACT AND TARGET
                         SURFACES
KEYOPT, 3, 10, 2        ! NORMAL CONTACT STIFFNESS IS UPDATED EACH ITERATION
```

```
!------------------------ MATERIAL PROPERTIES --------------------------!
! THE MATERIAL OF THE SINUSOIDAL SURFACE IS ASSUMED ELASTO-PLASTIC, BI-
LINEAR ISOTROPIC HARDENING SOLID
MP, EX, 1, 200E3          ! ELASTIC MODULUS [N/(mm^2)]
MP, NUXY, 1, 0.3          ! POISSON'S RATIO
TB, BISO                  ! BILINEAR ISOTROPIC MATERIAL MODEL
TBDATA, 1, 1e3            ! YIELD STRESS  [N/(mm^2)]
TBDATA, 2, 4e3            ! TANGENT MODULUS [N/(mm^2)]
TB, CREEP, 1, , , 8       ! USING GAROFALO LAW FOR CREEP
TBTEMP, 0                 ! DOESN'T AFFECT THE RESULTS
TBDATA, 1, 1E-3, 1E-2, 1, 0
                          ! CREEP CONSTANTS c81, c82, c83, c84 OF GAROFALO LAW
*SET, N, 56               ! NUMBER OF NODES IN X AND Y DIRECTIONS
*DIM, XX, ARRAY, N  ! ARRAY OF NODES IN X DIRECTION
*DIM, YY, ARRAY, N   ! ARRAY OF NODES IN Y DIRECTION
*SET, DELTA, 0.02       ! AMPLITUDE [mm]
*SET, LAMBDA, 1         ! WAVELENGTH IN X AND Y DIRECTIONS [mm]
*SET, DEPTH, 30*DELTA
                         ! DEPTH OF THE SUBSTRATE [mm]
*SET, DELXY, LAMBDA/(N-1)
                          ! THE MESH INTERVAL IN THE X AND Y DIRECTIONS [mm]
```

```
*SET, PI, 3.1415926D0
*SET, PENE, -0.02        ! PENETRATION OF RIGID FLAT INTO THE SINUSOIDAL
                          SURFACE [mm]
*DO, I, 1, N
*SET, XX(I), LAMBDA/2/(N-1)*(I-1)
                         ! NODAL COORDINATE IN THE X DIRECTION [mm]
*SET,YY(I), LAMBDA/2/(N-1)*(I-1)
                         ! NODAL COORDINATE IN THE Y DIRECTION [mm]
*ENDDO
*DIM, ZZ, ARRAY, N, N
                         ! SINUSOIDAL SURFACE HEIGHT MATRIX
*DO, I, 1, N             ! CALCULATING THE SINUSOIDAL SURFACE HEIGHT AT THE
                          DISCRETE NODES
*DO, J, 1, N
*SET, ZZ(I,J) , DELTA*( 1 - COS(2*PI*XX(I))*COS(2*PI*YY(J)) ) + DEPTH
*ENDDO
*ENDDO
*DO, I, 1, N             ! CREATING THE KEY POINTS ON THE SINUSOIDAL SURFACE
*DO, J, 1, N
K, (I-1)*N + J, XX(I), YY(J), ZZ(I,J)
*ENDDO
```

```
*ENDDO
*DO, J, 1, N              ! CONNECTING THE NEIGHBORING KEY POINTS ALONG Y
                            AXIS TO FORM THE LINE ELEMENTS
*DO, I, 1, N-1
L, (J-1)*N + I, (J-1)*N + I + 1
*ENDDO
*ENDDO

*DO, I, 1, N-1        ! CONNECTING THE NEIGHBORING KEYPOINTS ALONG X AXIS
                          TO FORM THE LINE ELEMENTS
*DO, J, 1, N
L, (I-1)*N + J, (I-1)*N + J + N
*ENDDO
*ENDDO

*DO, I, 1, N-1       ! CREATING AREA ELEMENT THROUGH THE NEIGHBORING LINE
ELEMENTS
*DO, J, 1, N-1
LSEL, S, LOC, X, XX(I) - 1/8*DELXY, XX(I+1) + 1/8*DELXY
LSEL, R, LOC, Y, YY(J) - 1/8*DELXY, YY(J+1) + 1/8*DELXY
AL, ALL
```

```
ALLSEL
*ENDDO
*ENDDO
CM, SINUSOIDAL, AREA
                    ! CREATING THE SINUSOIDAL SURFACE BY COMBINING ALL OF
                     THE SMALL AREAS
BLC4, 0, 0, LAMBDA/2, LAMBDA/2, 2*DEPTH
                   ! CREATING A BLOCK OF THE VOLUME: LAMBDA/2 X LAMBDA/2 X
                    2*DEPTH
VSBA, 1, SINUSOIDAL, SEPO, DELETE
                    ! USE THE SINUSOIDAL SURFACE TO SPLIT THE BLOCK INTO TWO
VDELE, 3, 3, , 1    ! DELETING THE UPPER PART OF THE BLOCK

   !-------------------------GENERATING THE RIGID FLAT SURFACE--------------------------!
WPOFFS, , , DEPTH + 2*DELTA
                  ! ALIGNING THE WORKING COORDINATE SYSTEM WITH THE
                    PEAK OF THE SINUSOIDAL WAVINESS RECTING, 0, LAMBDA/2,
                    0, LAMBDA/2
RECTING, 0, LAMBDA/2, 0, LAMBDA/2
                  ! CREATING THE RECTANGULAR SURFACE OF LAMBDA/2 X
                   LAMBDA/2 BY TWO CORNERS!
```

```
NUMCMP, AREA          ! RESORT THE AREA LABEL
NUMCMP, NODE          ! RESORT THE NODAL LABEL
NUMCMP, ELEM          ! RESORT THE ELEMENT LABEL
NUMCMP, KP            ! RESORT THE KEYPOINT LABEL
NUMCMP, LINE          ! RESORT THE LINE LABEL
NUMCMP, VOLU          ! RESORT THE LINE LABEL

                !------------------------MESHING--------------------------!
! RIGID FLAT
LESIZE, 1,,, 1              ! MESHING TARGET SURFACE WITH ONLY ONE TARGE170
                              ELEMENT
LESIZE, 2,,, 1
LESIZE, 3,,, 1
LESIZE, 4,,, 1
ASEL, S,,, 1
TYPE, 2                 ! SELECT TARGE170
AMESH, ALL              ! MESHING AREA
ESURF, ALL, REVERSE   ! REVERSE NORMAL DIRECTION OF ELEMENT TARGE170
ALLSEL
NSEL, S, , , 1              ! CREATE A PILOT NODE ON THE RIGID FLAT
CM, PILOT, NODE
```

```
ALLSEL                          ! DIVID FOUR VERTICLE LINE ELEMENT INTO 10
                                  SUBELEMENTS
LESIZE, 2*(N-1)*N + 8 + 1 „„ 10, 10
LESIZE, 2*(N-1)*N + 8 + 2 „„ 10, 10
LESIZE, 2*(N-1)*N + 8 + 3 „„ 10, 10
LESIZE, 2*(N-1)*N + 8 + 4 „„ 10, 10
ASEL, ALL                       ! SELECT ALL AREAS
ASEL, U, AREA, , (N-1)*(N-1) + 2    ! UNSELECT BOTTOM SURFACE
ASEL, U, AREA, , (N-1)*(N-1) + 3    ! UNSELECT FOUR LATERAL SURFACES
ASEL, U, AREA, , (N-1)*(N-1) + 4
ASEL, U, AREA, , (N-1)*(N-1) + 5
ASEL, U, AREA, , (N-1)*(N-1) + 6
ASEL, U, AREA, , 1              ! UNSELECT THE RIGID FLAT AREA
CM, SINUSOIDAL, AREA            ! CREATING AREA COMPONENTS FOR THE
                                  AREAS ON SINUSOIDAL SURFACE
LSLA, S                         ! SELECT LINES CONSTAINED IN THE CURRENT
                                  AREA SET
LESIZE, ALL, , , 1              ! DIVIDE THE LINE ELEMENTS ON THE
                                  SINUSOIDAL SURFACE INTO ONE SUBDIVISION
ALLSEL
VSWEEP, 1                       ! MESHING THE ONLY VOLUME THROUGH SWEEP
```

```
!-------------------------CONTACT PAIR CREATION---------------------------!
! CONTACT SURFACE
ASEL, S, AREA, , SINUSOIDAL  ! SELECT ALL THE AREA ELEMENTS ON THE
                               SINUSOIDAL SURFACE

NSLA, S, 1                   ! SELECT ALL THE NODES ATTACHED TO THE
                               AREAS IN THE CURRENT SET
TYPE, 3                      ! SELECT CONTA174
MAT, 1
ESLN, S, 0                   ! SELECT ALL THE ELEMENT ATTACHED TO THE
                               AREAS
ESURF                        ! LAYING ELEMENT CONTA174 ON THE MESHED TOP
                               SURFACE
ALLSEL
REAL, 1                      ! CREATE A PILOT NODE ON THE RIGID FLAT
TYPE, 2
TSHAP, PILO
N, 1E7 ,0, 0, 0
E, 1E7
NSEL, S , , , 1E7            ! SELECT THE NEWLY CREATED NODE
CM, PILOT, NODE
```

```
ALLSEL

!-------------------------SOLUTION SOLVER---------------------------!
/SOL                            ! SOLUTION PROCESSOR
                                ! FIRST LOAD STEP - STATIC ELASTO-PLASTIC CONTACT
                                ! BOUNDARY CONDITIONS
DA, (N-1)*(N-1) + 2, UZ, 0      ! BOTTOM SURFACE
DA, (N-1)*(N-1) + 2, UX, 0
DA, (N-1)*(N-1) + 2, UY, 0
DA, (N-1)*(N-1) + 3, UY, 0      ! SIDE SURFACES PERPENDICULAR TO Y AXIS
DA, (N-1)*(N-1) + 4, UY, 0
DA, (N-1)*(N-1) + 5, UX, 0      ! SIDE SURFACES PERPENDICULAR TO X AXIS
DA, (N-1)*(N-1) + 6, UX, 0

D, PILOT, UZ, PENE              ! MOVE PILOT NODE (RIGID FLAT) ALONG 0I + 0J +
                                  PENE K
D, PILOT, UX, 0
D, PILOT, UY, 0
D, PILOT, ROTX, 0               ! NO ROTATION
D, PILOT, ROTY, 0
D, PILOT, ROTZ, 0
```

```
! OPTIONS OF SOLVER
ANTYPE, 4                ! PERFORMS TRANSIENT ANALYSIS
TRNOPT, FULL             ! TRANSIENT ANALYSIS OPTIONS: FULL METHOD
                          (DEFAULT)
LUMPM, 0                 ! USE ELEMENT-DEPENDENT DEFAULT MASS
                           MATRIX FORMULATION (DEFAULT)
NLGEOM, 1                ! INCLUDE LARGE-DEFLECTION (LARGE ROTATION)
                           EFFECTS
OUTRES, ALL,-10          ! WRITE UP TO 10 EQUALLY SPACED SOLUTIONS
KBC, 0                   ! RAMPED LOADING
RATE, OFF                ! EXCLUD THE CREEP STRAIN RATE (NO CREEP)
NCNV, 2                  ! TERMINATE THE ANALYSIS, BUT NOT THE
                           PROGRAM EXECUTION
TIME, 1e-3               ! SIMULATION TIME OF FIRST LOAD STEP

LSWRITE, 1               ! WRITE FIRST LOAD STEP - STATIC ELASTIC-PLASTIC
                           CONTACT TO A FILE
! SECOND LOAD STEP
! BOUNDARY CONDITIONS
DKDELE, PILOT, ALL       ! DELETE CONSTRAINTS ON THE PILOT APPLIED IN
                           THE FIRST LOAD STEP
```

```
D, PILOT, UZ, PENE      ! POSITION OF RIGID FLAT IS HELD AT Z = PENE
D, PILOT, UX, 0
D, PILOT, UY, 0
D, PILOT, ROTX, 0
D, PILOT, ROTY, 0
D, PILOT, ROTZ, 0
! OUTRES, ERASE
OUTRES, ALL, -10
RATE, ON                ! INCLUDE THE CREEP STRAIN RATE
TIME, 0.01              ! SIMULATION TIME OF SECOND LOAD STEP

LSWRITE, 2              ! WRITE SECOND LOAD STEP - STATIC ELASTIC-PLASTIC
                          CONTACT TO A FILE
! THIRD LOAD STEP
! BOUNDARY CONDITIONS
DKDELE, PILOT, ALL    ! DELETE CONSTRAINTS ON THE PILOT APPLIED IN THE
                        FIRST LOAD STEP
D, PILOT, UZ, PENE      ! POSITION OF RIGID FLAT IS HELD AT Z = PENE
D, PILOT, UX, 0
D, PILOT, UY, 0
D, PILOT, ROTX, 0
```

```
D, PILOT, ROTY, 0

D, PILOT, ROTZ, 0

!OUTRES, ERASE

OUTRES, ALL, -10

TIME, 0.1                    ! SIMULATION TIME

LSWRITE, 3                   ! WRITE THIRD LOAD STEP - STATIC ELASTIC-PLASTIC
                               CONTACT TO A FILE

! FOURTH LOAD STEP

! BOUNDARY CONDITIONS

DKDELE, PILOT, ALL   ! DELETE CONSTRAINTS ON THE PILOT APPLIED IN TEH
                               FIRST LOAD STEP

D, PILOT, UZ, PENE       ! POSITION OF RIGID FLAT IS HELD AT Z = PENE

D, PILOT, UX, 0

D, PILOT, UY, 0

D, PILOT, ROTX, 0

D, PILOT, ROTY, 0

D, PILOT, ROTZ, 0

OUTRES, ERASE

OUTRES, ALL, -10

TIME,   1                    ! SIMULATION TIME

LSWRITE, 4                   ! WRITE FOURTH LOAD STEP - STATIC ELASTIC-PLASTIC
```

CONTACT TO A FILE

```
! FIFTH LOAD STEP
! BOUNDARY CONDITIONS
DKDELE, PILOT, ALL       ! DELETE CONSTRAINTS ON THE PILOT APPLIED IN THE
                           FIRST LOAD STEP
D, PILOT, UZ, PENE       ! POSITION OF RIGID FLAT IS HELD AT Z = PENE
D, PILOT, UX, 0
D, PILOT, UY, 0
D, PILOT, ROTX, 0
D, PILOT, ROTY, 0
D, PILOT, ROTZ, 0
OUTRES, ERASE
OUTRES, ALL, -10
TIME,   10                 ! SIMULATION TIME
LSWRITE, 5                 ! WRITE FIFTH LOAD STEP - STATIC ELASTIC-PLASTIC
                             CONTACT TO A FILE
! SIXTH LOAD STEP
! BOUNDARY CONDITIONS
DKDELE, PILOT, ALL         ! DELETE CONSTRAINTS ON THE PILOT APPLIED IN
                             THE FIRST LOAD STEP
D, PILOT, UZ, PENE         ! POSITION OF RIGID FLAT IS HELD AT Z = PENE
```

```
D, PILOT, UX, 0
D, PILOT, UY, 0
D, PILOT, ROTX, 0
D, PILOT, ROTY, 0
D, PILOT, ROTZ, 0
OUTRES, ERASE
OUTRES, ALL, -10
TIME,   100                    ! SIMULATION TIME
LSWRITE, 6                     ! WRITE SIXTH LOAD STEP - STATIC ELASTIC-PLASTIC
                                 CONTACT TO A FILE
! SEVENTH LOAD STEP
! BOUNDARY CONDITIONS
DKDELE, PILOT, ALL      ! DELETE CONSTRAINTS ON THE PILOT APPLIED IN THE
                          FIRST LOAD STEP
D, PILOT, UZ, PENE      ! POSITION OF RIGID FLAT IS HELD AT Z = PENE
D, PILOT, UX, 0
D, PILOT, UY, 0
D, PILOT, ROTX, 0
D, PILOT, ROTY, 0
D, PILOT, ROTZ, 0
OUTRES, ERASE
```

```
OUTRES, ALL, -10
TIME,   500                 ! SIMULATION TIME
LSWRITE, 7                  ! WRITE SEVENTH LOAD STEP - STATIC ELASTIC-PLASTIC
                              CONTACT TO A FILE
LSSOLVE, 1, 7, 1            ! SOLVE
```